TOHOKU
UNIVERSITY

博 士 学 位 論 文

論文題目

Quantifying Correlations Between Geometrical Features and Wall Shear Stress in Basilar Artery
脳底動脈における幾何学的特徴と壁せん断応力との相関の定量化

提 出 者　　東北大学大学院医工学研究科

医工学専攻

学籍番号 COWD1010

氏　　　名　潘 方家 PAN FANGJIA

指 導 教 員	太田　信　　　　　　　　　　　　　　　　教授	
審 査 委 員 （○印は主査）	○　太田信 1 西條芳文　　　　　　　　2 石川拓司 3 麦倉俊司　　　　　　　　4 Philippe　BIJLENGA 5 安西眸　　　　　　　　　6	

<center>提 出 者 略 歴</center>

ふり がな 氏 名	はん　　ほうか 潘　方家		昭 和 西 暦	
本 籍		都・道 府・県	国 籍	

<center>履 歴 事 項</center>

【 学 歴 】	

【 職 歴 】	
年　　　月　　　日	
年　　　月　　　日	
年　　　月　　　日	
年　　　月　　　日	

備考１）外国人留学生は、国籍を記入してください。２）履歴事項は、大学入学から年次にしたがって記入してください。

修了年度	2023 年度	課程	博士課程後期 3 年の課程

英文 Abstract

Title:　　Quantifying Correlations Between Geometrical Features and Wall Shear Stress in Basilar Artery
Author:　　Fangjia PAN
Supervisor: Makoto OHTA

This thesis quantified vessel geometry-hemodynamic stress correlations, aiming to help the early detection and prediction of intracranial aneurysm (IA). As the quantified influence on IA formation brought by hemodynamic stress remained unclear, a literature review was conducted to identify biomarkers for IA detection and prediction. From the summary, the potential use of geometry for detection and the importance of wall shear stress (WSS) for IA prediction were identified. Although some of the geometric features were reported to be influential, the influence degrees of geometric features on the hemodynamic stress remained unclear. Based on the findings from the review, studies were conducted on quantifying geometry-WSS correlations. Initially, bifurcation angles associated with IA were explored. The results revealed that at bifurcation with more than two branches such as the basilar artery apex, significant angle differences can be observed among groups with IA occurring at different sites. This observation suggested the potential use of bifurcation angles for early IA detection. Subsequently, the influence degree brought about by various geometric features and flow velocity on WSS was calculated. The results identified blood velocity at the bifurcation plane as the most influential parameter. Vessel diameters also showed significant impact on 10th and 2.5^{th} quantiles of WSS. To further quantify the geometry-WSS correlations, investigations into the impact of boundary conditions on WSS were evaluated. The study found that the generalized boundary conditions tended to overestimate WSS, whereas the normalized WSS could still reflect around 90% of specific WSS. This thesis work revealed the influence degrees on WSS from geometric features and velocity. These results can be expected to contribute to future studies on IA prediction and early detection.

和文アブストラクト

論文題目：　　脳底動脈における幾何学的特徴と壁せん断応力との相関の定量化
提出者氏名：　潘　方家
指導教員：　　太田　信

本論文では、頭蓋内動脈瘤（IA）の早期発見と予測に役立てることを目的として、血管形状と血行力学的ストレスの相関を定量化した。IA 形成に対する血行力学的ストレスの影響の定量的な解明がまだ得られていないため、IA 早期発見と予測に有用なバイオマーカーを同定するために、まず文献レビューを行った。この結果、IA を早期発見するための幾何学的形状特徴の利用可能性と、IA 予測における壁せん断応力（WSS）の重要性が明らかになった。また、いくつかの幾何学的特徴が WSS に影響することがこれまでにも報告されてきたが、幾何学的特徴がもたらす影響度は不明であった。

文献レビューの結果に基づき、血管形状–WSS 定量的相関を明らかにすることとした。まず、IA に関連する分岐角について計測した。その結果、脳底動脈頂部のような複数の枝を持つ分岐が存在する箇所では、異なる部位で IA が発生したグループ間で有意な角度差が観察された。この観察結果は、IA の早期発見に分岐部角度を利用できる可能性を示唆した。続いて、さまざまな幾何学的特徴が WSS に及ぼす影響度を算出した。その結果、分岐面における血流速度が最も影響力のあるパラメータであることが同定された。血管径も WSS の 10 分位値と 2.5 分位値に有意な影響を示した。形状と WSS の相関をさらに定量化するために、境界条件が WSS に与える影響を評価した。この結果、一般化された境界条件は WSS を過大評価する傾向がある。一方、正規化された WSS は、患者固有境界条件を用いた場合の WSS を約 90%反映した。以上より、幾何学的特徴や血流速度による WSS への定量的影響度が明らかになった。これらの成果は、IA 予測および早期発見に貢献すると期待できる。

TOHOKU UNIVERSITY

Graduate School of Biomedical Engineering

Quantifying Correlations Between Geometrical Features and Wall
Shear Stress in Basilar Artery

脳底動脈における幾何学的特徴と壁せん断応力との相関の定量化

A Dissertation Submitted for the Degree of Doctor of Philosophy (Biomedical Engineering)
Graduate School of Biomedical Engineering

by
Fangjia Pan
March 2024

Contents

Abbreviations

Vessels	
AICA	anterior inferior cerebellar arteries
BA	basilar artery
ICA	internal carotid artery
MCA	middle cerebral artery
PCA	posterior cerebral artery
PcomA	posterior communicating artery
SCA	superior cerebellar artery
VA	vertebral artery
Medical checks	
CTA	computed tomography angiography
MRA	magnetic resonance angiography
US	ultrasound
Disease	
AS	atherosclerosis
CVD	cerebrovascular disease
IA	intracranial aneurysm
Others	
CFD	computational fluid dynamics
iNOS	inducible nitric oxide synthase
IQR	interquartile range
OSI	oscillatory shear index
VIF	variance inflation factor
WSS	wall shear stress
WSSG	wall shear stress gradient

List of figures

List of tables

Chapter 1

Introduction

Chapter 1   Introduction

1.1 Background

1.1.1   Cerebral aneurysm

Cerebral aneurysm, also known as intracranial aneurysms (IA), are defined as dilations that occur at weak points alongside the arterial circulation happening inside the brain [1] (Fig.1-1). The prevalence of IAs is reported in around 0.4% to 3% of the general population[2]. Another report claimed that the prevalence of unruptured IA is in between 2% to 5% [3]. The presence of IA is in a notable proportion of the general population because of the lack of symptoms for most of the IAs.

Although most IAs are silent, the consequences of aneurysm rupture are fatal. Once an IA ruptures, the morbidity and mortality are very high. It is reported that nearly 25% are dead within the first 24 hours and 50% will die within the next three months [1]. The overall fatality rates are reported between 33% and 77% at 1 year after bleeding [4]. Aneurysm rupture is reported as the most common reason of nontraumatic subarachnoid hemorrhage, which is known as a devastating event with high rates of mortality, morbidity, and disability, along with high medical costs and decrease of life quality [5]. The substantial mortality risk associated
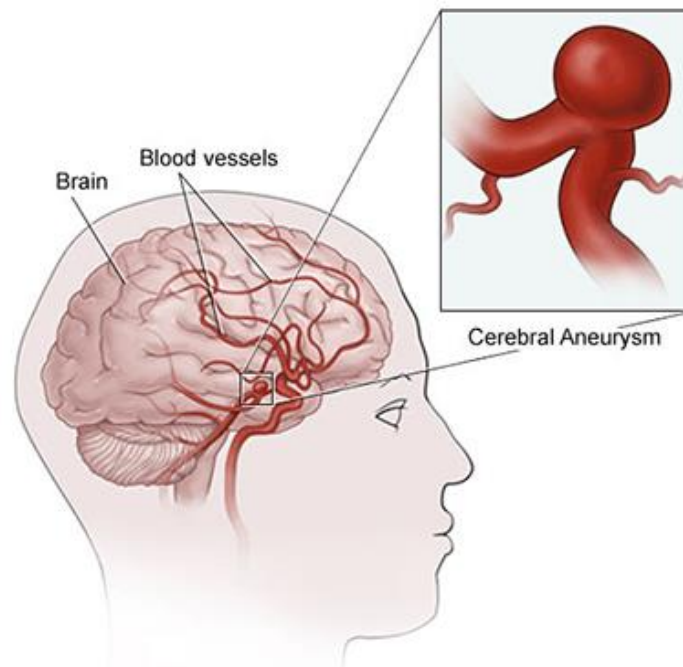
Figure 1-1 Cerebral aneurysm: a typical structure of the cerebral aneurysm.

(Cited from: https://www.rwjbh.org/images/hospital-locations/rwj%20new%20brunswick/cerebral-aneurysm-400px.png 2023/11/15)

with IAs emphasized the importance of the early detection and intervention prior to the onset of the disease.

1.1.2   Aneurysm and its location preference

Cerebral aneurysm is usually considered as a focal disease. Not all positions at the vessel tree have the same possibility of IA happening. A vast majority of IAs are saccular aneurysms [5], and the typical sites for saccular IAs are at bifurcation apices [6]. Even among all those bifurcation positions, the happening ratios are uneven and IA formation is showing its own preference.

It is reported that approximately 85% of aneurysms are located in the anterior circulation, predominately at junctions or bifurcations along the circle of Willis [1]. Nehls et al. reported their findings that common locations for multiple aneurysms were the posterior communicating artery, middle cerebral artery, anterior communicating artery and ophthalmic artery [7].

The reason for this site preference, also referred to as the relationship between IA formation and the geometry of its parent vessel, has been discussed a lot. Kayebe et al. pointed out that the asymmetric circle of Willis is correlated with more common happening of IAs [8]. Similar conclusions were also reported in the middle cerebral artery (MCA). Alongside the asymmetry, the author also reported that the presence of a long and less tortuous parent vessel upstream is potentially the mark of higher risks. Other researchers also studied the correlation between torsion and aneurysms. Marina Piccinelli et al. revealed that compared to unruptured ICA aneurysms, the ruptured ones tend to have a smaller radius, lower maximum curvature, and lower proximal torsion [9].

Although they reported that vessels with less bending are correlated with aneurysms, some researchers reported the opposite correlation between torsion and aneurysm formation. Alexandra et al. employed both specific and normalized models and revealed that high bend curvature induces high WSS and wall shear stress gradient (WSSG), leading to the local conditions known as contributions to aneurysms [10]. Zhang et al. proposed that the abnormal WSS in vessels with curved or bifurcated vessels leads to continuous stimulation to the vessels, triggering the inflammatory cells and local inflammatory reaction [11]. Various parameters have been employed to describe the bending geometry, including relative length (RL), sum of angle metrics (SOAM), triangular index (TI), product of angle distance (PAD), and inflection count metrics (ICM). Among all these parameters, both Roger [12] and Kornelia [13] emphasized SOAM and TI as factors highly correlated with aneurysm development. Labeyrie

et al. revealed that tortuosity happening at the cervical artery is significantly associated with IAs [14] but the association between tortuosity and aneurysm characteristics was not observed. The association between increased tortuosity and IA was also observed in studies conducted by Bum Joon Kim [15]. They promoted tortuosity as an independent influence factor to the presence of hypertension and smoking habits.

In addition to the vessel bending, diameters and angles have also been reported as parameters correlated with aneurysm formation, development, and rupture. Marina reported smaller ICA diameters with ruptured aneurysms than unruptured ones [9]. Similarly, Kono et al. proposed proximal stenosis as a potential factor to induce aneurysm formation [16].

When it comes to the vascular angles, studies have shown that larger angles seem to be correlated with aneurysm formation. These kinds of studies have been reported on BA, MCA, and ICA [17]–[19]. However, this correlation between vascular angles and aneurysm presence remains unclear because most of the studies are only able to gather patients' information after the aneurysm happening. Recently, a multi-center study with a large database has revealed that angle changes are more likely to happen after aneurysm formation. The detailed correlation and the timeline of angle changes require more study in the future.

As we summarized above, various studies have been done on the aneurysm location preference and tried to find out the geometry factors having higher possibility of aneurysm happening.

1.1.3 Aneurysm and hemodynamics

Previous research not only pointed out the location preference of IA formation, but they also proposed that this phenomenon is mainly contributed by hemodynamic stresses. Hemodynamics, which is known as the study of blood flow and its forces on vessel walls, plays an important role in the pathogenesis, development, and rupture of IAs. In the last two decades, a large amount of research has focused on the correlations between hemodynamic stressors and aneurysm pathogenesis, including the formation, development, and rupture of aneurysms. Researchers believe that study on the aneurysm-hemodynamic correlations will help future prediction, prevention, and rupture prediction of aneurysm treatments.

It has been proposed that the hemodynamic stressors are correlated because the mechanical stimuli working on vessel walls will transduce into biological signals and trigger inflammatory cascades. This serious of transcriptional and signaling process will ultimately lead to vascular wall remodeling [20]. Although this hypothesis has been widely recognized, the detailed correlation about how hemodynamic stress is influencing aneurysms remained

unclear. Most of the researchers could only make compare analysis between already happened aneurysms and its hemodynamic environments. It can be difficult to have longitudinal studies on aneurysm from its initiation to its development because most of the aneurysms have no symptoms before its rupture. Many of the unruptured aneurysms are detected when patients are undergoing medical checks for other diseases. This induced the difficulty of tracing the hemodynamic stress before and after the initiation of aneurysms, as well as during its development process.

Various parameters describing hemodynamic stress have been reported. Plenty of parameters have been lifted, including wall shear stress (WSS), wall shear stress gradient (WSSG), oscillatory index (OSI), pressure loss (PL), etc. The most famous one will be the WSS. What has been reported by animal and cell experiments is that endothelial cells sense the WSS in the environment and change this stress into biological signals [21]. The WSS is not only working as the trigger of this signal and causing the pathologic responses, also known as contributors for the vessel remodeling. Because of the lack of external elastic lamina, medial elastin, and supporting adventitial and perivascular tissues, the influence brought by the WSS on cerebral vasculature is intrinsically obvious [5]. Recent studies in animal models have shown that WSS is playing a vital role in IA initiation. High WSS and a positive WSSG can cause cascades of biochemical signals which are known as the trigger of aneurysm initiation [22]. The high WSS and positive WSSG exceeding threshold will cause local loss of internal elastic lamina, and media thinning, which are known as the earliest signs of IA formation [22].

Although studies about WSS and aneurysms have been reported a lot, how WSS is affecting aneurysms remains unclear. Some reports emphasized low WSS can be dangerous, and some insisted that high WSS works on IA formation. By increasing local blood flow manually, Gao et al. induced aneurysms in rabbits by unilateral ligation and with the expose under high WSS, all rabbits had aneurysms. Their experiments proved that flow increase alone at the bifurcations can lead to a nascent aneurysm [23]. Nam et al. also reported that the increase of WSS in the circle of Willis with morphological variations can be potential contributions of aneurysm formation [24]. On the other hand, Machi et al. reported the opposite. They proposed that low WSS and the coming high oscillatory index (OSI) is triggering formation of aneurysms [25]. Doenitz et al. also stands the hypothesis of low WSS [26]. They revealed that there exists low WSS in specific locations and lowering the already low WSS leads to endothelial damage and to a decrease in stability of the vessel wall, which in the end, will cause aneurysm development, growth, and rupture.

Facing these contrast conclusions, Meng et al. proposed their own hypothesis integrating these contrast results [5]. They reported that both low and high WSS can be influential to IA formation and development (Fig.1-2). According to their hypothesis, the combination of a high WSS and a positive WSSG can cause the initiation of aneurysms. Further in the development of the aneurysms, both a high WSS and a low WSS can affect its growth by activating different pathways. They also emphasized the integration of a high WSS and a positive WSSG. Metaxa et al. also reported the combination of WSS and WSSG and the influence on aneurysm formation brought by this combination [22].

In all, we understood that it has been widely accepted that hemodynamic stress, especially WSS, is working as a key factor of aneurysm formation. However, the details remain unclear and require further study.
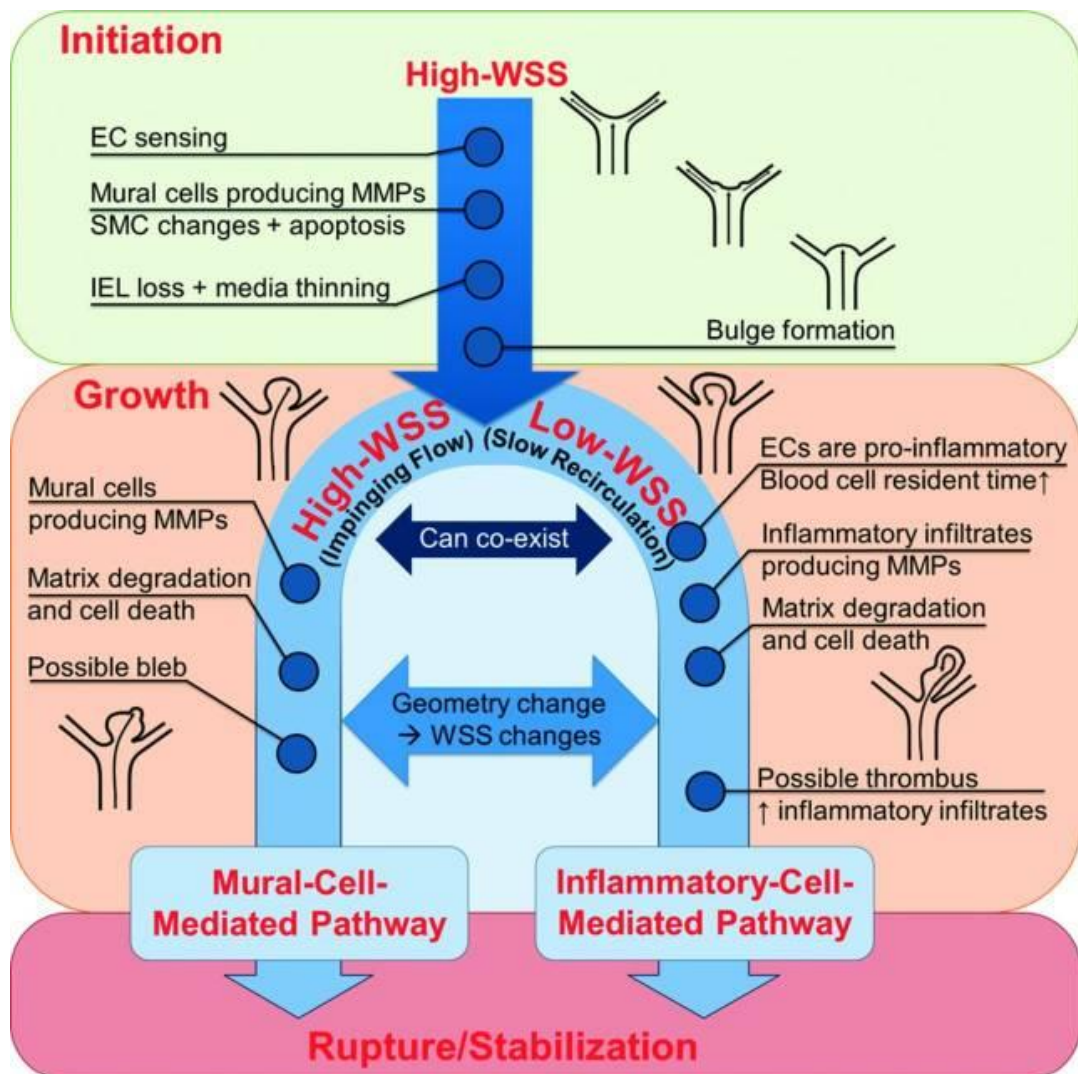

Figure 1-2 Role of WSS in aneurysm initiation, growth, and rupture [5]

1.1.4 Vessel geometry and hemodynamics

From the summary above, we understood that IA formation has its own local preference, which is highly affected by vascular geometry. What's more, considering that the hemodynamic stress refers to the physical stress brought by blood flow working on vessel walls, it is understandable that the hemodynamic stress is connected to the vessel geometry. The most studied hemodynamic stress parameter, WSS, refers to the tangential force between blood flow and wall and is highly sensitive to the vasculature geometry. Several studies tried to figure out the correlations between vessel geometry and WSS and the possibility of using geometry features as risk factors for aneurysm prediction and detection. Hassan et al. proposed categorization of IAs based on the parent vessel geometry [27]. They believe that this categorization will provide a promising way of understanding the natural history of IAs and assist aneurysm management.

Studies concerning the vascular geometry-WSS correlations were conducted. The proposed geometric features include the bending of vessels, the diameters, and the angles. Kornelia et al. mentioned that the correlation between the bending and WSS can be complicated and depends on the definition of the bending [28]. In addition, studies about vascular angles and WSS were also conducted. Tütüncü et al pointed out that widening of basilar bifurcation angles is associated with IA by performing computational simulations [18]. Their simulation results revealed that when the bifurcation angles are widened, the impingement area at the bifurcation apex will also become wider. The widened area will extend the protected zone at the bifurcation apex and cause the weakening of the area outside the apex, which is considered as the initial step of aneurysm formation.

Although not for the study of aneurysms but for the atherosclerosis, another common vascular disease, Zhang et al. performed studies on geometry-WSS were conducted and promoting cross-sectional expansion at the bifurcation as influential factors on WSS [29].

In all, studies have been conducted on geometry-WSS correlations and several geometric features have been emphasized. However, the detailed correlations remained unclear and require further studies.

1.1.5 Computational simulation and hemodynamics

WSS and other hemodynamic stress parameters were mentioned a lot in the introduction above. The way to get access to this information changed throughout history. Before the bloom of computer techniques, experiments with normalized models were commonly utilized. In the last two decades, because of rapid progress on computer calculating

speed and the huge change of precise medical imaging techniques, the computational fluid dynamics (CFD) simulations have been widely utilized to get information of hemodynamic stress. Plenty of studies searching on the connections between hemodynamics and aneurysm development/ rupture are using CFD simulations for very detailed hemodynamic information [5], [27], [28]. CFD techniques are believed to have the potential to be a clinical tool for predicting the occurrence, development, and rupture of IA.

Many engineers are working on applying CFD before the surgery to help improve the treatment decision and prognosis. Although doctors are also welcoming these efforts, there are still several problems slowing down the wide use of CFD in clinical situations. One of these problems is the time and cost consumed by computational simulations are making it not suitable for daily used situations in clinical field. It takes time to perform specific simulations for patients, especially when we are trying to make CFD results close enough to the real situation, the time costs will be huge. At medical situation, the time costs make the application before surgery difficult. This made us think of making a detailed correlation study between hemodynamic stress and geometric features. With this connection, we could make a rough estimation of hemodynamic situations from geometric features, which are easier to get access to, so that we could get closer to applying hemodynamic prediction before IA formation.

1.2 Study object

1.2.1 Basilar artery and vertebral artery

This study is focusing on the basilar artery (BA). BA is the vessel formed by two vertebral arteries (VAs) at the base of the pons [30]. BA together with two VAs can be called vertebrobasilar system. There are several reasons for choosing this artery as the object of our study:
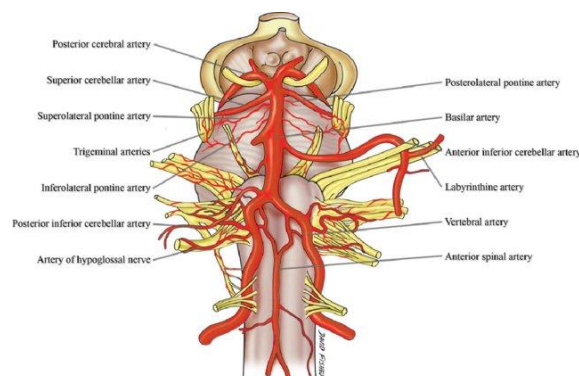
Figure 1-3 Frontal view of basilar artery [152]: the frontal view of

BA together with the brain stem.

- Unique structure: The vertebra-basilar system is the only location where two arteries merge together into one [31]. This unique structure brings the variation of BA geometry (Fig.1-4). Studies have reported on the anatomical variability in BA origin, length, termination, as well as the diameter and angles [32]–[34] (Fig.1-2, 1-3).

- Important position: The vertebra-basilar system supplies blood to the posterior part of the cerebral hemispheres [35] (Fig.1-5). An average of 20% of intracranial blood stream derives from this circuit [30]. BA locates proximal to the Circle of Willis and serves the primary supply to the posterior brain [31].

1.2.2 Basilar artery aneurysm

BA aneurysm represent only 3%-5% of all IAs according to previous report [36]. However, because of its special geometry and location, as we mentioned in chapter 1.2.1, the prognosis of BA aneurysm can vary a lot. Actually the mortality rates for ruptured BA aneurysms can be as high as 23% [37]. What's more, rapidly growing basilar tip aneurysms are
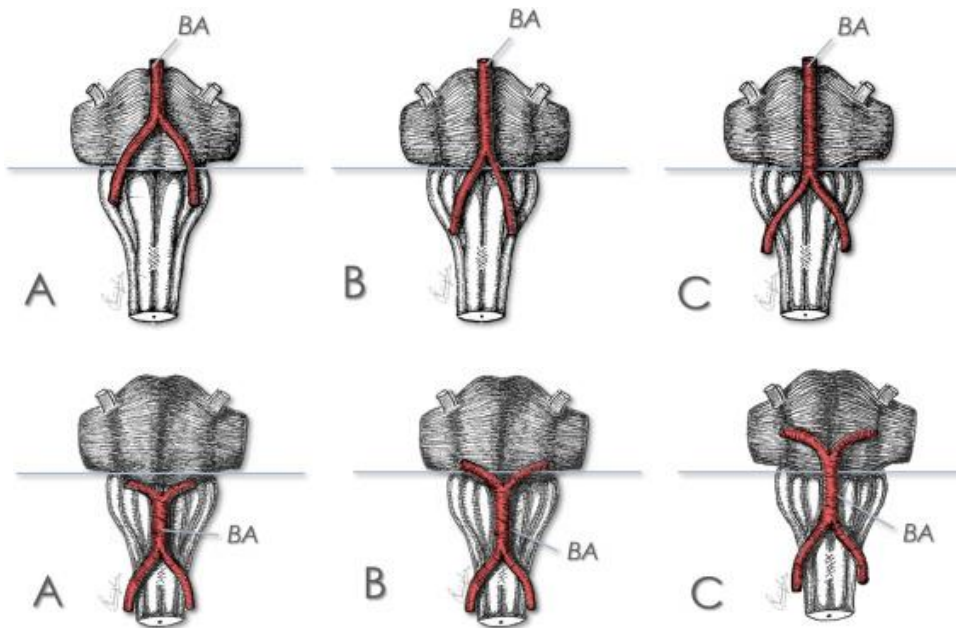
Figure 1-4 Level of BA formation & termination [32]: the upper line exhibited the different position of BA formation: A. Above the ponto-medullary junction; B. At the ponto-medullary junction; C. Below the ponto-medullary junction. The lower line exhibited different position of BA termination: A. Below the ponto-medullary junction; B. At the ponto-medullary junction; C. Above the ponto-medullary junction.
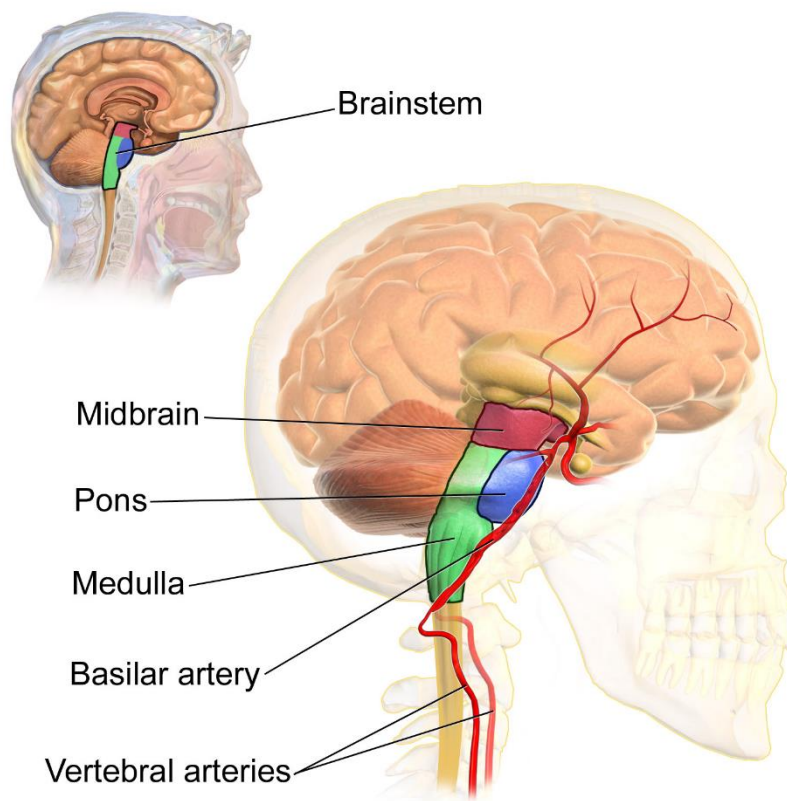
Figure 1-5 BA location: the location of BA within the brain. (cited from https://en.wikipedia.org/wiki/Basilar_artery 2023/11/15)

reported to be the trigger of a mass effect on the brain stem because of the increasing pressure on the areas [38].

In all, the large geometry variability of BA and the severe situations the BA aneurysm may cause motivated us to consider BA as our main study object.

1.3 Scope and thesis contents

Based on the possible severe situation caused by aneurysm rupture and the difficulty of aneurysm early detection described in chapter 1.1, we feel the importance of doing studies on primary prevention of the disease, including the risk prediction and early detection.

One of the factors we considered to be used for pre-disease risk assessment is hemodynamic stress. As described in chapter 1.1.2 to chapter 1.1.4, aneurysms are considered as focal vascular diseases having preference on occurrence sites and hemodynamic stresses are recognized as one vital factor contributing to the disease.

It is not easy to directly obtain the hemodynamic stress for risk assessment. As described in chapter 1.1.5, hemodynamic stresses can be accessed by performing computational simulations. However, doing simulations requires training of technicians, large

amount of costs on simulation software, and long calculation time. This all made simulations far from being widely applied in annual health checks.

To solve the problem that hemodynamic stress is hard to directly obtain, we had the idea that make detailed connections between geometry and hemodynamic stress, so that we could use the geometric features to make roughly hemodynamic predictions. We performed this study to quantify the correlation between geometric features and wall shear stress and promote the influence degree on WSS from various geometric features. With this quantified correlation, we would be able to propose the geometric features correlated to WSS to the most and deserve more future attention, and further help the development of IA formation predictions.

The contents of this study are introduced as follows:

Chapter 1: This chapter is the introduction chapter and works as the leading part of this whole thesis. A brief introduction of the background, study object and the outline of our study is included in this chapter.

Chapter 2: We are going to introduce the literature review we did on the mechanism of aneurysm formation and growth, especially those connected to hemodynamic stress and computational simulations. The literature study made us understand the importance of making study on WSS and this understanding motivated our following studies focusing on vessel geometry and WSS.

Chapter 3: To clarify the correlations between geometric features and aneurysm sites, we performed a study directly searching for the correlations between vascular angles and aneurysm locations. In this chapter, we will describe different BA aneurysms categorized by IA location and their connection to wider angles around the BA apex.

Chapter 4: Following our results from chapter 3, we turned into the study on correlations between geometric features and WSS. In this chapter, we will introduce our statistical analysis results on this correlation and the most influential geometric feature working on WSS.

Chapter 5: Computational simulations were performed in previous chapters for WSS information. We found the differences brought by boundary conditions on WSS results and performed this study to clarify how much the boundary condition is going to affect simulation results.

Chapter 6: This is the conclusion chapter. The whole study results will be summarized in this chapter.

Chapter 2

Review on the aneurysm formation and development contributed by hemodynamic stress

Chapter 2   Review on the aneurysm formation and development contributed by hemodynamic stress

2.1 Introduction

A cerebral aneurysm is a localized bulging or ballooning in a blood vessel in the brain. When the aneurysm ruptures, it causes internal bleeding, such as a subarachnoid hemorrhage and intracranial hematoma, which can be fatal. However, most cerebral aneurysms remain unruptured. Instead, they occasionally give rise to health problems or symptoms, such as the compression of surrounding nerves and brain tissue by aneurysms, leading to nerve paralysis, headaches, and vomiting.

The formation of aneurysms begins with the extrusion happened on the weakened position of an artery's wall. The reason why this local weakening happened in arteries remains uncertain. Some aneurysms maintain a constant size, while others grow continuously. Research by Koffijberg et al. suggests that cerebral aneurysms do not grow steadily [39]. The growth rate of aneurysms varies from each other; it can take a few years for an aneurysm to enlarge by 1 mm and show up clearly on an angiography [40].

To understand the latest studies concerning on correlations between aneurysms and hemodynamic stress and help IA prediction and detection, we performed this literature review. In this review, we looked at the formation and development of cerebral aneurysms as follows. In the first section, we made a summary of the ideas that have been proposed to explain the pathophysiology of cerebral aneurysms, focusing on epidemiological and pathological perspectives. We also gathered data derived from animal models of experimentally induced cerebral aneurysms. The attention points of the studies we gathered were the involvements of hemodynamic stress on the artery wall.

The second section summarized research focusing on the initiation of cerebral aneurysms, especially those performed with the method of CFD. After briefly reviewing the history of blood flow analysis studies, we reviewed hemodynamics-based hypotheses related to the initiation of cerebral aneurysms. Among the presented hypotheses, the significance of high WSS and a high WSSG were emphasized. We also reviewed other leading hypotheses involving hemodynamics-related parameters.

In the third section, we discussed CFD studies on the growth of cerebral aneurysms. In these studies, hemodynamic parameters are compared between growing and stable aneurysms to highlight the hemodynamic characteristics associated with the aneurysm growth.

2.2 Epidemiology, pathology, and animal experiments

In the past, the causes of cerebral aneurysms were classified as "congenital," "acquired," or "a combination of both congenital and acquired" [41]–[43]. Current understanding suggests that acquired factors are the primary cause of cerebral aneurysms, with some contributions brought by congenital factors, including genetic diseases, which increase the vulnerability of vascular walls. Below, we made a chronological summary of historical theories regarding the development of cerebral aneurysms, taking the epidemiological and pathological perspectives into consideration, and based on data from animal models that were utilized to experimentally produce cerebral aneurysms.

2.2.1 Hypothesis based on pathological factors

In 1930, Forbus et al. stated that medial defects, which are infrequently seen at cerebral artery bifurcations, are indicative of a congenital condition known as cerebral aneurysms [41]. On the contrary hand, Glynn et al. argued in 1940 that cerebral aneurysms are an acquired disease resulting from local degenerative changes in the internal elastic lamina [42]. By 1950, Carmichael et al. merged the two theories mentioned above and introduced a "congenital and acquired" hypothesis. This theory suggested the possibility that coincidental degenerative changes in the inner elastic lamina occur at locations where medial abnormalities happen [43]. In 1961, for the first time, Hassler et al. emphasized hemodynamic stress and pointed out that cerebral aneurysms are induced when the inner elastic lamina is stretched excessively due to hemodynamic stress in regions with medial defects [44]. Subsequently, in 1963, Stehben and colleagues paid their attention on acquired factors such as hypertension, hemodynamic stress, and cerebral arteriosclerosis. They dismissed the presence of congenital medial defects, and finally proposing that cerebral aneurysms are primarily acquired [45].

2.2.2 Animal model of experimentally induced cerebral aneurysms

Empirical evidence has shown the involvement of hemodynamics in the development of cerebral aneurysms [8], [46]–[49], and hypertension , which leads to a systemic increase in hemodynamic forces, stands as one of the primary risk factors for aneurysm formation [48]. Cerebral aneurysms are typically situated at the bifurcation of the circle of Willis, where the interconnected pathways facilitate collateral circulation in the event of partial occlusion of the blood flow. Such aneurysms are more prevalent in individuals with an asymmetric circle of Willis [8]. When one internal carotid artery (ICA) is blocked unilaterally, it can trigger the formation of cerebral aneurysms in the anterior communicating artery (Acom). This occurs as

a compensatory increase in blood flow [46] takes place, and the irregular geometries of the anterior cerebral arteries (ACAs) are closely linked to the development of Acom aneurysms [49]. Consequently, local elevations in hemodynamic stress, stemming from disrupted hemodynamics in an asymmetric circle of Willis, in conjunction with systemic hemodynamic enhancements (such as hypertension), may be crucial prerequisites for the emergence of cerebral aneurysms.

Hashimoto et al. directed their attention toward this hemodynamic phenomenon. In 1978, they achieved a significant milestone by successfully inducing cerebral aneurysms in rats through experiments. They accomplished this by inducing a local increase in hemodynamics in the circle of Willis through unilateral common carotid artery ligation, enhancing systemic hemodynamics by inducing renovascular hypertension, and administering 3-aminopropionitrile (BAPN), an inhibitor of lysyl oxidase (an enzyme that catalyzes cross-linking of collagen and elastin) to induce weakening of the arterial wall [50]. The resulting cerebral aneurysms were induced in the Acom and at the bifurcation of the ACA and the olfactory artery where blood flow is increased following unilateral carotid artery occlusion, which mirrors the micro- structural changes observed in human cerebral aneurysms [50]–[53]. Additionally, they demonstrated that cerebral aneurysms can be induced in the animal model even without BAPN, indicating that acquired hemodynamic factors alone are sufficient for cerebral aneurysm development [53]. Subsequently, cerebral aneurysms were experimentally induced in monkeys, which exhibit greater anatomical similarity to humans [54]. The consistent association of cerebral aneurysms with increased hemodynamic values across rodents, monkeys, and humans suggests a possibility of shared mechanisms in the aneurysm development among mammalian species. Consequently, researchers should be able to gain insights into the pathogenesis of cerebral aneurysms in humans by investigating the mechanisms formation mechanisms in animal models.

In Hashimoto et al.'s animal model, the initial formation of cerebral aneurysms, characterized by endothelial degeneration and disruption of the internal elastic lamina, predominantly occurs at the distal side of the major branch adjacent to the apex. Additionally, aneurysmal bulging was observed in this specific area [52]. Notably, hemorheological studies, which involved numerical analysis of latex particle paths in a rat model, revealed that WSS increased during the early phases of cerebral aneurysm development, and reached the peak values in this region [55]. In 1991, for the first time, Nakatani et al. suggested that an increased WSS contributes to the development of cerebral aneurysms.

However, the progression of cerebral aneurysm development is unlikely to result directly from mechanical stress induced by increased WSS [56]. Blood vessels sense the blood flow volume by sensing WSS rather than blood pressure. Vascular endothelial cells detect WSS generated by blood flow and subsequently regulate blood flow through remodeling shapes and releasing biochemical mediators [57]. Fukuda et al. introduced the WSS mechanotransduction theory, proposing that endothelial cells sense locally increased WSS-related hemodynamics environment within the vessel wall. This sensing initiates the production or activation of biochemical mediators that harm vessel walls components, leading to aneurysm formation. In 2000, they reported the expression of inducible nitric oxide synthase (iNOS) in human and rat cerebral aneurysms. They further demonstrated that both a reduction in WSS and the inhibition of iNOS decreased aneurysm development in rats after aneurysm induction surgery [58]. Thus, the focal point of the initiation of cerebral aneurysm formation shifted from the vascular media and internal elastic lamina to the endothelium, the inner layer of the blood vessel. The next step involved clarifying the spatial and temporal patterns of hemodynamic stress in cerebral aneurysms. Due to their small size, animal models proved unsuitable for such investigations. Instead, CFD techniques were initiated around 2004 to identify the hemodynamics-related factors contributing to human cerebral aneurysm development, growth, and rupture.

2.2.3 Cerebral aneurysm as a chronic inflammatory disease and hemodynamic stress

Based on the work done by Fukuda et al., Aoki et al. proposed that the agents causing damage to the arterial wall and triggering the formation of cerebral aneurysms are inflammatory factors originating from macrophages [59]–[61]. They pointed out that, during the initial stages of cerebral aneurysm development under increased WSS-related hemodynamics, a positive signaling pathway is established, comprising cyclooxygenase-2 (COX-2), prostaglandin E2, and prostaglandin E receptor 2. This is followed by the induction of monocyte chemotactic protein-1 (MCP-1) expression and subsequent recruitment of macrophages [61]. Their goal was to identify pharmacological inhibitors for the prevention of cerebral aneurysm development.

In 2008, Gao et al. established a rabbit model for inducing cerebral aneurysms through bilateral carotid artery ligation [23]. They combined this animal model and CFD analysis with clinical data. In their investigation using the rabbit aneurysm model, they proposed that damage to the internal elastic lamina occurred specifically at locations with a WSS exceeded 122 Pa (a surprisingly high value), along with a WSSG surpassing 530 Pa/mm [22]. This implied that the

initial changes in the development of cerebral aneurysms were associated with the exceeding of normal physiological WSS. For their hypothesis regarding the formation of cerebral aneurysms, please refer to the subsequent section [5].

A cerebral aneurysm undergoes a reduction in size or disappears when the blood flow in the parent artery decreases [62], [63]. Cerebral aneurysms located on distal feeding arteries near the arteriovenous malformation nidus have a high possibility of regressing with substantial or curative treatment of the arteriovenous malformation A patient-specific approach involving flow reduction strategies along with bypass surgery has the potential to eliminate or reduce the size of giant partially thrombosed BA aneurysms [63]. Consequently, the response of endothelial cells to shear stress not only initiates an inflammatory reaction but may also be crucial for sustaining the inflammation necessary for the maintenance, growth, and eventual rupture of the aneurysm.

Since the introduction of the WSS mechanotransduction theory by Fukuda et al. in 2000 [58], several researchers have proposed that increased WSS may be contribute to the development of cerebral aneurysm [22], [24], [64], [65]. Utilizing a microfluidic system, Nam et al. reported that morphological variations in the circle of Willis contribute to the formation of cerebral aneurysms under the circumstances of increased WSS [24]. Regions with a higher concentration of cerebral aneurysms exhibited a significant correlation with the magnitude of WSS [64]. CFD analysis on de novo human cerebral aneurysms indicated an association between high WSS and a high WSSG with cerebral aneurysm development [65]. However, direct evidence establishing that WSS sensing is responsible for cerebral aneurysm formation was lacking.

P2X4 purinoceptor plays a role in the shear stress response of vascular endothelial cells, which contributes to the vascular remodeling [66]. Fukuda et al. noted a significantly lower incidence of cerebral aneurysms in P2X4-knockout mice compared to wild-type mice [67]. In addition, when the P2X4 inhibitor paroxetine was administered to rats following cerebral aneurysm-inducing surgery, there was a significant reduction in the incidence and growth of aneurysms, along with a significant decrease in the expression of inflammatory factors contributing to aneurysm formation. These inflammatory factors include COX-2, MCP-1, tumor necrosis factor-α (TNF-α), iNOS, and interleukin-1β (IL-1β). These findings suggest that vascular endothelial cells respond to increased WSS-associated hemodynamics via triggering inflammation, which contributes to cerebral aneurysm formation. The data provide theoretical support for the validation of CFD simulations. Paroxetine may have potential for

the treatment of cerebral aneurysms, given its clinical use as an antidepressant, unrelated to P2X4 inhibition, and demonstrated lack of major safety concerns [68], [69].

2.2.4 A new hemodynamic element for initiation of aneurysm induction: mechanical stretch

Koseki et al. utilized a high-performance bio-camera to examine the initial changes in the cerebral arterial bifurcation of rats following cerebral aneurysm induction. They identified mechanical stretching of the vascular wall at the bifurcation [70]. In cell culture experiments, mechanical stretching was found to enhance the migration of macrophages. The data indicated that, alongside WSS, mechanical stretching could potentially act as a trigger for the formation of cerebral aneurysms. It should be noted that data supporting Hassler's theory [44] emerged more than 55 years later.

2.2.5 The vulnerability of the arterial wall

Apart from hemodynamics, the susceptibility of the cerebral artery may play an important role in the development of cerebral aneurysms. Various genetic disorders associated with extracellular matrix proteins have been identified as risk factors for the onset of cerebral aneurysms [71]. Lee et al. proposed a connection between the deficiency of the transcription factor Sox17 and the formation of aneurysms, alongside hypertension, stands out as one of the major risk factors for the development of cerebral aneurysms, although the precise understanding of the mechanism remains unclear. Smoking could potentially heighten the vulnerability of the cerebral artery. Starke et al. proposed that smoking contributes to the formation of cerebral aneurysms by activating NOX-dependent pathways [72].

Cerebral aneurysm induction in animal models, without an increase in hemodynamic stress, can be replicated through pharmacological and/or surgical means. For instance, cerebral aneurysms can be triggered by the stereotaxic injection of elastase into the cerebrospinal fluid at the basal cistern [73]. However, it should be noted that the locations of cerebral aneurysms induced by this method differ from those typically observed in human saccular cerebral aneurysms. Consequently, it is suggested that increased hemodynamic stress may be a crucial requirement for the saccular cerebral aneurysms' formation. Although the hemodynamic factors influencing aneurysm formation remain unclear, there is an association with high WSS and possibly mechanical stretching. Disturbed WSS lacking a clear direction resulted in sustained activation of proinflammatory and proliferative pathways, whereas laminar WSS with a defined direction lad to only transient activation of these pathways [74]. These findings

indicate that not only the magnitude of WSS but also WSS-associated disturbed flow contribute to WSS mechanotransduction and aneurysm formation. Additionally, the mechanism of WSS mechanotransduction triggering the expression of inflammatory factors under increased hemodynamic stress remains unclear.

2.3 CFD studies on the initiation of cerebral aneurysms

Since the late 1990s, CFD has been employed for blood flow analysis. Initially, due to the limitations of computer performance during that period, flow analysis was restricted to simple geometric pipe models. The increase in computational power in the 2000s facilitated the analysis of blood flow in anatomically realistic geometrical models of blood vessels and allowed the investigation of hemodynamic stresses on vascular lesions. Notably, with the improved capabilities of medical diagnostic imaging equipment like magnetic resonance imaging (MRI) and computed tomography (CT), researchers were able to achieve patient-specific blood flow simulations. Subsequently, efforts were directed toward devising personalized boundary conditions for simulations. Typical examples of inlet boundary conditions include literature-based values, values measured through techniques like by phase-contrast (PC) MRI, and values estimated based on hypotheses such as the constant WSS theory [75]. As for outlet boundary conditions, some researchers employ pre-distributed flow rates according to hypotheses like Murray's law, while others utilize a reduced-dimensional model of the peripheral vessel network based on the fractal nature of branching arteries. Additionally, fluid-structure interactions are achieved by considering the wall as an elastic rather than a rigid body.

Over the last two decades, blood flow analysis has witnessed significant progress. However, uncertainties persist regarding whether the use of complex boundary conditions and the implementation of fluid-structure analysis have truly contributed to identifying the initiation and growth factors of cerebral arteries. Recent studies have aimed to simplify blood flow simulations by avoiding complex boundary conditions, and identifying factors associated with the initiation and growth of cerebral aneurysms through statistical analysis of a large set of simulation data. While the future of blood flow analysis remains uncertain, it is likely to involve large-scale data analysis and artificial intelligence.

Below, we summarized the hypotheses involving hemodynamic factors proposed to be contributors to the initiation and growth of cerebral aneurysms.

2.3.1 High WSS and positive WSSG

Meng et al. [76], [77] deliberately induced the formation of an aneurysm in a dog by creating a bifurcated blood vessel through end-to-side anastomosis of two ICAs. They categorized the bifurcation region into three (I, collision area; II, acceleration area; III, recovery area) based on hemodynamic parameters. In region I, where the flow collided with the bifurcation, the WSS was observed to be low to normal. In this region, intimal thickening via growth remodeling was noted, along with the detection of fibronectin production. In region II, immediately adjacent to region I, the destruction of the inner elastic lamina and destructive remodeling including the loss of smooth muscle cells and endothelial cells were observed. In this region, the WSS and WSSG values were unusually high. Notably, the WSS increased from proximal to distal in region II, creating a positive gradient of WSS. These findings suggest that the combined impact of these hemodynamic stresses led to an excessive production of matrix metalloproteinases (MMP) by endothelial cells and smooth muscle cells, resulting in the destruction of the inner elastic lamina. While endothelial cells in arteries typically undergo proliferative remodeling resulting from chronic increases in WSS, the integration of a high WSS and positive WSSG caused endothelial cell dysfunction. This dysfunction led to the termination of proliferating cell nuclear antigen (PCNA) expression and the loss of smooth muscle cells. Based on these observations, Meng et al. [76], [77] proposed the hypothesis that destructive remodeling, induced by the combination of a high WSS and positive WSSG, leads to the thinning of the blood vessel wall, subsequently initiating cerebral aneurysm.

Various research groups tested the hypothesis involving high WSS and positive WSSG. Wang et al. [78] explored it from a molecular biology perspective, utilizing the same experimental system as Meng et al. [76], [77]. They discovered that the combination of a high WSS and positive WSSG resulted in a reduction in the expression of endothelial nitric oxide synthase (eNOS) and iNOS, which are involved in promoting nitric oxide (NO) production. Therefore, this led to an increased MMP production and activation. Importantly, these molecular changes were not observed in areas with a high WSS and negative WSSG, supporting the hypothesis proposed by Meng et al. [76], [77]. Further validation of the Meng hypothesis came from Metaxa et al. [22], who observed destructive remodeling at the bifurcation of the BA by ligating the rabbit common carotid artery (CCA) and increasing the flow into the BA.

Meng's hypothesis, initiated in 2011 and based on human cerebral aneurysms, utilized naturally occurring cerebral aneurysms in humans. Kulcsár et al. [65] establish a correlation

between hemodynamics and aneurysm formation by observing cerebral aneurysms that spontaneously occurred in the branch vessels of three human patients. They found that an aneurysm developed in the region characterized by high WSS and positive WSSG, aligning with Meng et al.'s findings [76], [77]. Alfano et al. [64], investigated blood flow at 114 bifurcations in 31 individuals in their reports, and Geers et al. [79] with their study of wall-type aneurysms, further supported Meng's hypothesis. Additionally, Watanabe et al. [80] compared hemodynamics in groups with and without aneurysms at ICA and found that the aneurysm group exhibited significantly higher values of WSS and WSSG compared to the non-aneurysm group.

The impact of geometric factors on the generation of high WSS and high WSSG has also been investigated. Kono et al. [16] proposed that the initiation of a particular class of cerebral aneurysm is induced by proximal stenosis. They created two pre-aneurysm models — one with stenosis and the other without — and compared their hemodynamics. The jet flow resulting from stenosis led to approximately a twofold increase in maximum WSS and a threefold increase in WSSG at the site of aneurysm initiation. Based on these reports, they concluded that proximal stenosis could be a factor in aneurysm initiation. Similarly, Lauric et al. [81] demonstrated that narrowing of an upstream vessel caused flow acceleration, accentuating the WSS and spatial gradient at the bifurcation apex, where aneurysms commonly form. Tutuncu et al. [18] proposed that the area exposed to direct flow impingement could be enlarged by a larger bifurcation angle, which results in abnormally increased hemodynamic stresses and potentially leading to aneurysm formation. Lauric et al. [82] assessed the impact of blood vessel curvature on hemodynamics, focusing on the inner carotid siphon. They prepared carotid siphon models with various curvature tightness. Flow simulations demonstrated that an elevated bend curvature caused oscillations and elevated values of proximal WSS and WSSG, subsequently leading to areas of stagnant flow and recirculation. This resulted in local conditions which were known to trigger destructive vessel-wall remodeling and formation of aneurysms.

2.3.2 Other hypotheses

Factors influencing the development of cerebral aneurysms extend beyond high WSS and normal WSSG. The oscillating shear index (OSI) is the index to which WSS changes direction within one cardiac cycle. It should be noted that the OSI is defined as a dimensionless parameter. The minimum OSI is 0, describing steady-state flow with WSS in one direction, and

the maximum number is 0.5, meaning flow with WSS in any direction. The relative residence time (RRT) reflects the duration blood resides near the vessel wall and results from a combination of a low WSS and high OSI. The gradient oscillatory number (GON), WSS divergence (WSSD), potential aneurysm formation index (AFI), inflow concentration index, shear concentration index, oscillation velocity index, low shear index, low shear area ratio, low shear area (LSA), and indices related to kinetic energy and turbulence allow for a more intricate analysis of blood flow.

The subsequent investigations focused on the parameters described in the preceding passage. Mantha et al. [83] introduced the AFI as a measurement for identifying regions of flow stagnation where WSS vectors aligned with endothelial cells throughout the cardiac cycle. They assessed AFI in paraclinoid aneurysms by virtually removing the aneurysms and reconstructing the parent artery. Their simulations demonstrated a region with relatively low and rotating WSS or large negative AFI at the location where aneurysm developed. Shimogonya et al. [84] employed virtual removal of aneurysms to examine hemodynamics in a pre-aneurysmal ICA. Among the investigated hemodynamic parameters, only GON, and not WSS, OSI, or AFI, showed correlation with aneurysm formation. Similarly, Chen et al. [85] conducted blood flow simulations in 22 human sidewall-type aneurysms, reporting higher WSS and GON at sites where aneurysms formed. Isoda et al. [86] concentrated on sidewall-type cerebral aneurysms in the human BA and observed high GON at the aneurysm sites. In contrast, Tanaka et al. [87] assessed WSS, WSSG, OSI, GON, and WSSD; among these, only WSSD demonstrated a correlation with the site of aneurysm initiation. The potential association of RRT with aneurysmal formation was investigated by Riccardello et al. [88]. Hemodynamic simulations were performed in 14 cases of sidewall aneurysm and the results revealed a negative connection between RRT and the occurrence of sidewall aneurysms. However, although researchers investigated various parameters, at this time point, no hemodynamic factor connected to the existence of all aneurysms has been identified.

2.4 CFD studies on the growth of cerebral aneurysms

There have been limited computational studies on the progression of cerebral aneurysms. Jou et al. [89] explored the association between cerebral aneurysm growth and hemodynamics via comparing the growth pattern of the aneurysms with the distributions of hemodynamic variables assessed through CFD simulations. Two patients with basilar aneurysms of similar size were monitored; one aneurysm exhibited significant growth (~ 3

mm/year), while the other remained stable during a 2-year follow-up. The growth pattern of the aneurysm wall was assessed by aligning aneurysm models constructed from MRA images at various time points. In the growing aneurysm, the area of growth correlated with a very low WSS (< 0.1 Pa), and a relatively large portion of the aneurysm surface with a WSS of < 0.1 Pa. In contrast, the stable aneurysm exposed a smaller surface region with a WSS of < 0.1 Pa. Over the aneurysm wall, both aneurysms exhibited a relatively uniform pressure distribution. Therefore, it is more likely that a low WSS rather than pressure, is responsible for the growth of cerebral aneurysms.

Boussel et al. [90] investigated the correlation between cerebral aneurysm growth and hemodynamics, particularly the WSS. They performed the study by making comparisons between the local radial displacement (growth) of the aneurysm wall and the time averaged WSS (TAWSS) measurement at the certain region. Seven patients with aneurysms (three BA, three ICA, and one middle cerebral artery aneurysms) were included, and patient-specific models were constructed based on MRA images at two time points (average 16.4 ± 7.4 months). The local radial displacement between the two time points was calculated by manually co-registering the models and assessing the displacement pixel by pixel. In that study, significant radial displacement was defined as exceeding 0.3 mm, equivalent to half of the MR pixel resolution. The mean radial displacement was 0.19 ± 0.34 mm, with 20% of wall-surface patches showing a displacement of ≥ 0.3 mm and 80% a displacement of < 0.3 mm. The TAWSS in the baseline geometry, assessed by CFD, was spatially averaged over areas with a displacement of ≥ 0.3 mm and < 0.3 mm. The spatial mean TAWSS values were 0.76 ± 1.51 and 2.55 ± 3.65 Pa, respectively ($p < 0.001$). These results indicate that the growth of cerebral aneurysms occurs in regions characterized by low WSS.

Sforza et al. [91] delved into the hemodynamic features of growing cerebral aneurysms with the method of comparing them with those of stable cerebral aneurysms. A total of 33 patient-specific CFD models were prepared, comprising 16 growing and 17 stable cerebral aneurysms. The models were constructed based on 3D-CTA or rotational angiography images and the hemodynamic parameters were compared. The criteria for a growing cerebral aneurysm included exhibiting a displacement of > 0.5 mm in any direction on at least 5% of the points on the aneurysm wall during follow-up observations. The criteria for a stable cerebral aneurysm were an aneurysm not exhibiting a displacement of > 0.5 mm for at least 9 months. The displacement of the aneurysm wall was assessed by aligning the parent vessels when

minimizing the distance between two models. The growing aneurysm group exhibited a significantly higher shear concentration index ($p = 0.03$) but lower shear rate ratio ($p = 0.01$), vorticity ratio ($p = 0.01$), and viscous dissipation ratio ($p = 0.01$) compared to the stable aneurysm group. Although not statistically significant, the growing aneurysm group showed a larger area under low WSS (LSA) ($p = 0.06$), and a greater aspect ratio ($p = 0.18$) than the stable aneurysm group. The definition of low WSS was the range of 1 SD below the mean WSS of the parent artery. The OSI showed no significant difference between the two groups ($p = 0.35$). The findings revealed that the hemodynamic environment of growing cerebral aneurysms may feature non-uniform WSS distributions, including areas of concentrated high WSS and extensive regions of low WSS.

As mentioned earlier, CFD studies have significantly advanced our comprehension of cerebral aneurysm hemodynamics. However, the hemodynamic factors linked to the initiation and growth of cerebral aneurysms remain unclear and requiring further exploration.

2.5 Conclusion

We reviewed the formation and growth of cerebral aneurysms, focusing on the involvement of hemodynamic stress on the arterial wall. First, we summarized the history of theories of the pathogenesis of cerebral aneurysm in chronological order from epidemiological and pathological viewpoints and based on data obtained from animal models of experimentally induced cerebral aneurysm. Enhanced hemodynamic stress may be a requirement for the formation of saccular cerebral aneurysm. The hemodynamic factors involved in aneurysm formation are unclear, although high WSS and possibly stretching are related. Also the mechanism of the WSS-induced mechanotransduction that induces the expression of inflammatory factors is unclear. Next, we briefly reviewed the history of studies of blood flow analysis by CFD, and summarized hemodynamics-based hypotheses on the initiation of cerebral aneurysms. Finally, we reviewed CFD studies on the growth of cerebral aneurysms, in which hemodynamic parameters were compared between growing and stable aneurysms, to highlight the hemodynamic characteristics associated with their growth. Remarkable progress has been made in CFD studies on the hemodynamics of cerebral aneurysms.

According to the review study, we got to know that early change of arterial bifurcation after cerebral aneurysm induction was observed [70]. To understand this change and stretch at bifurcation positions, we performed studies on correlations between vascular angles and aneurysms categorized by aneurysm locations (chapter 3).

The summarized history of applying CFD on WSS studies told us that CFD studies enabled researchers to get more detailed WSS information, from the maximum to the minimum. However, the definition of "low" WSS or "high" WSS varies. We would like to introduce the thinking of describing the relatively high or low WSS by representing them via WSS quantiles (chapter 4). In addition, we noted that despite the widely use of specific vessel models, many of the boundary conditions applied in CFD were generalized from reference papers. To figure out the influence of generalized boundary condition, we studied the difference and similarity of WSS brought by generalized and specific boundary conditions in chapter 5.

Chapter 3

Study on the correlation between vascular angles and aneurysm locations

Chapter 3   Study on the correlation between vascular angles and aneurysm locations

3.1 Introduction

Previous studies pointed out that vessel angles, especially wider angles could be related to aneurysm occurrence and development [18], [92], [93]. They reported the happening of early bifurcation changes after the aneurysm formation. Since the changing of angles plays an important role in the occurrence and development of aneurysms due to their effect on the hemodynamic situations, studies on vascular angles can contribute to the aneurysm early detection.

Therefore, in this chapter, we will study between the angles and aneurysms, and search for the correlation between vascular angles and aneurysm locations concerning on BA aneurysms.

3.2 Methods

3.2.1   Data collection

This study is a retrospective analysis based on patient data from the AneuX project [94], a multicenter database focusing on intracranial aneurysms. AneuX is a database including data collected and made available from the @neurIST project (www.aneurist.org) funded by the 6th framework program of the European Commission FP6-IST-2004-027703 and the AneuX project supported by the Swiss SystemsX.ch initiative and evaluated by the Swiss National Science Foundation. The authors extend their gratitude to the clinicians who diligently collected data at the Geneva University Hospital of Geneva, including Vitor Mendes Pereira, Hasan Yilmaz, Daniel Rüfenacht, Philippe Bijlenga, Karl Schaller, as well as to the @neurIST project for providing the infrastructure for data collection and sharing. The aim for this database is to work on using shapes as biomarkers for aneurysm disease.

In order to focus on patients with BA aneurysms only, several filters were applied based on following criteria: (1) Patients with either basilar tip aneurysms or basilar aneurysms other than the tip position; (2) Availability of clear visualization and reconstruction of the BA, PCA, and SCA region; (3) Patients with unruptured basilar aneurysms; (4) Availability of pre-treatment imaging data for basilar aneurysms.

After these filters were implemented, eleven cases of basilar tip aneurysms were incorporated in this study. Prior to treatment, medical imaging data for BA aneurysms were achieved through either CTA or MRA, depending on established medical protocols.

Among the basilar aneurysms other than the tip position, we notice that there exist two different types of aneurysms: one is happening alongside the basilar trunk, and another is still happening on the trunk but between the PCA and SCA (Fig.3-1). The happening of aneurysms alongside the basilar trunk are extremely rare and only one case was found after the filters. The reported happening ratio was 2.1% of all IAs [95]. The one happening between PCA and SCA was referred to as one type of SCA aneurysms according to some researchers [96], [97], and was named as 'BA type' or 'type a'. Some researchers also named it as basilar-SCA aneurysm [98].

In our study, we continued the name basilar-SCA aneurysm to separate them from other types of SCA aneurysms. The group including basilar aneurysms other than tip aneurysms was named "basilar-SCA group" and the trunk aneurysm was excluded because of the extremely small sample size (only 1 case).

To ensure this study a comprehensive comparison, we randomly selected eleven patients with aneurysms on vessels other than the BA. The selection criteria for this non-BA group were listed as follows: (1) The absence of BA aneurysms; (2) The inclusion of unruptured aneurysms at different locations; (3) Clear visualization and reconstruction of BA, PCA, and SCA regions.

To summarize, we employed in total 32 cases in this study, including 10 basilar-SCA aneurysms, 11 basilar tip aneurysms, and 11 non-BA aneurysms.

basilar-SCA   Trunk
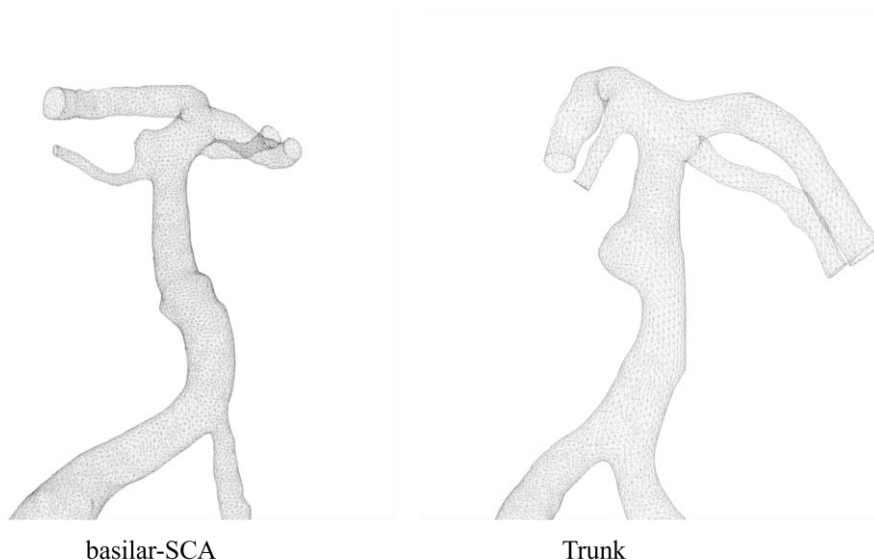
Figure 3-1 Two different types of basilar aneurysms other than tip position: two different types of basilar aneurysms: left is the aneurysm happing between the PCA and SCA; right another is the aneurysm happening alongside the basilar trunk.

3.2.2   Aneurysm model reconstruction

Because some cases were already reconstructed in the AneuX database, we conducted a retrospective search before we started our own reconstruction. We identified five cases meeting all our filters and had already undergone reconstruction. These five models were directly utilized in our analysis. For the remaining twenty-seven cases, models were constructed using 3D slicer 5.0.3 [99]. The process of the reconstruction was shown in Fig.3-2.

Side branches on BA, including the anterior inferior cerebellar artery (AICA) and posterior inferior cerebellar artery (PICA), were removed using Blender 3.1 [100]. The process was exhibited in Fig.3-3 and Fig.3-4.

3.2.3   Angle calculation

The definition of vascular angles was relied on the algorithms of branch splitting and centerline extraction functions utilized in "Vascular Modeling Toolkit" (VMTK) [101]. At first, centerlines were calculated. The word "centerline" here were determined as weighted shortest paths traced between extremal points[101]. Centerline are very powerful descriptors of the irregular vessel shapes. After the centerline extraction, each centerline point will contain the
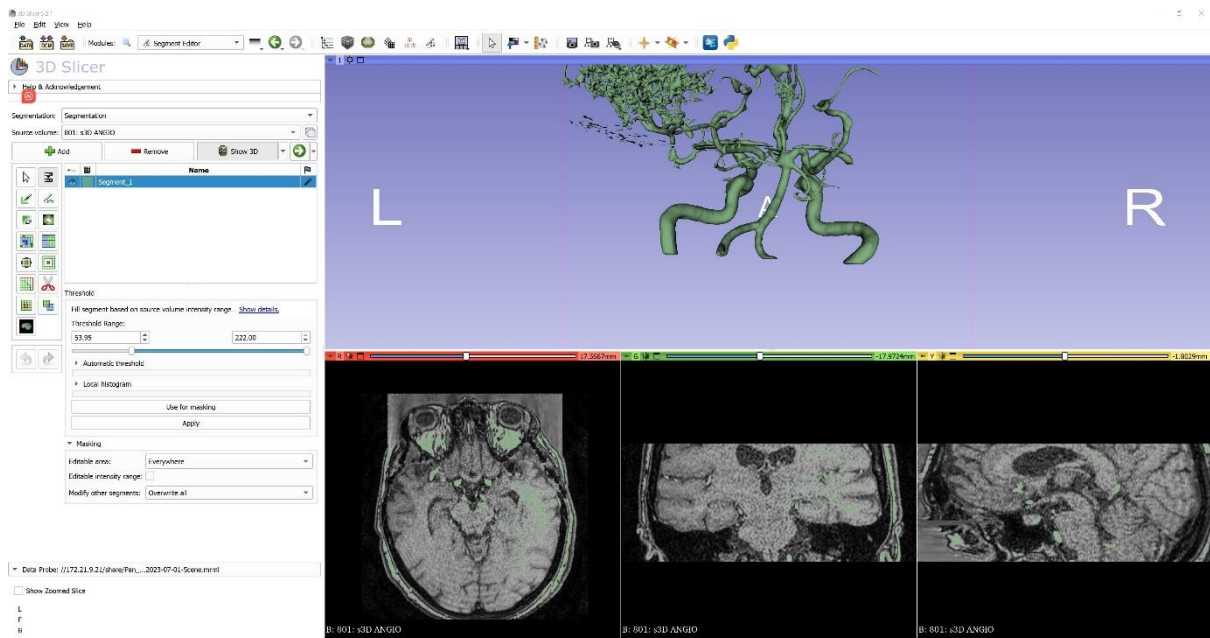
Figure 3-2 Segment editor in 3D slicer: the edit window for segmentation in the 3D slicer 5.0.3. The segmentation was performed based on threshold. The green zone represents the selected zone.
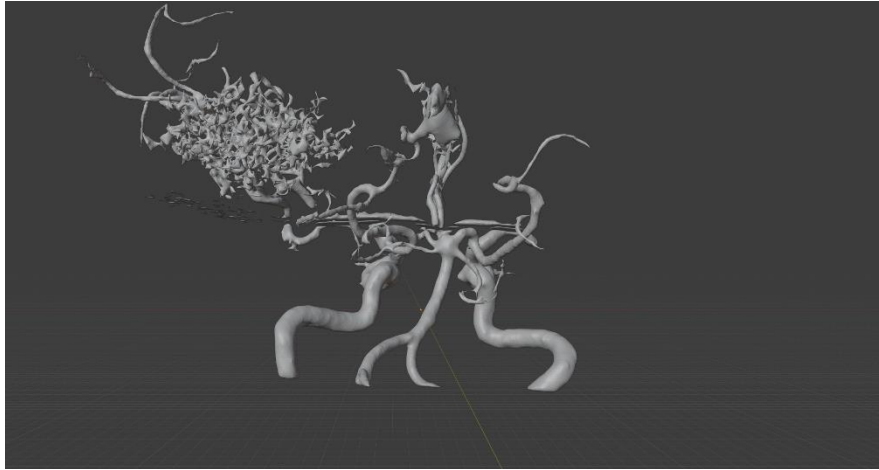
Figure 3-3 The model after segmentation: the reconstructed model after
the segmentation in 3D slicer.

coordinates of the centers of each maximal inscribed sphere alongside the whole vessel tubes, as shown in Fig.3-5.

If we combined all maximum inscribed spheres, we could construct tubes around each branch including the parent and daughter vessels, as shown in Fig.3-6. In Fig3-7, we exhibited one of the cases of the bifurcation region. The region where tubes intersect with each other was defined as bifurcation region. The detailed calculation algorithm can be found at VMTK website (vmtk.org), tutorial section.

In Fig.3-8, the bifurcation points and bifurcation vectors of this sample were exhibited. After we defined the bifurcation region, each centerline could be divided into three sections: the one before the bifurcation (marked in blue), the one inside the bifurcation zone (marked in
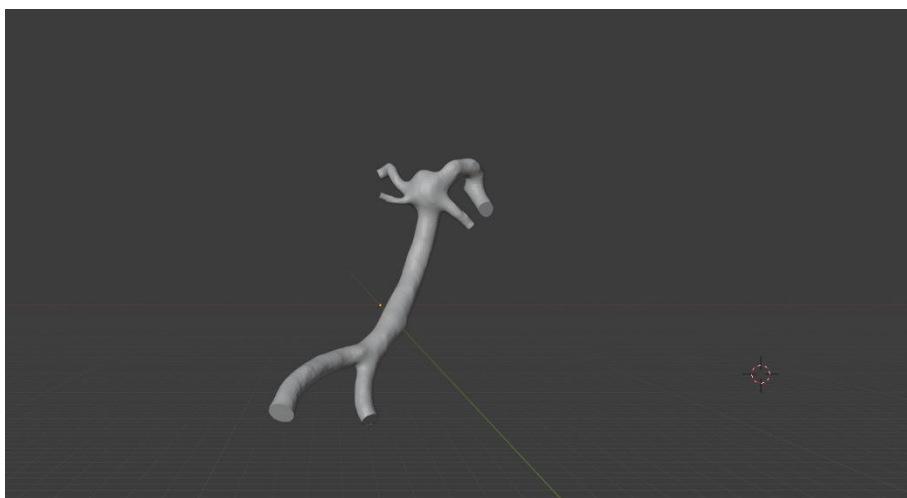

Figure 3-4 The model after side branches removed: the model with our
target vessels only. Branches including AICA and PICA were removed.
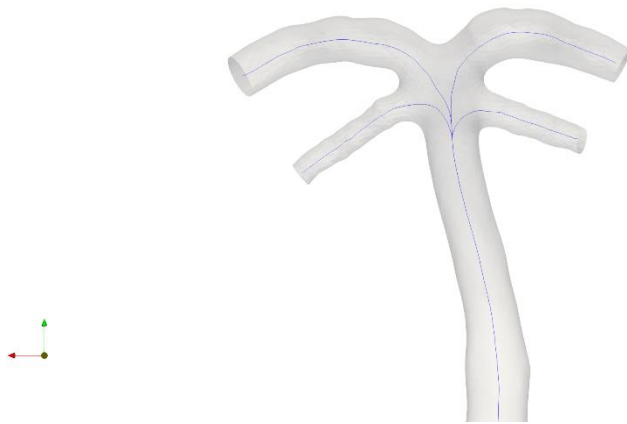
Figure 3-5 Centerlines: the centerlines extracted with VMTK. The blue lines exist in the middle of the branches are the centerlines.

green), and the one after the bifurcation zone (marked in red). The centerline points at the sites where the parent vessel or daughter vessels enter or leave the bifurcation region were called bifurcation points. The vectors at each bifurcation point, directing to the directions where branches enter or leave the bifurcation region were considered bifurcation vectors.

We defined the plane where daughter vessels branched off the parent vessel as the bifurcation plane. Each bifurcation of the daughter vessels has its own bifurcation plane. The bifurcation vectors were projected onto the bifurcation plane. The component of a bifurcation
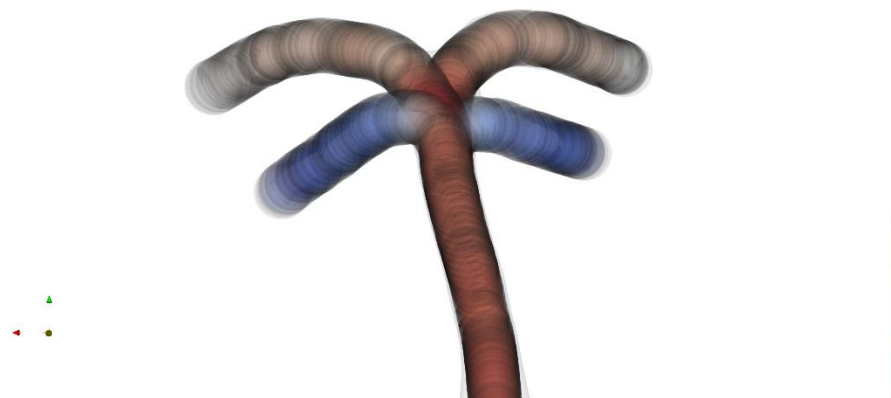
Figure 3-6 Tubes: the tubes constructed by combing maximum inscribed spheres alongside the whole vessel structure.
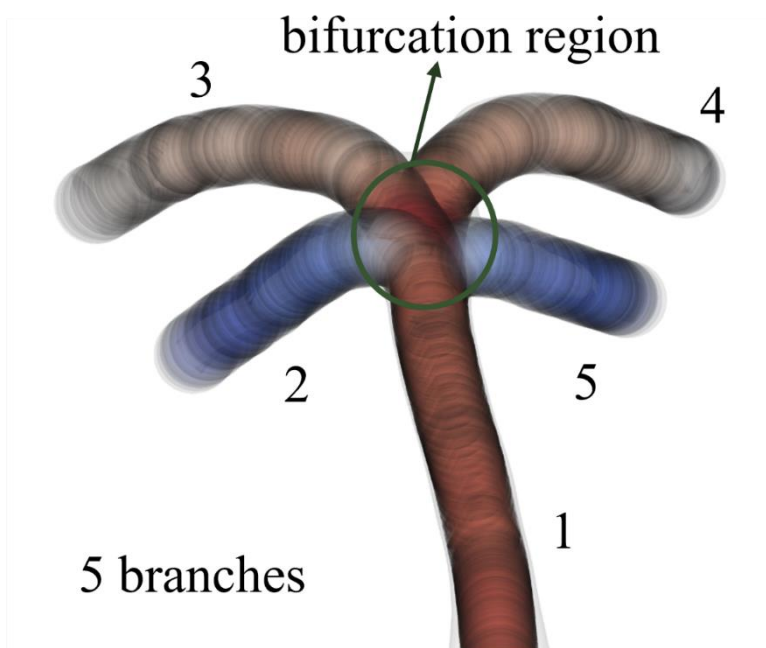
Figure 3-7 Bifurcation regions: an example of the bifurcation region. The area where branches intersect with each other was defined as bifurcation region.

vector projected on the bifurcation plane was referred to as an "in-plane vector". The component perpendicular to the in-plane vector was called as the "out-of-plane vector" (Fig.3-9).

In our study, vascular angles were defined as three different types: bifurcation angles, in-plane angles and planarity. The angles between two in-plane vectors were defined as "in-plane angles", and angles between two bifurcation vectors were called "bifurcation angles". The angles between two out-of-plane vectors were referred to as "planarity" [102] (Fig.3-10).

We calculated the angles between two PCAs (Fig.3-11 e) and the angles between PCA and SCA (Fig.3-11 a and b), and SCA and BA (Fig.3-11 c and d) on each lateral side. The words "left" and "right" were not used this time. Instead, we employed the terms "larger and smaller angles". This is because, especially in basilar-SCA aneurysms cases, the aneurysm's position significantly influences the dominant side. The angle with the greater measurement between a and b was defined as the "larger PCA-SCA angle," while the angle with the smaller measurement was referred to as the "smaller PCA-SCA angle". Similarly, the SCA-BA angles (c and d in Fig.3-10) were compared and categorized as the "larger SCA-BA angle" and the "smaller SCA-BA angle". Both pairs of angles (PCA-SCA angles and SCA-BA angles) were compared separately. Additionally, all three types of angles, namely "in-plane
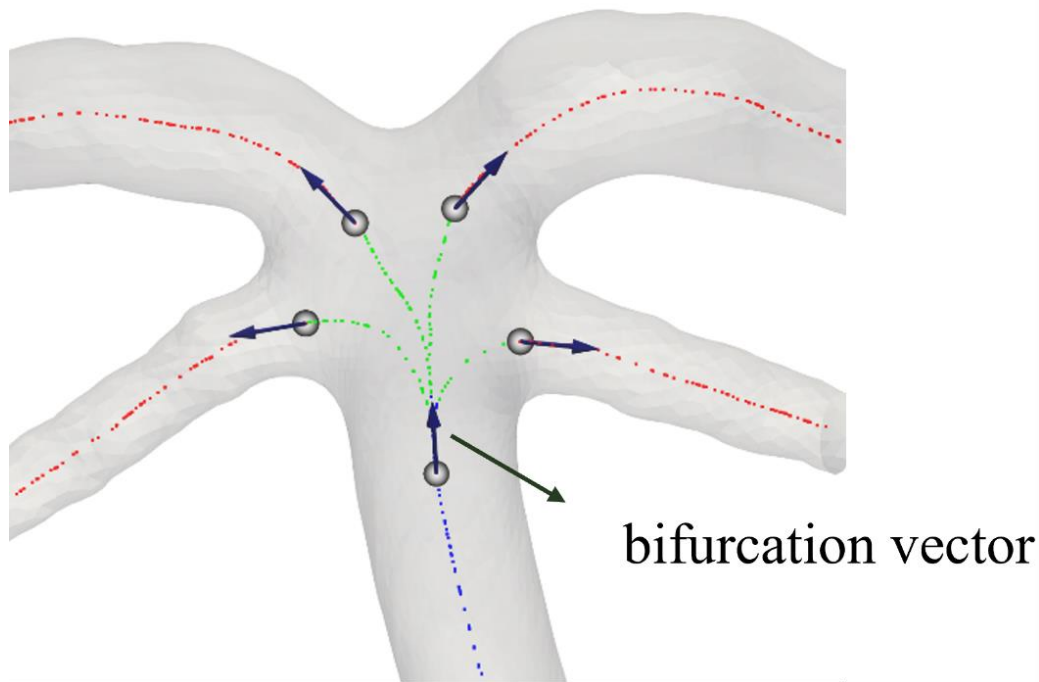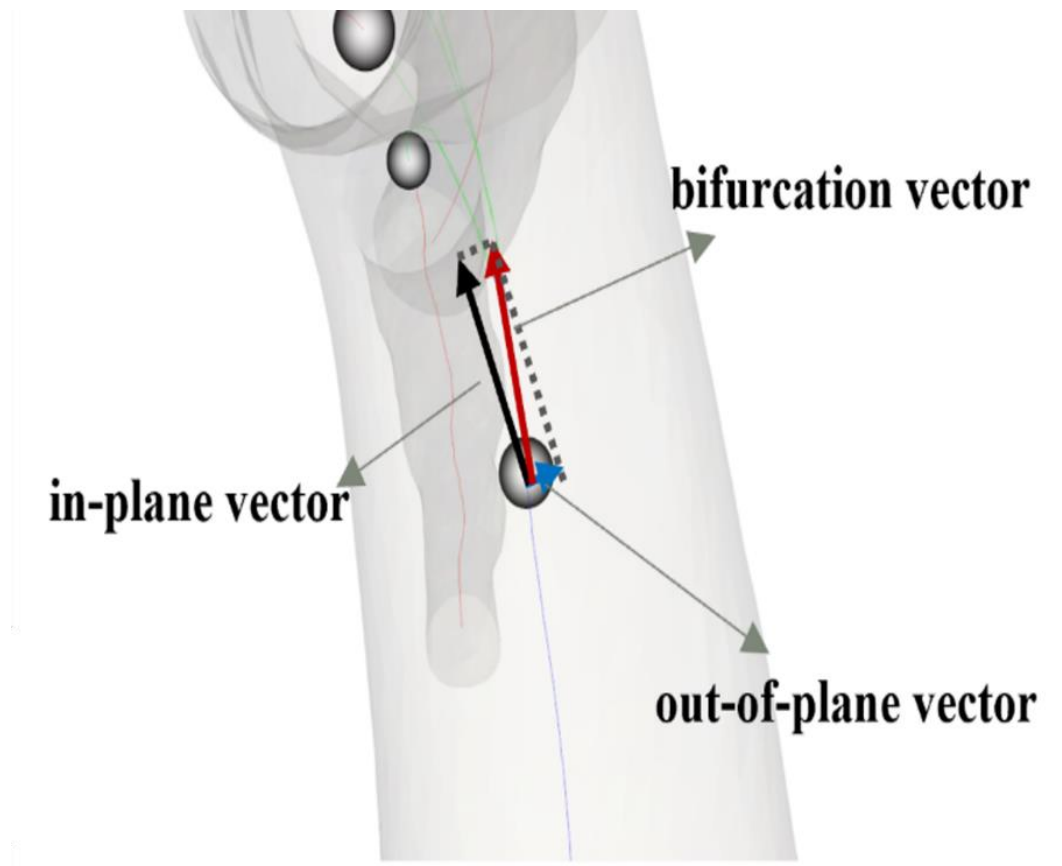
Figure 3-8 Bifurcation vectors: the bifurcation vectors together with the bifurcation points. The whole vessel structure was divided into five branches. The green region was the bifurcation region. The center point at the site where parent or daughter vessel enter or leave the bifurcation region was called bifurcation points. The direction of which the branches leave or enter this bifurcation region was defined as bifurcation vector, marked in blue arrows.

angles", "bifurcation angles", and "planarity", were independently compared. Consequently, in some cases, the larger PCA-SCA in-plane angle could be on the right side while the larger PCA-SCA planarity was on the left.

3.2.4 Data analysis

We performed a statistical analysis to study the geometric differences among the three categories (basilar tip aneurysm, BA-SCA aneurysm, and the non-BA aneurysm groups). At first, we evaluated the homogeneity of variances and distribution for each angle. If the data satisfied the assumption of homogeneity of variances and were normal distributed, we conducted a one-way analysis of variance (ANOVA). As long as the significant differences among the means were detected, we conducted pairwise multiple comparisons to further identify which pair of the groups were showing significant differences. During the multiple comparisons, the Bonferroni t-test was employed.

Figure 3-9 Projected components of bifurcation vector: the decomposition of the bifurcation vectors. For each bifurcation vector, we projected them onto the bifurcation plane. The component on the plane was defined as in-plane vector, and the component perpendicular to the plane was defined as out-of-plane vector.

When the assumption of homogeneity of variances was not satisfied or the data was not normal distributed, we performed a Kruskal-Wallis analysis instead of ANOVA. If any significant differences were identified, pairwise comparisons were conducted. Again, the significance level was adjusted using the Bonferroni correction. The analysis was performed using IBM SPSS Statistics 28.0 (IBM Corp. Released 2021. IBM SPSS Statistics for Windows, Version 28.0. Armonk, NY: IBM Corp). The whole process was listed in Fig.3-12.
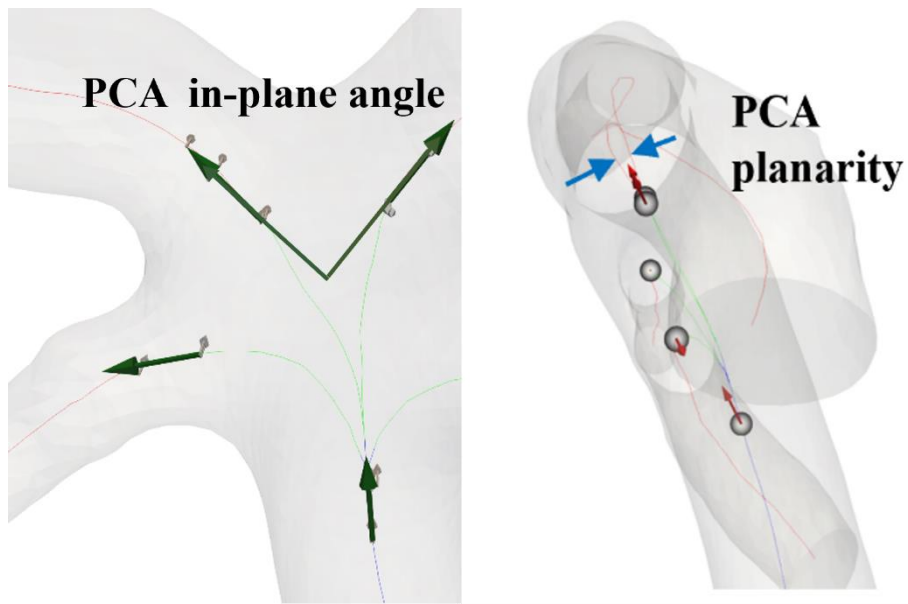
Figure 3-10 In-plane angles and planarity: the examples of the in-plane angles and the planarity between two PCAs. The angle between two in-plane vectors (shown in green arrows) was referred to as in-plane angle, and the angle between two out-of-plane vectors was defined as planarity.
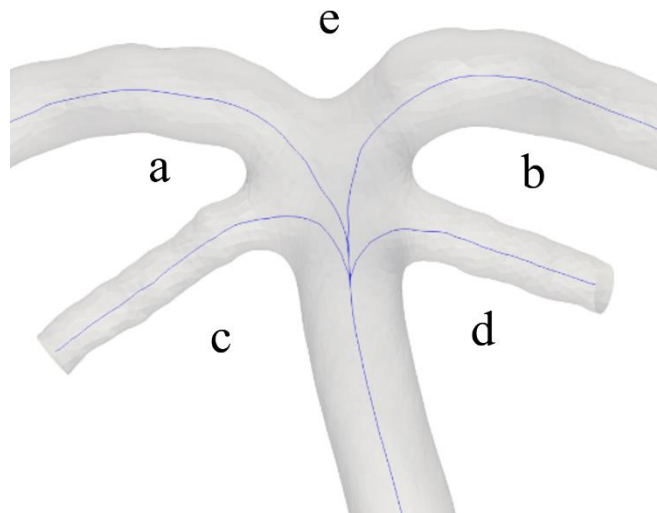
Figure 3-11 Calculated angles: all angles calculated in this study. The number a, b, c, d, e represented left PCA-SCA angle, right PCA-SCA angle, left SCA-BA angle, right SCA-BA angle and PCA angle separately.

comparison among three groups

| Homogeneity of variances | Both yes → | ANOVA |
| Normal distribution | Either is no → | Kruskal-Wallis analysis |

comparison between two groups

if significant → Pairwise multiple comparisons (Bonferroni *t*-test)
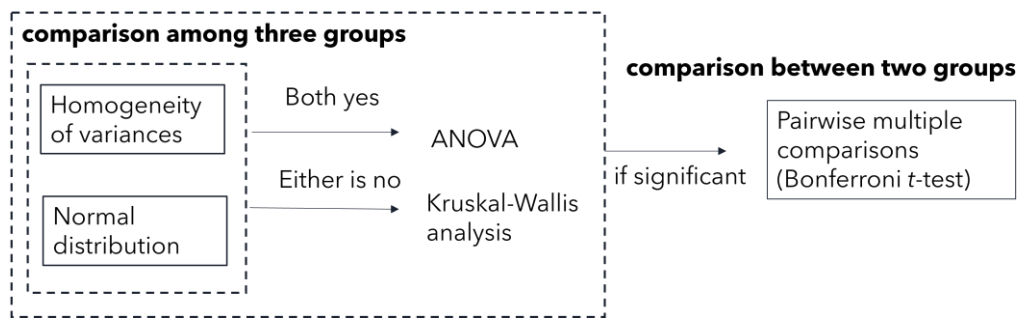
Figure 3-12 Data analysis: the process of the data analysis applied in this chapter.

3.3 Results

3.3.1 Study group characteristics

Our study cohort consisted of thirty-two patients, including eleven individuals with basilar-SCA aneurysms (from 39 to 64 years mean age: 51.1 ± 8.3 years), eleven patients with basilar tip aneurysms (from 44 to 70 years, mean age: 57.3 ± 9.0 years), and eleven patients with non-BA aneurysms (from 38 to 83 years, mean age: 58.7 ± 13.1 years). Among the three groups, no significant difference in patient ages was found.

The maximum, minimum, mean and standard deviation of all angles were listed in Table 3.1 and Table 3.2. Boxplots shown in Fig.3-13 illustrate all calculated angles based on group and angle site categorize. Among all angles, we would like to note the following groups:

(1) PCA bifurcation angles ranged from 38.98° to 132.11° (with a mean of 82.89° ± 32.75°) in the basilar-SCA group. The same angles ranged from 76.88° to 154.47° (with a mean of 114.02° ± 25.13°) in the basilar tip group. In the non-BA group, these angles ranged from 74.05° to 129.82° (mean of 97.78° ± 21.44°). Notably, the basilar tip group exhibited the largest mean PCA bifurcation angles.

(2) Regarding the larger PCA-SCA bifurcation angles, the basilar-SCA group displayed a range of 43.80° to 162.57° (mean 99.02° ± 38.53°). The same angles in the basilar tip group ranged from 33.89° to 79.82° (mean 65.63° ± 14.54°), and when it comes to the non-BA group, the angles ranged from 45.47° to 94.23° (mean 69.85° ± 17.23°). From the boxplots, considerable individual variations in planarity could be observed among the two PCAs, larger SCA-BA and larger PCA-SCA angles (Fig.3-13) when compared to the in-plane and bifurcation angles.

3.3.2 Data analysis

Based on data characteristics (the homogeneity of variances and whether normal distributed or not), the PCA-SCA angles, planarity of larger SCA-BA, smaller SCA-BA and PCA were compared with Kruskal-Wallis test and the other angles were compared with ANOVA. Significant differences were found between the PCA and the larger PCA-SCA bifurcation angles. The two groups existing these differences were the basilar-SCA group and the basilar tip group (Table 3.3).

The PCA bifurcation angles were found to be significantly larger in the basilar tip group than those in the basilar-SCA group. Conversely, the larger PCA-SCA bifurcation angles showed a significantly greater mean value in the basilar-SCA group than in the tip group. No significant differences were observed in the remaining comparisons.

3.3.3 Aneurysm size and angles

The collar size and maximum diameter of the basilar aneurysms were also gathered and the results of aneurysm size versus PCA bifurcation or larger PCA-SCA bifurcation angles were exhibited from Fig.3-16 to Fig.3-19. One case in the basilar-SCA group did not have its maximum diameter record in the database. Data of other cases were all collected. It could be observed that the both collar size and maximum diameter of the aneurysms in basilar-SCA group showed strong correlations with each other. The correlations between aneurysm size and angles in basilar tip groups with the PCA bifurcation angles were also significant. However, the aneurysm size and larger PCA-SCA in tip groups were not correlated.

Table 3-1Mean and standard deviation of all calculated angles

geometric parameter	basilar-SCA aneurysm		basilar tip aneurysm		control group	
	mean	SD	mean	SD	mean	SD
PCA						
in-plane angle	92.78°	28.65°	115.90°	28.23°	102.40°	23.34°
planarity	7.67°	21.14°	4.49°	14.90°	2.32°	7.69°
bifurcation angle	82.89°	32.75°	114.02°	25.13°	97.78°	21.44°
PCA-SCA						
larger in-plane angle	94.65°	42.19°	63.64°	12.83°	68.08°	18.15°
larger planarity	3.44°	7.38°	6.33°	15.02°	4.74°	13.16°
larger bifurcation angle	99.02°	38.53°	65.63°	14.54°	69.85°	17.23°
smaller in-plane angle	45.91°	29.93°	42.41°	11.37°	45.20°	16.22°
smaller planarity	0.00°	0.00°	0.00°	0.00°	0.77°	2.55°
smaller bifurcation angle	51.97°	26.01°	45.93°	12.22°	48.09°	13.74°
SCA-BA						
larger in-plane angle	129.82°	27.91°	122.84°	20.48°	117.80°	14.80°
larger planarity	7.12°	15.05°	10.82°	19.62°	4.52°	14.98°
larger bifurcation angle	130.57°	26.37°	123.71°	19.73°	117.73°	14.52°
smaller in-plane angle	97.44°	15.80°	92.38°	17.79°	95.01°	10.75°
smaller planarity	0.00°	0.00°	0.00°	0.00°	0.00°	0.00°
smaller bifurcation angle	98.08°	15.42°	92.47°	18.21°	95.68°	12.24°

Table 3-2 Maximum and minimum of all calculated angles

geometric parameter	basilar-SCA aneurysm		basilar tip aneurysm		control group	
	maximum	minimum	maximum	minimum	maximum	minimum
PCA						
in-plane angle	132.91°	44.17°	156.17°	75.95°	137.79°	73.37°
planarity	67.25°	0.00°	49.40°	0.00°	25.51°	0.00°
bifurcation angle	132.11°	38.98°	154.47°	76.88°	129.82°	74.05°
PCA-SCA						
larger in-plane angle	167.84°	34.87°	79.88°	34.17°	93.27°	45.90°
larger planarity	20.07°	0.00°	46.49°	0.00°	43.66°	0.00°
larger bifurcation angle	162.57°	43.80°	79.82°	33.89°	94.23°	45.47°
smaller in-plane angle	108.13°	16.11°	59.17°	19.07°	65.74°	5.88°
smaller planarity	0.00°	0.00°	0.00°	0.00°	8.47°	0.00°
smaller bifurcation angle	100.19°	21.52°	66.17°	21.61°	74.81°	32.46°
SCA-BA						
larger in-plane angle	171.66°	89.93°	164.86°	90.68°	136.43°	96.23°
larger planarity	47.45°	0.00°	49.40°	0.00°	49.68°	0.00°
larger bifurcation angle	168.07°	89.05°	157.84°	90.74°	135.41°	96.41°
smaller in-plane angle	126.06°	78.49°	119.16°	67.36°	114.62°	77.08°
smaller planarity	0.00°	0.00°	0.00°	0.00°	0.00°	0.00°
smaller bifurcation angle	126.07°	79.44°	122.31°	67.37°	118.01°	77.32°

boxplot of the in-plane anlges in three groups

boxplot of the planarity in three groups

boxplot of the bifurcation anlges in three groups
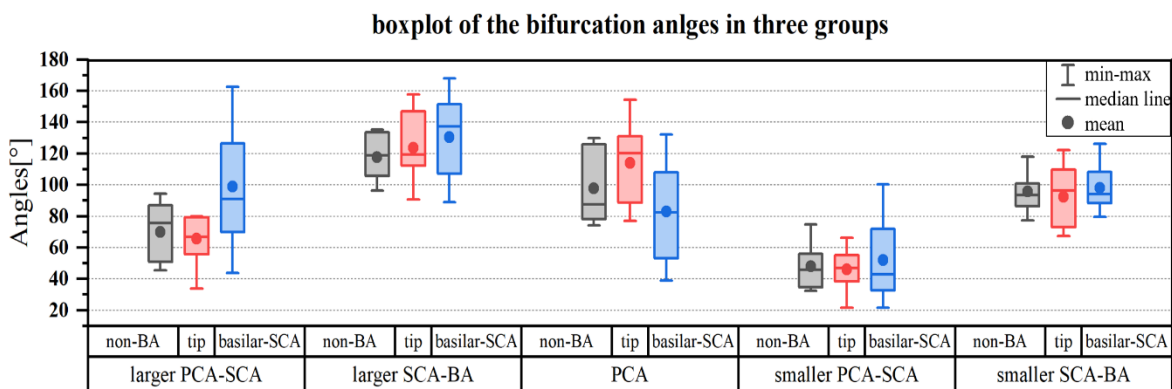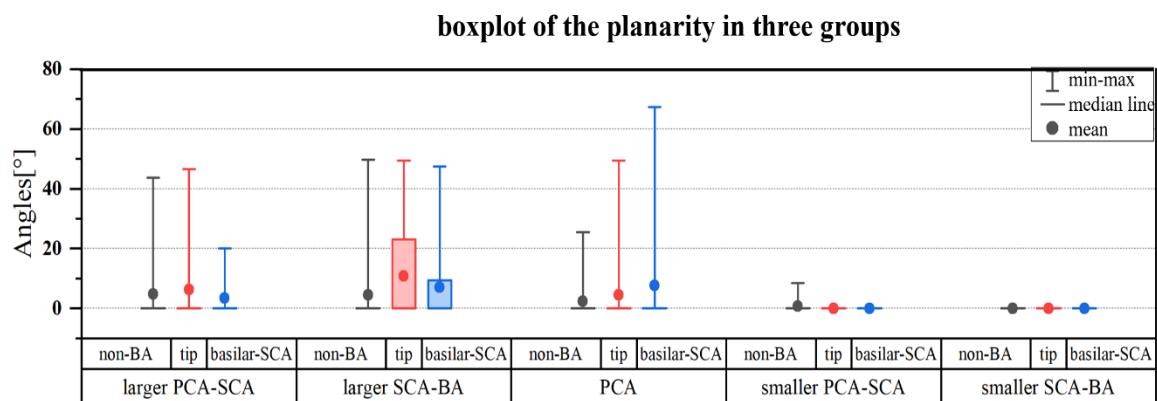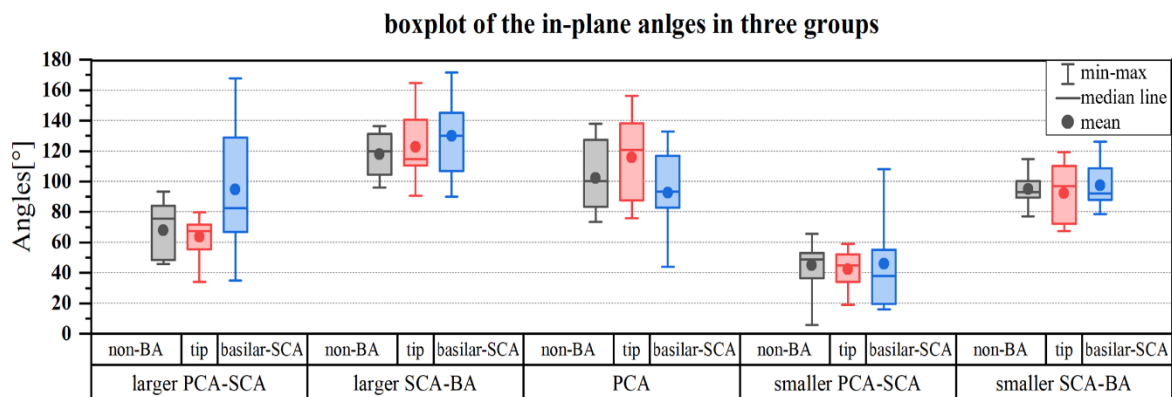
Figure 3-13 Boxplots of all extracted angles: all calculated angles with boxplots. The groups were shown via the categorize of angle sites and aneurysm sites. The y-axis of all plots means the angle measurement.

Table 3-3 Summary of data analysis

geometric parameter	statistical analysis	*p* value	multi comparison results*
PCA			
in-plane angle	ANOVA	0.156	
planarity	Kruskal-Wallis test	0.916	
bifurcation angle	ANOVA	0.040	basilar-SCA group and tip group: *p*= 0.036
PCA-SCA			
larger in-plane angle	Kruskal-Wallis test	0.106	
larger planarity	Kruskal-Wallis test	0.877	
larger bifurcation angle	Kruskal-Wallis test	0.039	basilar-SCA group and tip group: *p*= 0.042
smaller in-plane angle	Kruskal-Wallis test	0.642	
smaller planarity	Kruskal-Wallis test	0.479	
smaller bifurcation angle	Kruskal-Wallis test	0.998	
SCA-BA			
larger in-plane angle	ANOVA	0.449	
larger planarity	Kruskal-Wallis test	0.157	
larger bifurcation angle	ANOVA	0.372	
smaller in-plane angle	ANOVA	0.746	
smaller planarity	Kruskal-Wallis test	0.611	
smaller bifurcation angle	ANOVA	0.709	

*p values listed in this column were adjusted by Bonferroni correction.

3.4 Discussion

In this chapter, we introduced our study on the correlations between vascular angles and aneurysm sites by doing research on differences existing in vascular angles when categorized by aneurysm sites.

We conducted a retrospective study of the angles including PCA, PCA-SCA, and SCA-BA in individuals with basilar-SCA and basilar tip aneurysms, and patients with non-BA aneurysms were also involved. Our results revealed that significant differences exist in PCA and PCA-SCA angles between the basilar-SCA and basilar tip aneurysm groups. The significant differences identified further validate the hypothesis proposed by previous studies [18] that aneurysm locations exhibit preferences, and larger bifurcation angles may play a role in contributing to this phenomenon.

3.4.1 Differences between basilar tip and trunk groups

The basilar-SCA group exhibited a larger PCA-SCA bifurcation angle compared to the other two groups. This trend can also be observed directly (Fig.3-13). Prior researches have suggested that aneurysms tend to happen in regions with larger bifurcation angles [18], [92],

[103], [104]. This theory was explored in different arteries, including the MCA, BA, and ICA. In this chapter, the side with the larger PCA-SCA bifurcation angle roughly aligned with the side where aneurysms were detected.

The significant differences in the larger PCA-SCA bifurcation angles, without a corresponding trend observed on the opposite side (the smaller PCA-SCA bifurcation angle), indicate the asymmetry of the PCAs in the basilar-SCA group. In this chapter, the terms "larger" or "smaller" angles were utilized. The majority of relatively larger PCA-SCA angles among all models were observed in the basilar-SCA group. This explains why, when categorized into basilar-SCA and tip groups, the differences in larger PCA-SCA angles yielded significant results.

In contrast, the PCA bifurcation angles were significantly larger in the tip group compared to the basilar-SCA group. Our study revealed the following tendency: basilar tip group > non-BA group > basilar-SCA group. This trend directly contrasts with the observed trend in larger PCA-SCA bifurcation angles. Previous research has proposed that basilar apices with larger angles lead to a longer distance for blood flow laminarization in the distal position of bifurcation compared to those with sharper angles [18]. This implies that those vessel walls without protected cell designs are exposed to high wall shear stress or vortices, which can contribute to the aneurysm formation [64], [105], [106].

The PCA angles in our basilar-SCA aneurysm group were relatively smaller when compared to those in previous studies [92], [104]. The in-plane PCA angles in our basilar-SCA group ranged from 44.17° to 132.91°, with an average angle of 92.78°. In addition, it did not exhibit a significant difference when compared to the non-BA group. This situation was also evident in the morphologies if we observe the basilar tip and the non-BA aneurysm group directly (Fig.3-14). From Fig.3-13, it could be observed that most of the PCAs with aneurysms in-between still had similar shapes to those in the non-BA group. The reason for this similarity could be that even patients in the non-BA group were patients with aneurysms, although in different locations other than BA. F Tütüncü reported the trend of wider PCA angles with increasing age was observed. This phenomenon was observed even in patients without BA aneurysms (but had aneurysms in other positions) according to their study [18].

The manifestation ratio of basilar-SCA aneurysms is reported to be relatively lower compared to BA tip aneurysms [107], [108]. To the best of our knowledge, separating basilar-
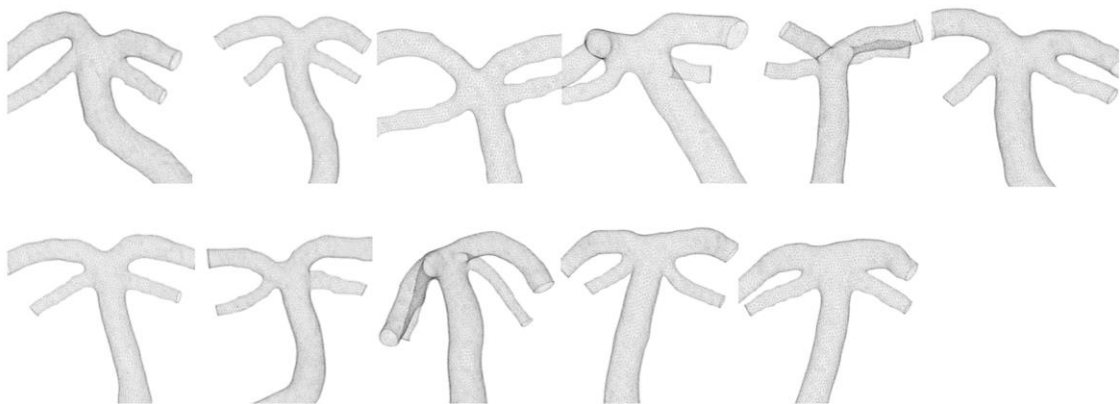
basilar –SCA aneurysms
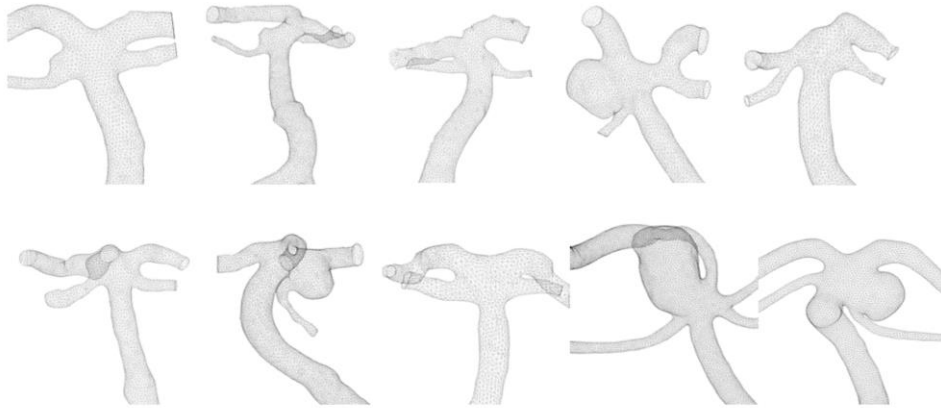
basilar tip aneurysms
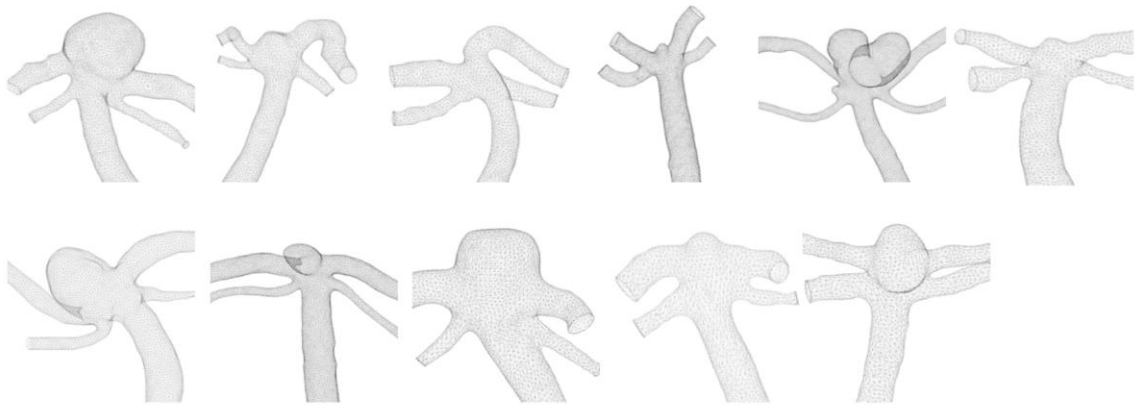
non-BA aneurysm group

Figure 3-14 A posterior view of all reconstructed models: all reconstructed models used in Chapter 3. All models shown here are observed from a posterior view.

SCA and basilar tip aneurysms was seldom considered in previous studies on basilar aneurysms. The differences in vessel angles between BA aneurysms and non-BA vessels reported in those studies might be primarily caused by BA tip aneurysm. In this chapter, we included a nearly equal number of patients in the basilar-SCA and basilar tip groups. The results revealed the significant differences in angles around the BA apex between the BA tip and basilar-SCA groups. Additionally, the non-BA group showed angles falling within the range observed for both PCA angle and PCA-SCA angle between the basilar tip and basilar-SCA groups.

The absence of significant differences between basilar aneurysms and non-BA groups, which was reported in previous studies [92], could be the results of the relatively small sample size. However, the differences between basilar tip and basilar-SCA groups were large enough to be detected. This further emphasized the correlations between the aneurysm sites and vascular angles.

3.4.2 Separating PCA-BA into PCA-SCA and SCA-BA

Considering PCA-BA as PCA-SCA and SCA-BA made the detailed discussions on angle variations around the BA apex possible (Fig.3-15). Interestingly, SCA-BA angles among all three groups yielded no significant results in our database. Previous studies suggested smaller PCA-BA angles in patients with basilar aneurysm compared to non-BA patients [92]. Since significant differences in PCA-SCA angles between the tip and basilar-SCA groups was observed, it can be inferred that the variability in PCA-BA angles was primarily affected by the differences in PCA-SCA angles, while SCA-BA angles had a minor effect.

Notably, our data revealed that a seemingly symmetric nature in SCAs. Planarity exhibited considerable individual variances, especially in the PCA angles. In contrast, PCA-SCA planarity on both lateral sides and the smaller SCA-BA planarity showed relatively consistent geometries. The mean planarity value of them was near 0.00°. This data validated that both SCAs were nearly aligned on the same plane. Although the reason why the SCAs were displaying such a consistent morphology remains unknown, uncovering this explanation could offer us further insights into the development of aneurysm formation mechanisms and contribute to pre-diagnosis of aneurysm locations.

### 3.4.3 Aneurysm size and angles

For most of the studies, it could be really hard to tell the changes of angles and the aneurysm initiation which comes first. Some researchers found that even in patients with really small size of aneurysms or with aneurysms at other locations other than at BA, they still tend

to have larger angles [18]. In that case, they proposed the idea that the changes may happened before the initiation. In contrast, some researchers proposed the opposite and claimed that the angle changes happened after the aneurysm formation [109]. They gathered patients with follow up data from multiple centers and promoted that the changes of angles may be secondary to the IA formation.

In our study, since the database collected all patients with aneurysms, it is also hard for us to tell the timeline of the angle changes and aneurysm formation. However, we found the significant correlations existing between the aneurysm size and angles. Especially in basilar-SCA groups, the angles were not only correlated with larger PCA-SCA angles, which were angles of the aneurysm happening position, but also correlated with PCA angles (Fig.3-16, Fig.3-17). On the other hand, basilar tip aneurysm size showed correlations only with the PCA angles but no larger PCA-SCA angles (Fig.3-18, Fig.3-19).

3.4.4 Limitations

Both CTA and MRA images were included during our reconstruction process. The 3D models reconstructed from medical images showed variability dependent on the operators [110]. To decrease bias arising from the geometry reconstruction process, we applied uniform threshold criteria on all our models. We allowed for the visualization of some parts of the AICA during the reconstruction process because the diameter of AICA was almost the same as the
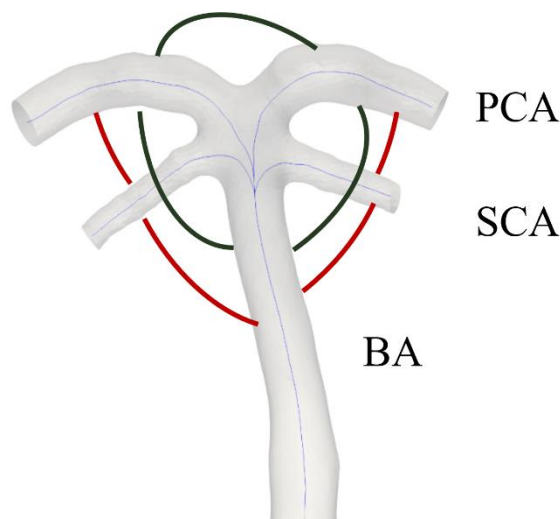
Figure 3-15 Separated PCA-BA angles This figure is made to explain the separation of PCA-BA angles. The PCA-BA angles were commonly considered in previous studies. We separated them into PCA-SCA and SCA-BA angles this time (marked with red lines).

pixel size of our medical images. Additionally, angle extraction relied on centerlines to mitigate the impact of different resolutions. Further correlations between basilar aneurysms and vessel angles can be expected with a larger patient cohort in the future.
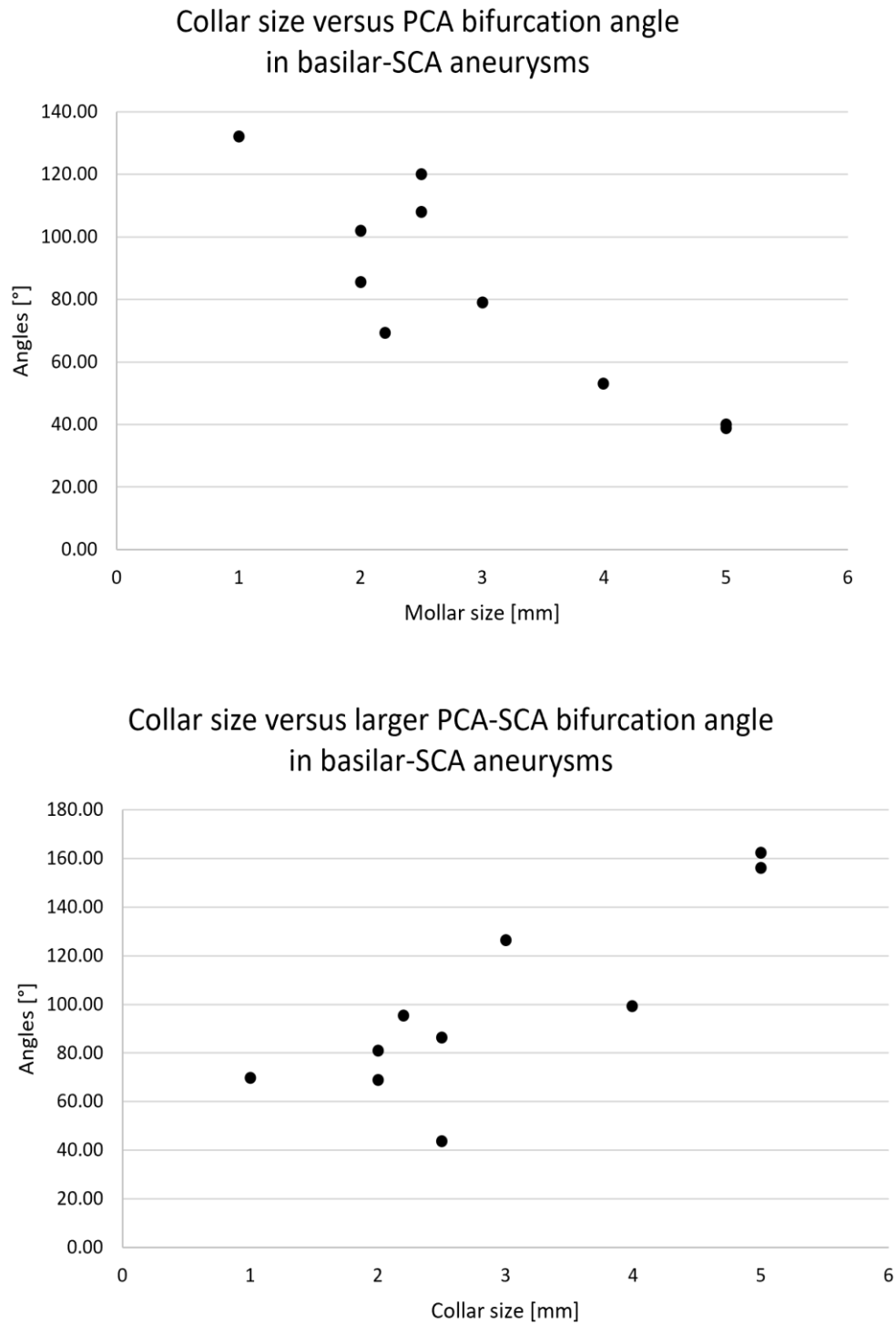
Figure 3-16 Collar size and angles in basilar-SCA aneurysm group

3.5 Conclusion

In this chapter, we introduced our study on the correlations between vascular angle changes and aneurysm location. By separating basilar aneurysms into basilar tip and basilar-SCA groups, significant differences were observed between the two groups. The results revealed that with the existence of aneurysms, bifurcations with more than two branches such
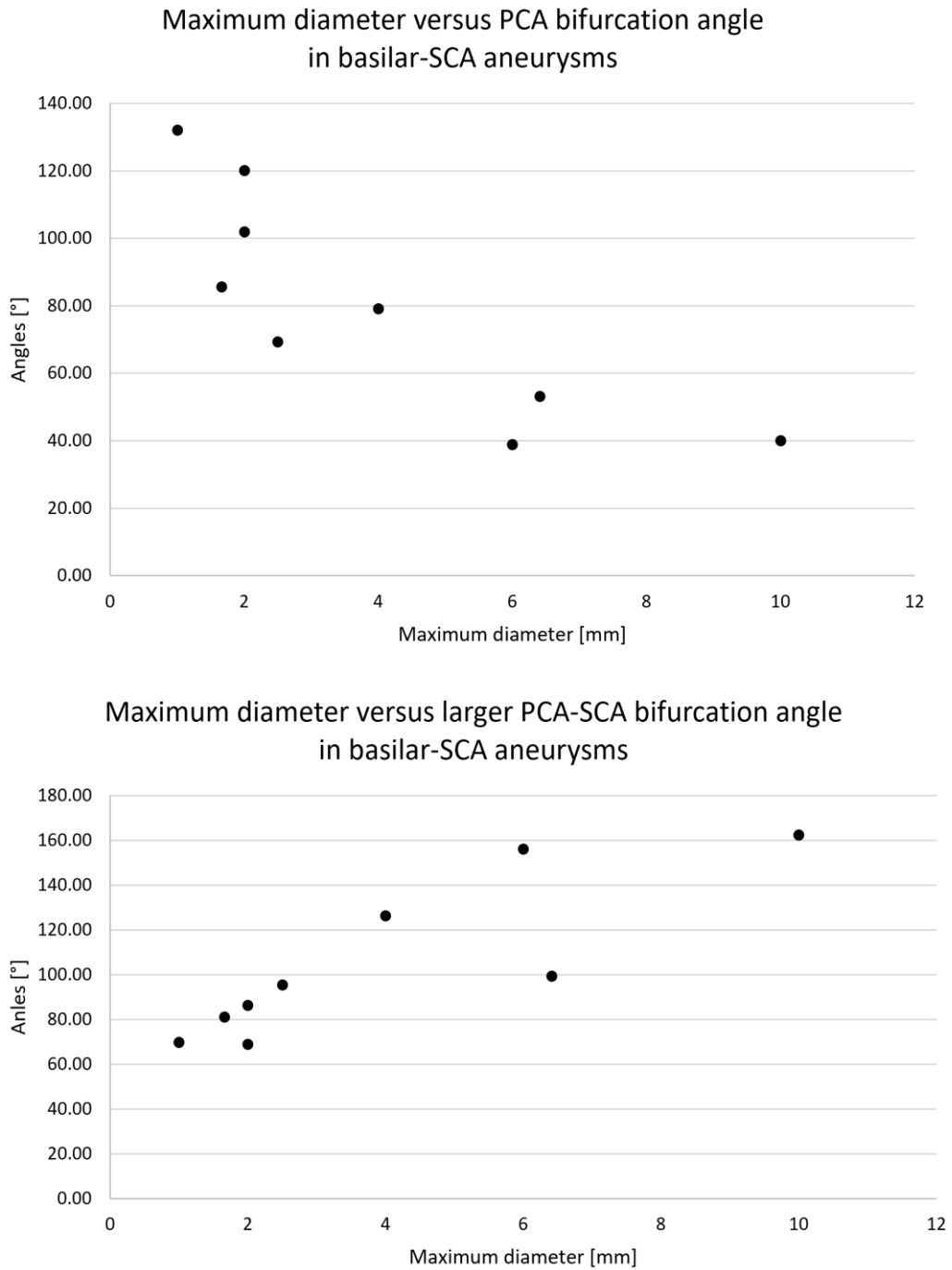
Figure 3-17 Maximum diameter and angles in basilar-SCA aneurysm group

as the basilar apex will have various angle changes according to the aneurysm location. In addition, by separating PCA-BA angle into PCA-SCA and SCA-BA, we observed that with the IA existence, the movements of the branch vessels were different. These findings implied that the happening of angle changes can be potential factors for IA early detection.
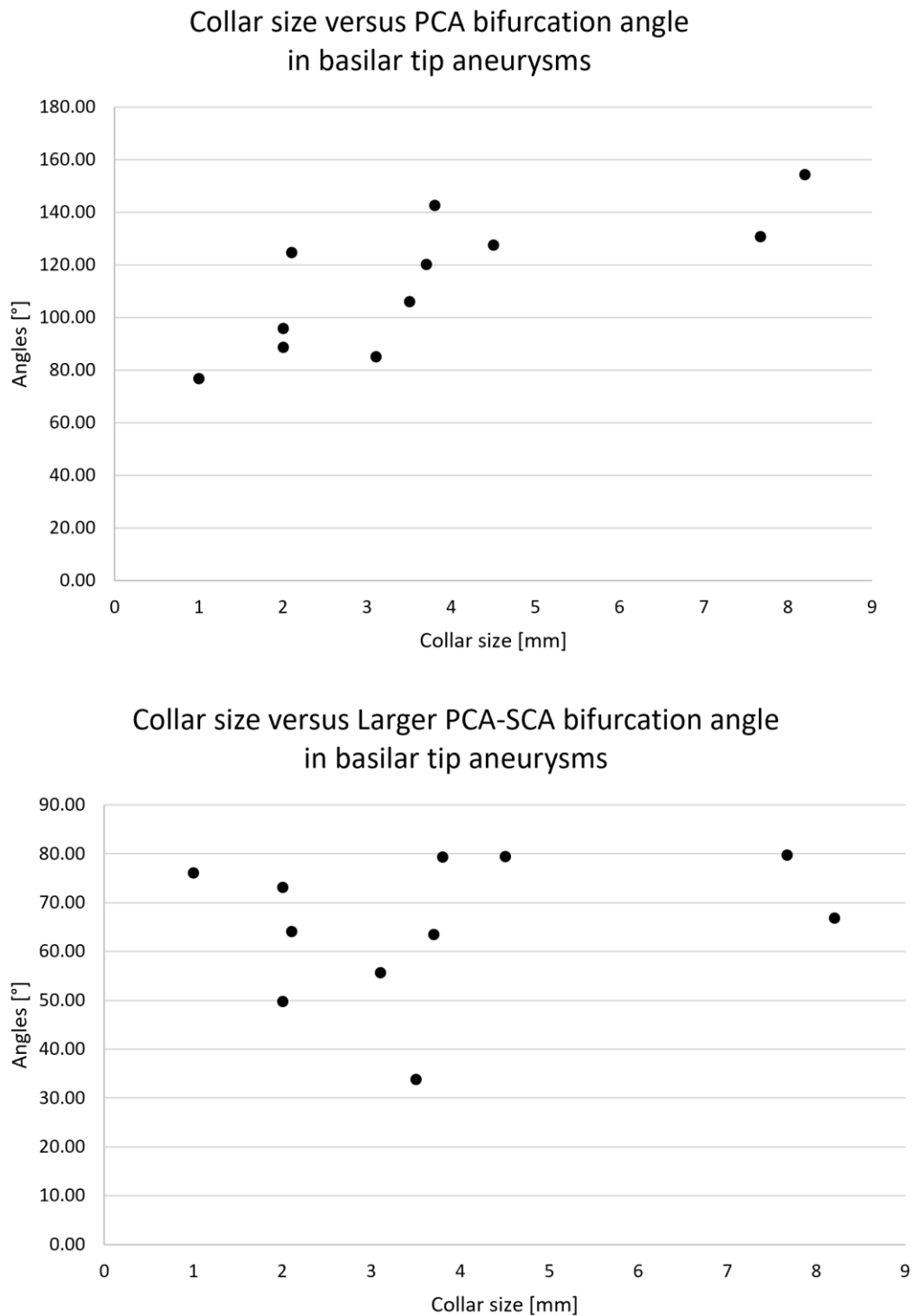
Figure 3-18 Collar size and angles in basilar-tip aneurysm group

Maximum diameter versus PCA bifurcation angle in basilar tip aneurysms
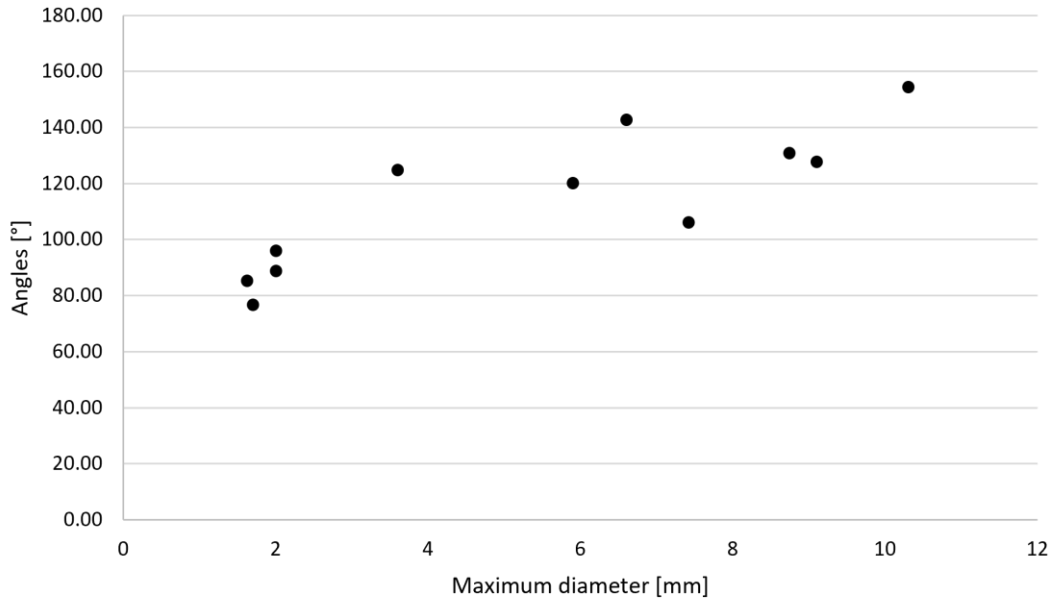
Maximum diameter versus Larger PCA-SCA bifurcation angle in basilar tip aneurysms
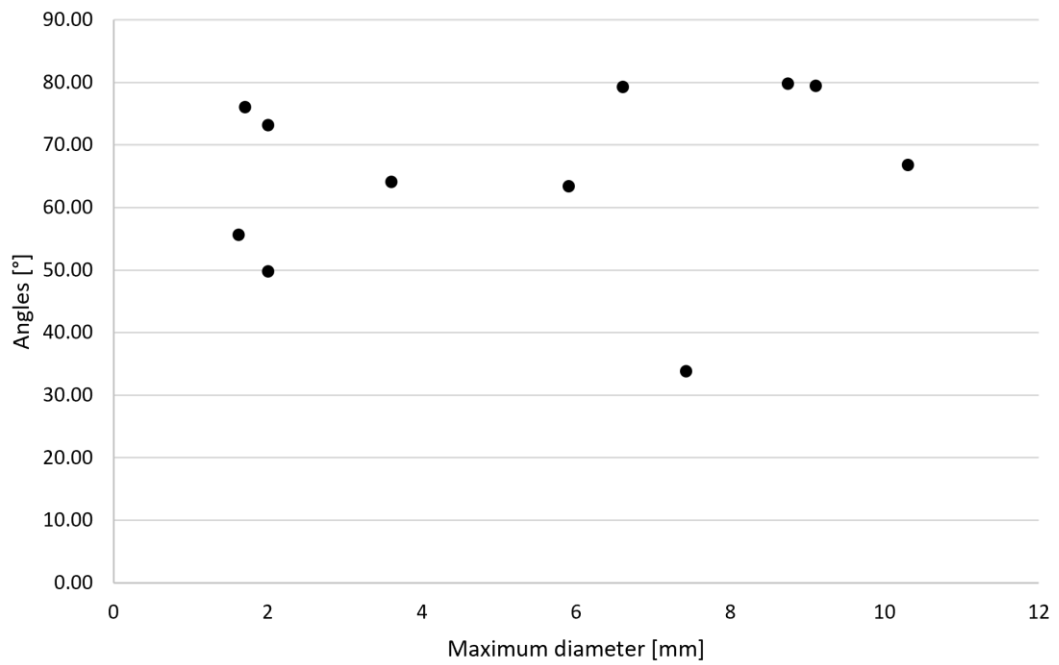
Figure 3-19 Maximum diameter and angles in basilar tip aneurysm grou

Chapter 4

The influence of blood velocity and vessel geometric parameters on WSS

Chapter 4   The influence of blood velocity and vessel geometric parameters on wall shear stress

4.1 Introduction

In this chapter, we did a study to quantify the influence degree of geometric and flow features on WSS in BA. WSS distributions from CFD results in 20 patients were statistically analyzed to identify the parameters significantly affecting WSS. Furthermore, we also quantified the influence degree of each parameter. The identification and quantification of influential parameters will provide important information for future statistical studies correlating WSS and shape parameters with the onset of IA.

4.2 Methods

The process of this chapter was listed in Fig.4-1.

4.2.1   Participants

This study retrospectively studied patients with a Doppler ultrasound test and MRA check of VA and BA. The time interval between the two tests was less than 1 week. The resolution of MR angiography tests was clear enough to make reconstruction VA and BA models. Patients included in this study were patients with primary aldosteronism who underwent medical examinations between 2009 and 2016. No plaques or wall thickening were detected in VA and BA, as diagnosed by experienced ultrasound technicians from Tohoku University Hospitals.

The cohort was consisted of 20 patients (11 women and 9 men) with ages ranging from 34 to 73 years (54 ± 11 years). All patient personal data used in this study was approved by the Ethics Committee of Tohoku University.

In the present study, three-dimensional time-of-flight MRA was performed with three different types of machines under routine clinical work. The majority of patients (14 out of 20) underwent MRA check using an Achieva 3T instrument (Philips Medical Systems). The parameters for this check were as follows: a slice thickness of 1.2 mm; the reconstructed voxel size was $0.2841 \times 0.2841 \times 0.5999$ mm^3; and the reconstruction diameter was 200 mm. The MRA test was performed with patients in a head-first supine position.

Four patients underwent MRA checks using a 3T Siemens MR header. The parameters were: a slice thickness of 0.65 mm; a reconstructed voxel size of $0.2865 \times 0.2865 \times 0.6500$ mm^3; and the flip angle for both machines was 20°.

The remaining 2 patients were tested using GENESIS_SIGNA from GE Medical Systems. The parameters were: a slice thickness of 1.2 mm; a reconstructed voxel size of $0.4102 \times 0.4102 \times 0.5439$ mm^3; a reconstruction diameter of 210 mm; and a flip angle of 18°. The phase encoding direction was in rows for all listed types of checks.

4.2.2 Model reconstruction

The reconstruction of 3D vascular models was conducted using the threshold function in Fiji [111], [112] and Blender 2.90 [100]. Smoothing was performed with Meshlab and Autodesk Netfabb Premium 2019 (©AUTODESK) to limit the variation in model volume to 5%. Side branches—including the PSCA, SCA, pontine arteries, and AICA—were removed during this process.

Detailed reconstruction process was explained in Fig.4-2 and 4-3. The smoothing process was explained in Fig.4-4 and 4-5. The examples of applying different smoothing methods were exhibited in Fig.4-5. It could be observed that the geometric changing after smoothing varied a lot among different smoothing algorithm. The details of volume changing after different smoothing algorithms were listed in Table 4-1.
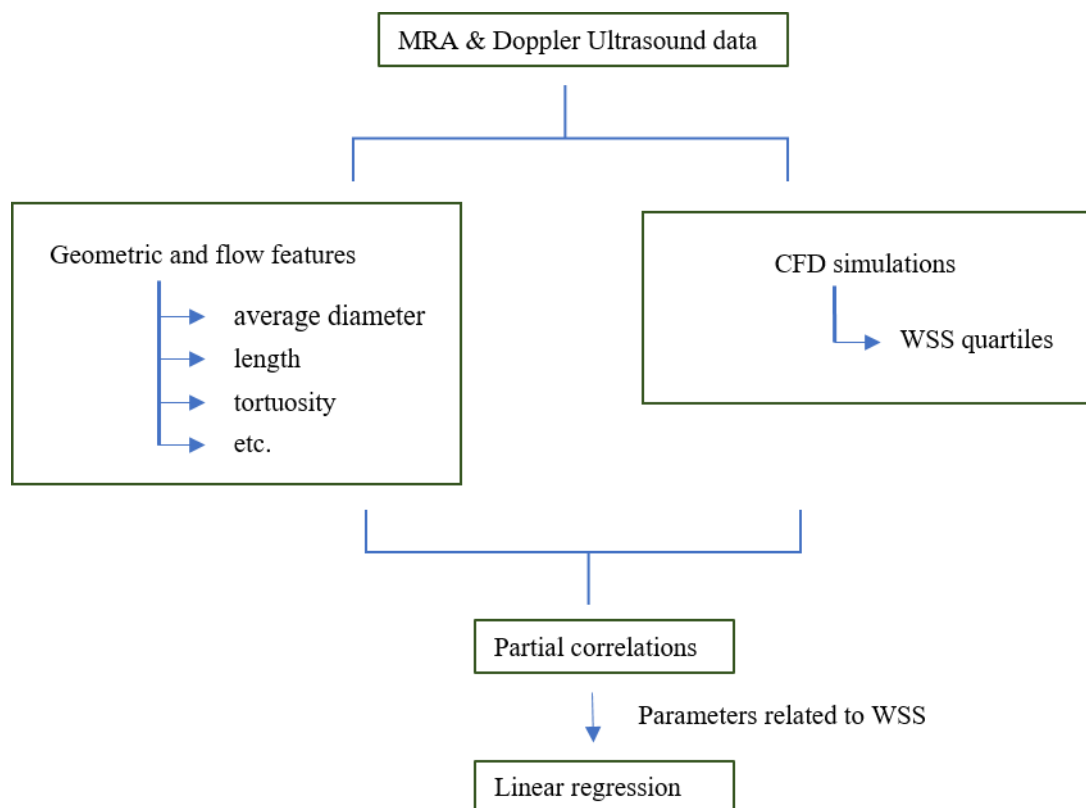
Figure 4-1 Process flowchart: the process of the methods applied in this chapter.
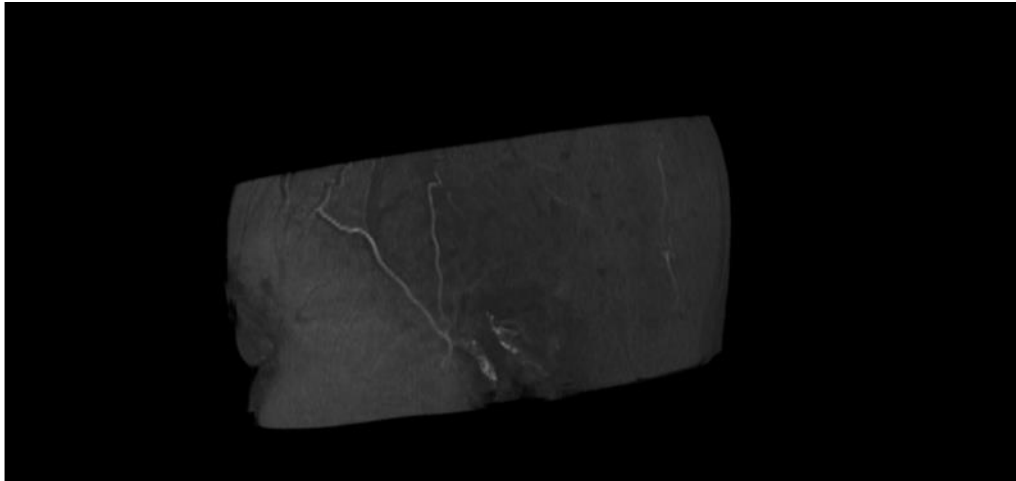
MRA image constructed in Image J Fiji
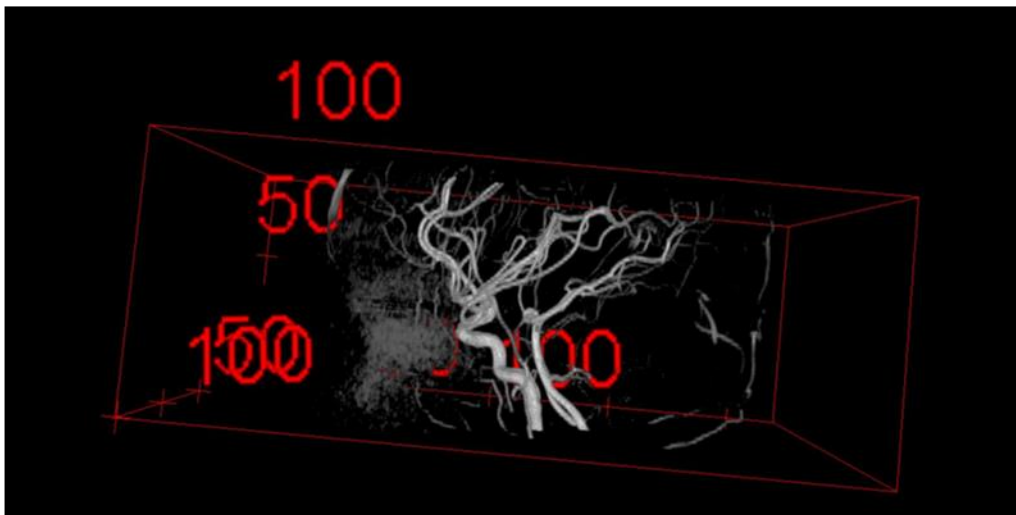
The vessel model after adjusting threshold (Threshold= 88 in this case)

The model displayed as surface

Figure 4-2 The reconstruction process in Image J Fiji: the process of the first reconstruction step finished with Image J Fiji.
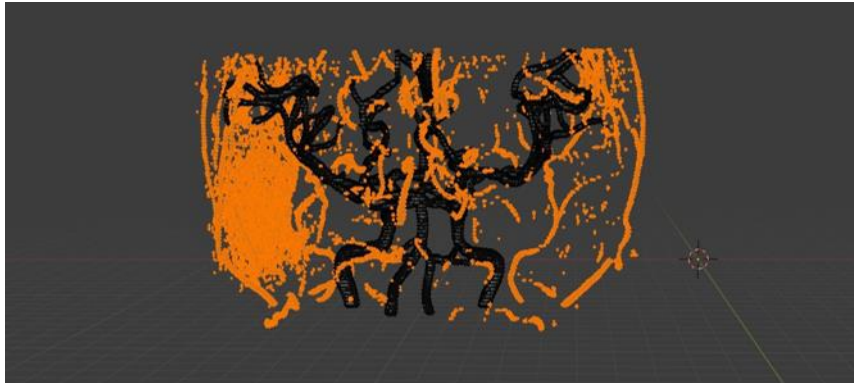
Remove the noise and un-connected parts

Remain only vertebral and basilar arteries

Remove all side branches on vertebral and basilar arteries

Figure 4-3 The reconstruction process in Blender 2.9: the process of the removing subjects other than vertebral and basilar arteries in Blender 2.9.
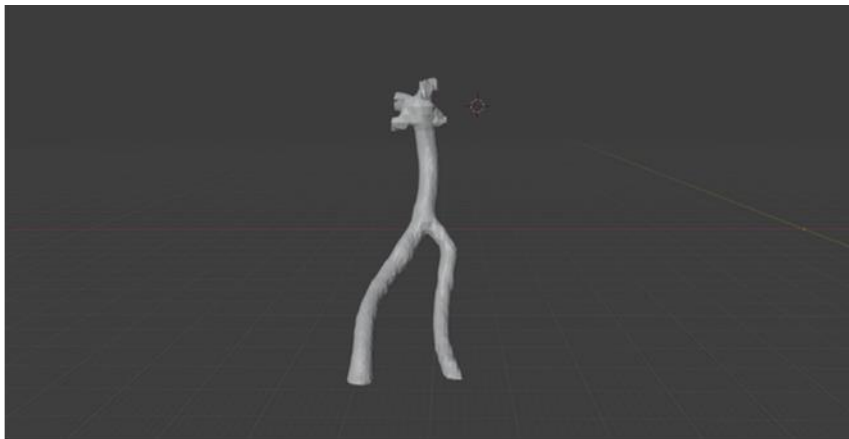
Remained vertebral and basilar arteries after mild manual smoothing
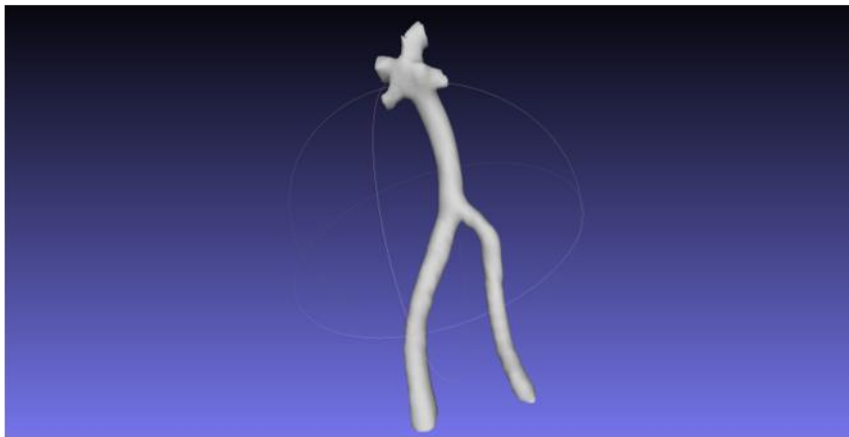
Smoothed with Taubin Smooth function in Meshlab
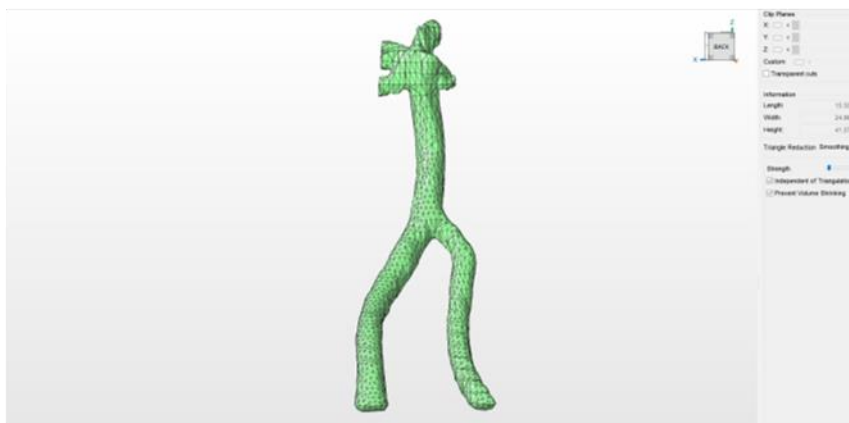
Read the model in Netfabb Premium (©Autodesk)

Figure 4-4 The smoothing process: the process of the smoothing. The whole smooth process could be divided into three steps:(1) Manual mild smoothing in Blender; (2) Taubin smooth in Meshlab; (3) Smoothing in Netfabb Premium.
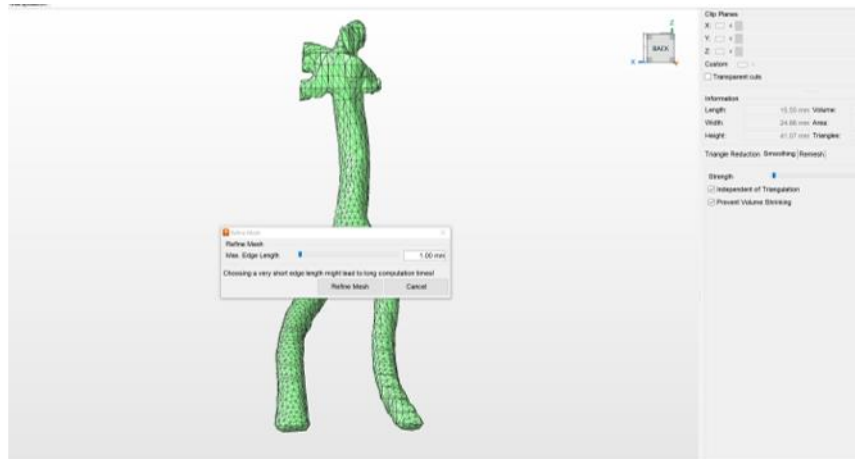
Refine the mesh and smooth
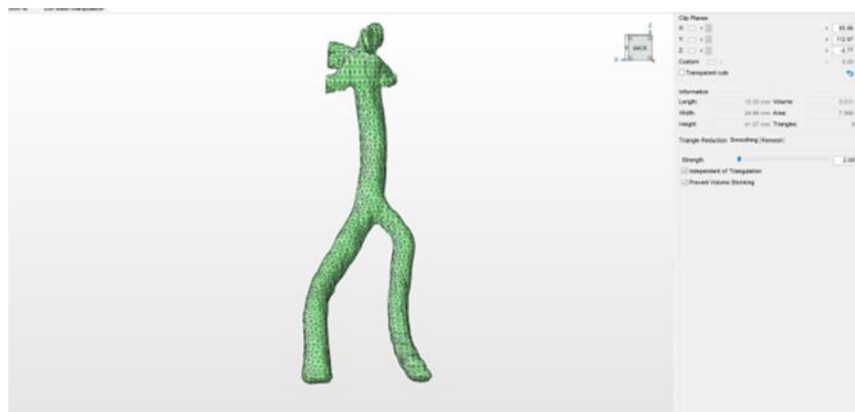
Before the smoothing

After the smoothing

Figure 4-5 The smoothing process: the last process of the smoothing: smooth the model surface in Netfabb Premium. The changing ratio before and after the smoothing of the model volume was less than 1%.

Before the smoothing

After the smoothing

Taubin smooth

Twostep smooth

Depth smooth

Laplacian smooth

HC Laplacian smooth
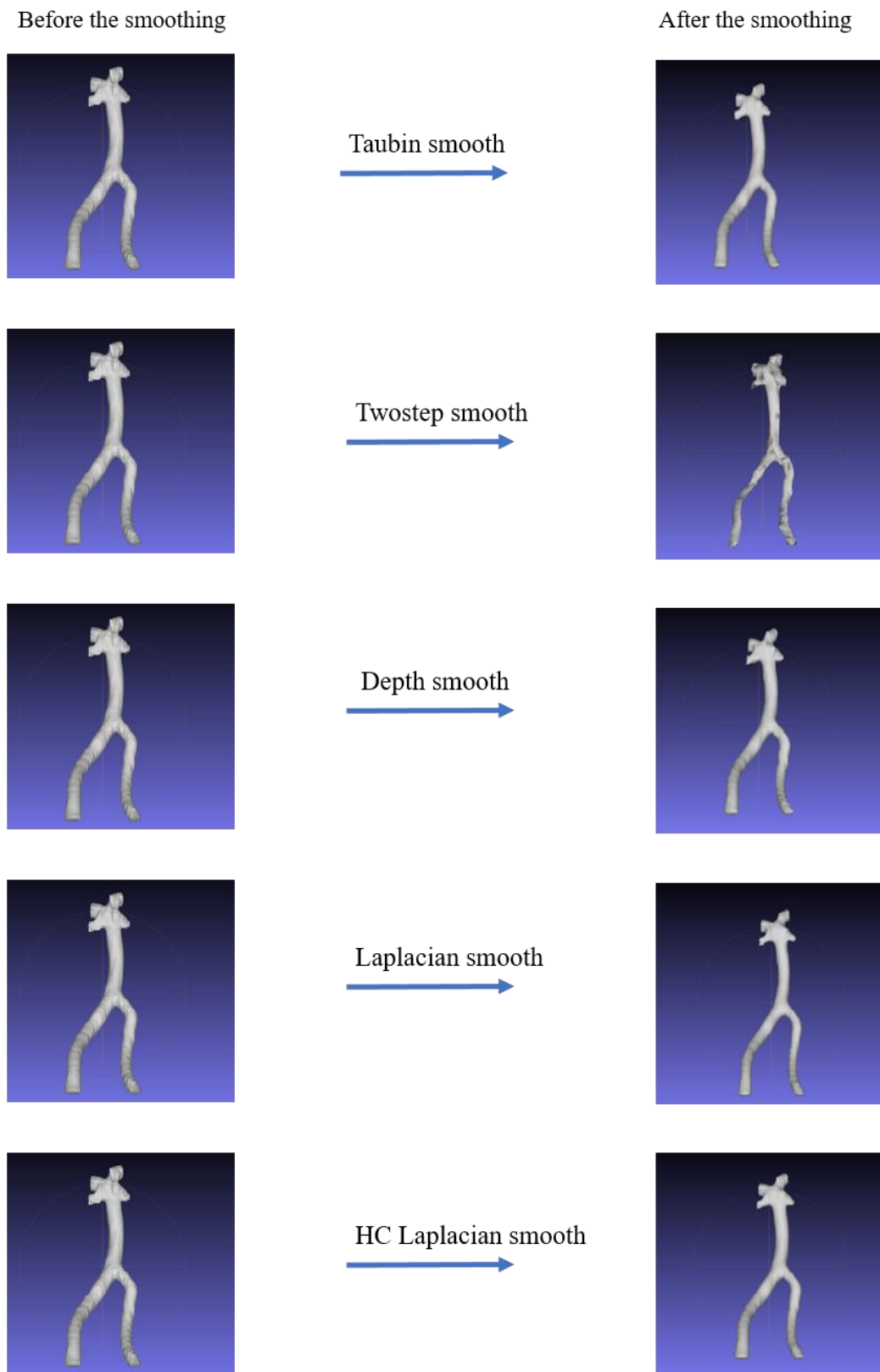
Figure 4-6 The error brought by different smoothing methods: the models before and after different smoothing methods via Meshlab.

Table 4-1 Volume changing ratio via different smoothing methods in Meshlab

Smoothing method	Previous Mesh volume	Mesh volume after smooth	Mesh volume changing ratio	Previous surface area	Surface area after smooth	Surface area changing ratio
Taubin smooth	511.28	514.70	0.67%	758.80	751.12	-1.01%
Twostep smooth	511.28	220.34	-56.90%	758.80	603.19	-20.51%
Depth smooth	511.28	466.31	-8.80%	758.80	722.50	-4.78%
Laplacian smooth	511.28	414.50	-18.93%	758.80	666.62	-12.15%
HC Laplacian smooth	511.28	465.30	-8.99%	758.80	708.14	-6.68%

From the above table, we could tell the reason of choosing the combination of taubin smooth and Netfabb Premium. It is the combination that enables us with models having the smoothest surface together with smallest volume change.

The entrances of the two VAs were extended to ensure that the flow could fully develop, and the details were exhibited in Fig.4-7. The calculation of entrance length was based on the following equation:

$$\text{Entrance length} = 0.05 \cdot Re \cdot D \tag{4-1}$$

where Re represents Reynold's number and D represents vessel diameter. Since the Reynold's number can be calculated as:

$$Re = \frac{\rho \cdot u \cdot D}{\mu} \tag{4-2}$$

where ρ represents density, u represents flow speed, and μ refers to dynamic viscosity. The density applied in this study was 1050 kg/m^3 and the dynamic viscosity was 0.0035 Pa · s.
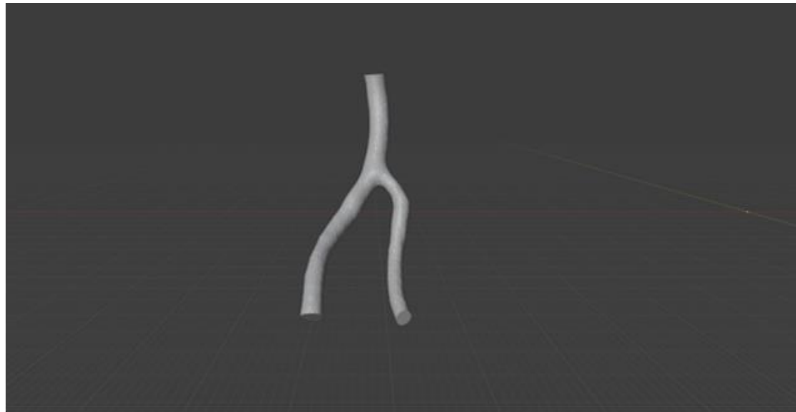
After segmentation
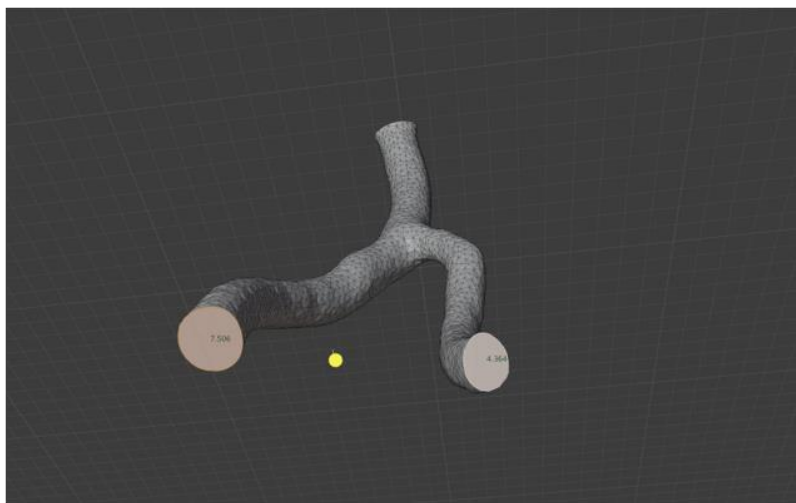
Measurement of inlets, preparing the entrance length
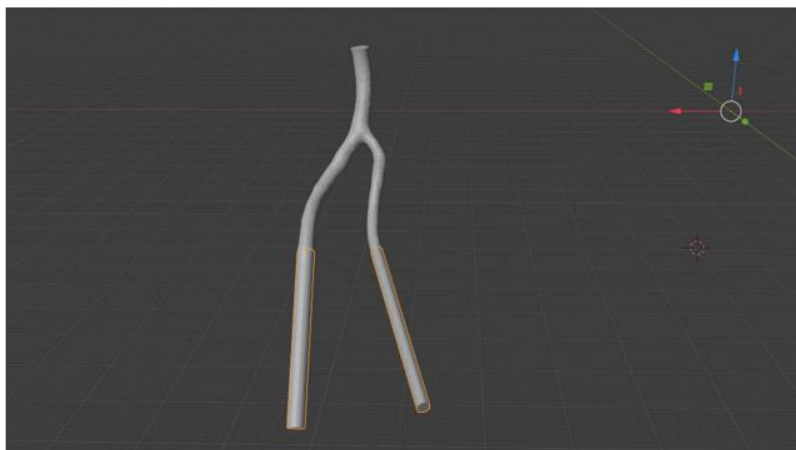
Entrance length constructed

Figure 4-7 The pre-processing for CFD simulations: the pre-processing of the models to apply them into CFD simulations. This whole process includes the segments of inlets and outlets and elongate the inlets for fluid development.

Based on information above, the entrance length can be obtained by the following equation:

$$Entrance\ length = \frac{0.05 \cdot \rho}{\mu} \cdot u \cdot D^2 \tag{4-3}$$

4.2.3 Geometric parameters

(1) Splitting models

The geometric parameters studied in this chapter are listed in Fig.4.8. The geometric features of each reconstructed BA and VAs were identified with the centerline of the whole model. The details of centerline extraction have been introduced in chapter 3.2.3. Similar to what we did in chapter 3, the bifurcation point was identified with VMTK. The area and velocity at the BA-VA bifurcation plane were defined as BA proximal area and BA proximal velocity in this thesis work.

(2) Curvature and tortuosity

To describe the variation of BA shape, curvature and tortuosity were employed. The curvature of the BA was calculated by finding the most fitted sphere to the BA centerline. The most fitted sphere here means the one can minimize the distance between centerline points and the sphere's surface. The distance was measured with the least squares method. Assuming that the radius of the sphere is "R," the curvature of the BA (represented by k) was defined as:

$$k = {1}/{R} \tag{4-4}$$

The tortuosity of the BA (represented by τ) was defined as the ratio between the actual BA length and the straight-line distance between VA-BA bifurcation and BA-SCA bifurcation and calculated as:

$$\tau = {L}/{D} \tag{4-5}$$

in which "D" is the straight-line distance and "L" being the actual length.

(3). Diameter and velocity

The average BA diameter was determined based on the diameter of the 3D model. We summed the diameter of each inscribed sphere alongside the BA centerline and the average number of this series of diameters was referred to as the BA average diameter. Correlations between diameter/velocity and WSS quantiles were analyzed separately in this study to obtain the degree of influence of each geometrical and velocity parameter on WSS.
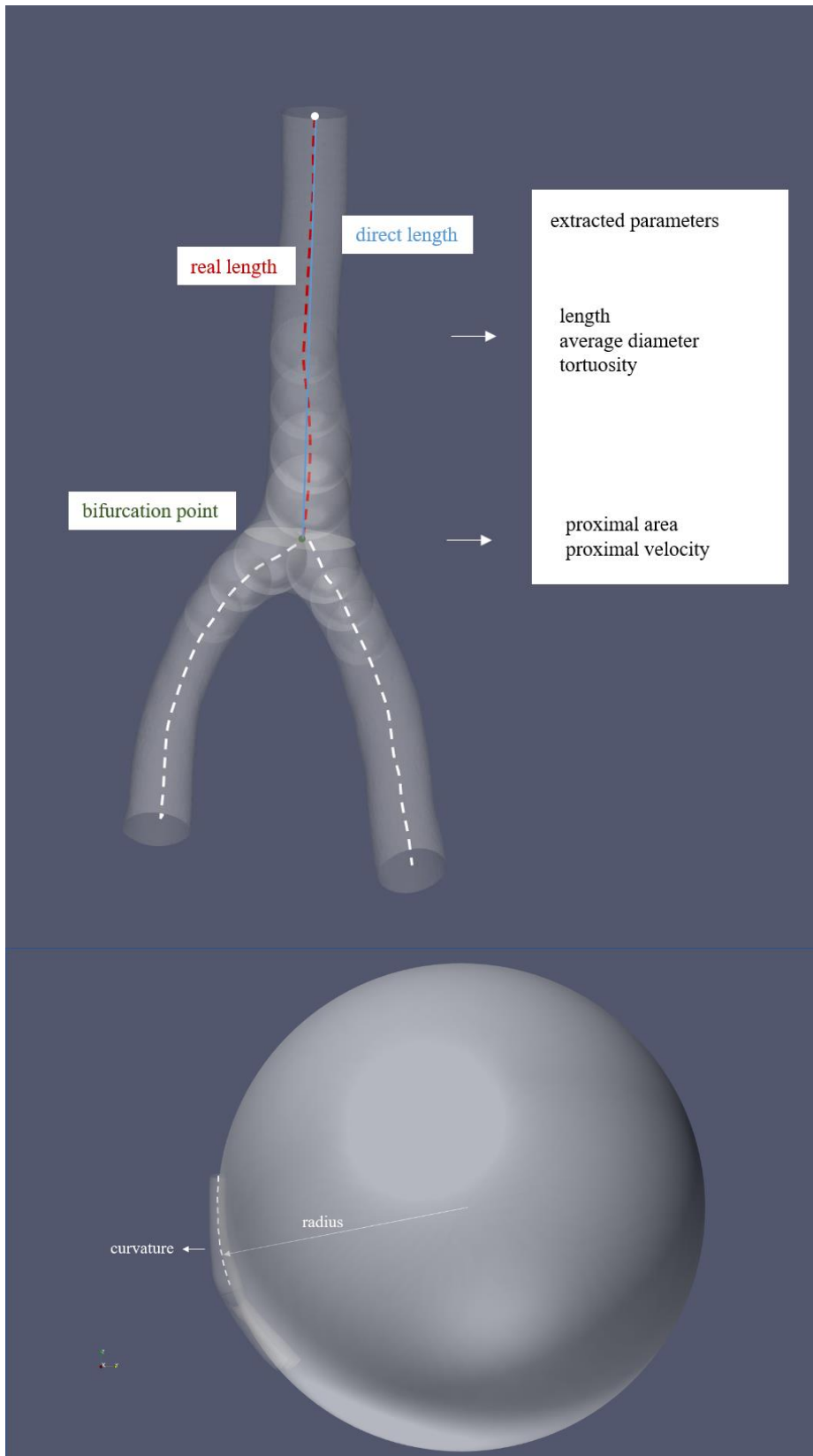
Figure 4-8 Geometric parameters: the geometric features utilized in this chapter. The sphere inside the bottom figure is the most fitted sphere to the BA centerline calculated with least square method.

4.2.4　Computational simulations

(1) CFD settings

The details of CFD settings applied in this chapter were explained as follows:

- Steady simulations with Star CCM+ 13.04.010 (© Siemens PLM, U.S.A).
- The polyhedral mesh with prism layers, the base size was 0.1 mm based on independence tests.
- Hypothesis of rigid and no-slip wall, laminar flow, and Newtonian flow were applied. The outlet in the BA was supposed to be a pressure outlet with 0 Pa.

(2) Boundary conditions

The applied boundary conditions were BA flow rates, which were defined as the sum of the VA flow rates. With the average blood velocity and VA diameters determined by Doppler ultrasound test, the VA flow rates were calculated. The ultrasound tests were performed as routine checks by experienced technicians. The machine included in these tests was a Toshiba Aplio instrument and V6.00 version software. VA was most frequently examined in the C4–C5 intertransverse segment with patients in the supine position. The patient's head was tilted upward and turned to the contralateral side at approximately 10° from the midline position.

(3). Post-processing

To comprehensively observe the whole WSS distributions, WSS quantiles were utilized in our simulations. The WSS on each cell was extracted and listed regarding to the WSS magnitude. Then the quantiles were calculated in each case. Quantiles considered in this chapter included the 97.5th, 90th, 75th, 50th, 25th, 10th, and 2.5th percentiles, as well as the interquantile range (IQR) between the 75th and 25th percentiles. This whole process was carried out using JMP®, Pro 16 (SAS Institute Inc., USA). The reason why 97.5^{th} and 2.5^{th} were utilized instead of directly using maximum and minimum WSS is because WSS is a parameter highly sensitive to the vessel wall geometry. Although we did our best to make the wall situation of our models smooth enough, the direct maximum and minimum can still be decided by very random bias brought by geometry variations.

4.2.5　Data analysis

As we listed in Fig.4-1, the analysis process used here can be divided into two steps. At first, partial correlation was tested between each WSS quantile and each BA geometric and flow features. This step was applied to decrease the potential influencing parameter number.

Following the results of partial correlation tests, only parameters with significant correlations to the WSS percentiles will be subjected to multiple linear regression.

In addition, the partial correlations were also tested among the BA and VA geometric features. A *t*-test was applied to study the VA lateral differences. These analyses were performed using JMP Pro 16 and IBM SPSS Statistics (IBM Corp. Released 2020. IBM SPSS Statistics for Windows, Version 27.0. Armonk, NY: IBM Corp). Both software were used so that we could validate the results from different data analysis software. To escape the family-wise error rate because multiple analyses were performed within the same database, Bonferroni correction was employed during the partial correction test process.

4.3 Results

Table 4-2 Geometric features

Case Number	Left VA		Right VA		BA					
	D[mm]	V_{mean} [m/s]	D [mm]	V_{mean} [m/s]	L [mm]	k[m^{-1}]	τ	$A_{proximal}$ [mm^2]	$V_{proximal}$ [m/s]	D_{mean} [mm]
1	3.8	0.120	2.5	0.112	15.85	0.039	1.017	13.5	0.141	3.28
2	3.0	0.086	3.9	0.058	22.97	0.056	1.090	18.3	0.071	3.88
3	3.2	0.125	3.1	0.120	22.94	0.024	1.033	15.6	0.122	3.52
4	3.8	0.104	3.3	0.082	25.09	0.058	1.340	16.9	0.111	3.8
5	3.0	0.088	3.6	0.080	20.21	0.078	1.170	13.5	0.106	3.5
6	3.3	0.222	2.6	0.138	21.27	0.014	1.013	13.2	0.199	3.56
7	3.5	0.076	3.4	0.096	27.57	0.018	1.021	17.0	0.094	4.06
8	4.3	0.131	2.2	0.111	27.64	0.046	1.106	22.4	0.103	4.22
9	2.8	0.083	2.9	0.104	25.05	0.047	1.078	13.2	0.090	3.04
10	4.4	0.118	3.6	0.079	27.21	0.021	1.032	20.5	0.126	4.04
11	4.5	0.102	3.6	0.076	26.88	0.013	1.019	18.9	0.126	3.82
12	2.6	0.074	2.9	0.117	29.44	0.018	1.069	15.6	0.074	3.24
13	2.9	0.121	3.5	0.124	24.23	0.031	1.027	12.5	0.159	3.18
14	3.0	0.104	2.8	0.095	25.11	0.038	1.065	10.1	0.131	3.42
15	3.4	0.109	2.9	0.090	19.84	0.035	1.037	13.6	0.116	3.42
16	3.5	0.091	3.3	0.094	25.54	0.046	1.077	14.5	0.115	3.5
17	2.6	0.146	2.9	0.106	23.98	0.006	1.009	13.2	0.111	3.36
18	4.0	0.106	4.3	0.104	19.14	0.016	1.011	20.7	0.137	3.64
19	2.6	0.119	2.6	0.091	20.28	0.015	1.026	9.0	0.124	2.82
20	4.6	0.164	3.2	0.137	22.55	0.029	1.041	20.8	0.184	4.3
Mean ± SD	3.4 ± 0.7	0.114 ± 0.033	3.1 ± 0.6	0.100 ± 0.021	23.64 ± 3.44	0.032 ± 0.019	1.064 ± 0.076	15.7 ± 3.70	0.120 ± 0.033	3.58 ± 0.38

4.3.1 Morphological and flow parameters

The morphological features of the 20 patients are listed in Table 4-2 [113]. In the table, "D" represents diameter, "V_{mean}" refers to average velocity, "k" means curvature and "τ" means the tortuosity. "$A_{proximal}$" and "$V_{proximal}$" represent proximal area and proximal velocity separately, referring to the area and velocity at VA-BA conjunction.

According to the table, we would like to emphasize several data inside. The average BA diameter of 20 patients was 3.58 ± 0.38 mm. The mean diameter of the left LVA and right VA was 3.4 mm and 3.1 mm, respectively.

Since the velocity and diameter of the VAs exhibited a normal distribution, VA parameters were able to be used in the Student's t-tests. The velocity in left VA was significantly ($P < 0.05$) larger than that in the right side according to paired t-tests results, as previously reported by Schöning and Hartig [114], [115]. Conversely, the results between left and right diameters showed no significant lateral difference, unlike Simon's report [116]; however, similar observation was reported by Peter Scheel [117].

4.3.2 Data analysis

(1) Correlation test

The partial correlation results between morphological characteristics and WSS quantiles were summarized in Table 4-3 [113]. Based on the adjusted significance level presented in the table, it was observed that, under almost all circumstances, there was a correlation between proximal velocity and average diameter with WSS. Proximal area exhibited correlation in most of the situations except for relatively low WSS (below the 10th WSS quantile. Tortuosity demonstrated correlation with WSS only under extremely high WSS area (97.5th WSS quantile). Although curvature did not exhibit a significant correlation with the 97.5[th] WSS, the p-value in this case was very close to the corrected confidence interval.

After completing correlation tests between BA and WSS, similar tests were performed on VA and BA characteristics (Table 4-4) [113]. Among the three main factors (BA average diameter, proximal area, and proximal velocity), only proximal velocity showed a lot of correlations with VA parameters (velocity in both VAs and diameter in the left VA). The proximal area correlated with the diameter in the left VA diameter only, and BA average diameter did not show correlations with VA parameters.

In the lateral study of VAs, it was revealed that VA velocities and flow rates exhibited significant lateral differences based on the t-test results. The left VA had larger velocities and flow rates, while no significant differences were detected for VA diameters.

Table 4-3 Partial correlation probability among WSS and BA characteristics

	WSS$_{97.5\%}$	WSS$_{90.0\%}$	WSS$_{75.0\%}$	WSS$_{50.0\%}$	WSS$_{25.0\%}$	WSS$_{10.0\%}$	WSS$_{2.5\%}$	WSS$_{75\%-25\%}$
k[m^{-1}]	0.0066	0.7213	0.9723	0.8443	0.4353	0.5806	0.6212	0.2288
τ	0.0007	0.0204	0.1168	0.4970	0.8149	0.7030	0.4746	0.0127
L[mm]	0.5968	0.8061	0.3802	0.4729	0.6352	0.1633	0.0390	0.5933
$A_{proximal}$ [mm^2]	<0.0001	<0.0001	<0.0001	<0.0001	<0.0001	0.0116	0.2523	<0.0001
$V_{proximal}$ [m/s]	<0.0001	<0.0001	<0.0001	<0.0001	<0.0001	<0.0001	0.0001	<0.0001
D[mm]	<0.0001	<0.0001	<0.0001	<0.0001	<0.0001	0.0007	0.0013	<0.0001

*Bonferroni correction, n = 8, significant level α = 0.00625

Table 4-4 Partial correlation probability among BA and VA morphology and flow velocity

	$V_{proximal}$ [m/s]	τ	$A_{proximal}$ [mm^2]	k[m^{-1}]	L [mm]	BA D_{mean}[mm]
RVA-diameter[mm]	0.5720	0.9593	0.0696	0.8247	0.4700	0.6337
RVA-velocity[cm/s]	<0.0001	0.4483	0.1773	0.8644	0.0605	0.0473
LVA diameter[mm]	0.0009	0.7351	0.0002	0.8247	0.5242	0.1836
LVA velocity[cm/s]	<0.0001	0.2749	0.3262	0.0485	0.3387	0.1771

*Bonferroni correction, n = 6, significant level α = 0.008

(2) Linear regression

The outcomes of the linear regression analysis are presented in Table 4-5 [113]. After assessing the variance inflation factor (VIF) and linear correlation between each characteristic, stepwise regression was employed in this chapter. The multicollinearity among all potential parameters were examined using VIF. A strong correlation was found between proximal area and BA diameter, while the remaining parameters appeared independent of each other.

Multivariate regression was conducted twice for each WSS quantile to ensure that BA and proximal area were not input into the same regression calculation. In the regression calculations for all WSS quantiles, except the 97.5[th] quantile WSS, only two parameters were entered into a single regression—either proximal area and proximal velocity or average diameter and proximal velocity. Considering the correlation results, tortuosity was input into the regression model for the 97.5[th] quantile WSS and BA characteristics. The regression models for the

10th and 2.5th WSS quantiles only included BA diameter and proximal velocity due to the lack of significant correlations with proximal area and these two WSS quantiles.

To summary all analysis results, the proximal velocity remained a highly influential factor across all WSS quantiles. From the 97.5th to 25th WSS quantiles, the proximal velocity was the only influential factor. In the 10th WSS quantile, the average diameter exhibited a negative influence. While for the 2.5th quantile, the influence of average diameter increased, slightly larger than that of the proximal velocity. Within the IQR, proximal area positively influences WSS, whereas average diameter had no effect.

4.3.3   WSS quantiles in individual patients

The WSS quantiles were derived from the simulation results of the 20 cases. The detailed WSS results were exhibited in Table 4-6. For better observation, the WSS results were also exhibited via boxplots (Fig.4-9). The 97.5th, 90th, 75th, 50th, 25th, 10th, and 2.5th percentiles were chosen to represent inside the quantile box plot. The box plot reveals that, even when having similar average WSS values, the cases displayed varied WSS ranges. The simulation results are listed in Fig.4-10.

Table 4-5 Regression results of BA characteristics and WSS

Entered variables	$A_{proximal}$, $V_{proximal}$ (τ in 97.5th) *		Unstandardized β	Standard coefficients β	BA D_{mean}, $V_{proximal}$ (τ in 97.5th) *		Unstandardized β	Standard coefficients β
	Adjusted R^2	Significant factor			Adjusted R^2	Significant factor		
97.5	0.591	Proximal velocity	27.874	0.783	0.591	Proximal velocity	27.874	0.783
90	0.705	Proximal velocity	24.648	0.849	0.705	Proximal velocity	24.648	0.849
75	0.678	Proximal velocity	20.510	0.833	0.678	Proximal velocity	20.510	0.833
50	0.659	Proximal velocity	16.419	0.823	0.659	Proximal velocity	16.419	0.823
25	0.609	Proximal velocity	11.824	0.793	0.609	Proximal velocity	11.824	0.793
10	-	-	-	-	0.605	Proximal velocity	9.536	0.761
							−0.346	−0.338
						BA diameter		
2.5	–	–	-	-	0.573	BA diameter	−0.486	−0.585
							5.916	0.581
						Proximal velocity		
IQR	0.643	Proximal velocity	8.887	0.759	0.525	Proximal velocity	8.686	0.742
			0.037	0.361				
		Proximal area						

Table 4-6 WSS quantiles [Pa]

Case Number	97.5%	90.0%	75.0%	50.0%	25.0%	10.0%	2.5%
1	3.999	3.427	3.004	2.481	2.107	1.876	1.530
2	1.551	1.291	1.109	0.959	0.795	0.630	0.442
3	3.345	2.934	2.616	1.939	1.467	1.123	0.889
4	3.684	2.613	2.128	1.649	1.194	0.867	0.568
5	2.690	2.226	1.782	1.451	1.187	0.942	0.645
6	5.569	4.360	3.514	2.716	1.973	1.567	1.109
7	1.503	1.282	1.132	0.961	0.755	0.604	0.480
8	3.234	2.631	2.127	1.539	1.075	0.838	0.615
9	2.510	2.196	1.921	1.558	1.222	0.943	0.758
10	3.105	2.617	2.266	1.798	1.176	0.626	0.272
11	3.281	2.849	2.440	2.012	1.586	1.136	0.626
12	2.871	2.062	1.692	1.437	1.194	0.949	0.576
13	4.899	4.219	3.517	2.937	2.322	1.737	1.381
14	2.047	1.725	1.445	1.218	0.974	0.700	0.444
15	2.257	1.929	1.643	1.322	1.051	0.905	0.771
16	2.990	2.576	2.209	1.838	1.349	1.020	0.792
17	4.647	2.519	1.922	1.560	1.215	1.018	0.828
18	6.54	4.999	4.563	4.045	3.540	2.868	1.823
19	2.268	1.978	1.679	1.348	1.054	0.865	0.748
20	4.925	4.218	3.572	2.987	2.301	1.847	0.892
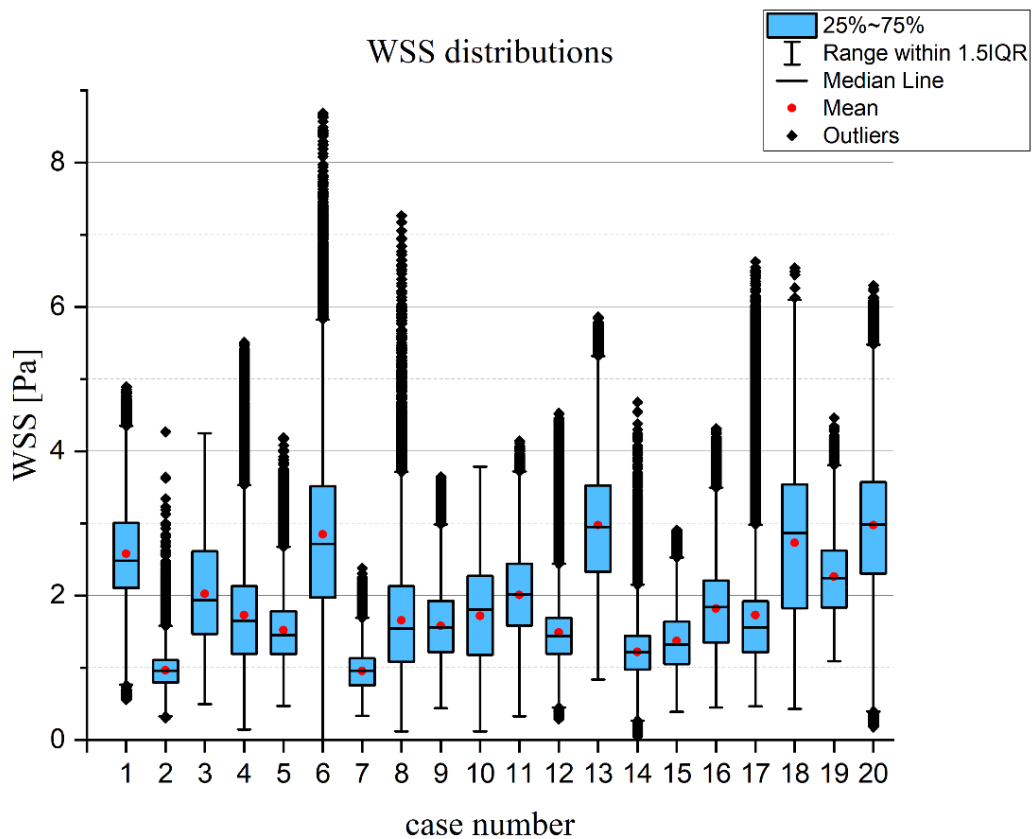
Figure 4-9 WSS distributions: the WSS distribution of all 20 cases in boxplots. The red points inside the boxes are the mean value and the black line in the middle of boxes means the median value.

4.4 Discussion

This chapter examined the different influence degree of vessel shape and flow velocity on WSS. Our findings revealed that various vessel geometric and flow variables influenced WSS to varying degrees. We specifically input the proximal area and velocity into our analysis due to the unique geometry of the human vertebrobasilar system, where two arteries converge into one. Prior studies have emphasized the importance of proximal area, tortuosity, as well as the vessel diameter in WSS prediction [29], [31]. Consequently, we included the vessel length and curvature detected via 3D models to characterize various vascular shape characteristics.

4.4.1 Statistical analysis quantifying the degree of BA WSS quantiles

The outcomes of the multiple regression analysis revealed the importance of BA proximal velocity, as it emerged as the only parameter exhibiting a robust impact on each WSS quantile. Given that WSS is calculated using the velocity gradient near the wall, a positive

correlation between proximal velocity and all WSS quantiles is expected. Notably, other parameters also demonstrated moderate or strong correlations with specific WSS quantiles.

The results also called attention to the BA average diameter, which affects regions with relatively low WSS. As shown in Table 4-5, in general, the lower the WSS, the stronger the impact of the BA average diameter on BA WSS. The proximal area displayed a mild positive correlation with WSS IQR, while tortuosity correlated with the 97.5th quantile WSS.

The findings in Table 4-5 revealed that the adjusted R^2 of the regression models decreased in the lower WSS quantiles. The adjusted R^2 reached its peak value at the 90th WSS quantile and diminished with decreasing WSS. The adjusted R2 reached its lowest points at both the 97.5th and 2.5th WSS quantiles, indicating that factors influencing extremely high or low WSS may be more complicated than those influencing other WSS quantiles. From the 90th to 97.5th WSS quantile, the decrease in adjusted R^2 was nearly the same as the decrease from the 90th to the 2.5th WSS quantile, suggesting a higher decreasing ratio of adjusted R^2 in the high WSS region. This implies that potential influential factors exist, strongly affecting the high WSS region but not showing the same degree of influence on the low WSS region.

Before conducting multilinear regression, we verified the independence among all parameters input into in the regression model. In our case, proximal velocity and average diameter were found to be independent of each other, allowing them to be added into the multiple linear regression models.

Despite the constraints of our study sample size, we maintained the quality of our statistical results by dividing the statistical process into two steps. Involving correlation analysis before regression analysis helped reduce the variables in the regression models. While the reduction in statistical power suggests the potential existence of significant undiscovered results, the identified significance is robust and reliable. With an increased sample size, we could expect a more comprehensive understanding of the influence of various geometric features on WSS.

4.4.2 WSS distribution

Our simulation results showed that the WSS at the inner arc is lower than the WSS at the outer arc in all cases and the samples were exhibited in supplement material. This result is consistent with that of several previous studies that performed simulations in BA systems [78], [118], [119]. It has been reported that BA plaques are more likely to occur at the inner arc than at the outer arc [78]. This finding is consistent with the contention that regions exposed to a low WSS (LWSS) are more likely to develop plaques [74], [120].

Our simulation results indicated that in most of our cases, the WSS at the inner arc tended to be lower than that at the outer arc. This outcome aligns with previous studies that conducted simulations in BA and VA systems [78], [118], [119]. Previous research suggested that a higher WSS can be a trigger of aneurysm formation [22], [64] and this also called our attention on further study on WSS difference between inner and outer arc in the future.

Moreover, our observations revealed that, within the same patient, WSS varied more significantly alongside the BA rather than rather than varying strictly to the vessel curve. Our numerical analysis demonstrated a correlation between BA average diameter and low WSS quantiles, making the BA average diameter a potential predictor for the presence of low WSS. However, it could not accurately predict the specific positions of low WSS regions. Visualization results from our simulations suggested that the WSS distribution along the BA showed frequent changes based on inner-individual diameter variations. Therefore, a more detailed examination of diameter variation within the same subject will be required.

4.4.3 Vertebrobasilar artery geometry and flow velocity

The left VA demonstrated correlations with both BA proximal velocity and area, while the right VA only exhibited correlations with BA proximal velocity, as shown in Table 4-4. Our *t*-test results indicated significant differences in velocities and flow rates between the left and right VAs. The left VA showed larger velocities and flow rates than those of the right VA. This lateral difference might contribute to the varied correlations observed in the LVA and BA compared to the right side.

The calculated VA flow rate from our data appeared to be smaller than previously reported [121]. Several factors may explain this difference. One is the age of our sample [114], [117]. In our study, VA average velocities and diameters were derived from patients aged 34–73 years (average age $= 54 \pm 11$ years), whereas previously reported data were from volunteers with an average age of 23.6 years [121]. A series of studies have indicated that blood flow rates in elderly individuals tend to be lower than those in younger generation [114], [117], [122].

Variations in BA geometries, including its formation and termination levels, diameters, and vertebral–basilar conjunction shapes, have been highlighted in prior studies [31], [34], [123]. Manara et al. [123] conducted an analysis of a control group on 108 patients with no history of head trauma or neurological conditions, and they reported a mean BA diameter similar to our study (3.70 ± 0.36 mm versus 3.58 ± 0.38 mm). Amanda et al. [31] classified vertebral–basilar system into three basic geometric configurations (Walking, Tuning Fork, and Lambda). Although our study had a limited sample size, all types of VA–BA morphology were

observed. Given the variability in vascular geometry, the models in our study represented some geometric features due to the constraints of our limited sample size. A larger sample size might reveal additional geometric features.

This study utilized CFD simulations, which offer comprehensive hemodynamic information but are sensitive to many factors, including geometric uncertainty [124], [125], boundary conditions [126], and different simulation software [127]. Geometry uncertainty can arise from imaging resolution and operator subjectivity [110], [125]. To minimize this uncertainty, all models in our study were reconstructed by the same operator following a standardized threshold criterion. The details of this threshold criterion are explained in chapter 3. Patient-specific blood flow velocity, detected with Doppler ultrasound tests, helped reduce the uncertainty related to reference paper generalized boundary conditions. We also did study on the difference brought by generalized and specific boundary conditions and will explain it in chapter 5. Additionally, convolutional dropout networks can be employed to assess the ratio of uncertainty resulting from variations in inner-individual blood velocity, as described by Maher [125]. Patient-specific models were employed in this study. Some researchers did the geometry-WSS study based on standardized geometries and change the geometric features manually [124], [128], [129], however, our specific models revealed that the vessel geometry reflecting the real situation can be way more complicated than those manually created ones.

In our study, CFD simulations assumed steady flow due to the lack of patient-specific pulse wave data. Previous research has reported no significant difference between time-averaged WSS results obtained from time-dependent simulations and those derived from steady flow [130], [131]. However, the assumption of stationary flow limits the consideration of time-dependent variables like the OSI. We acknowledge the potential benefits of time-dependent simulations, and we would like to broaden our investigation scope when patient-specific waveforms become available in the future.

4.5 Limitations

Firstly, given the limited sample size, we conducted correlation tests first, and only parameters exhibiting significant correlations were input into the regression models. However, the relatively low adjusted R^2 values observed in low WSS quantiles suggested the need to add additional geometrical parameters. To achieve a more comprehensive understanding, a larger number of cases would be required for the regression analyses.

Secondly, CFD simulations were conducted under the assumption of a rigid wall and Newtonian flow. Comparison between Newtonian and non-Newtonian CFD simulations revealed negligible non-Newtonian effects with a Reynolds number range of 110 to 850 [132]. Considering that this study focused on BA and VA, the simulation was performed with the assumption of Newtonian flow. Steady flow was utilized to investigate the average BA WSS, BA geometry, and flow velocity. Future investigations will explore systolic and diastolic conditions.

Additionally, this study extended the entrance in VAs to ensure fully developed inlet flow in simulations. However, it is important to note the existence of tortuous in the VA proximal to our clip position. Because of the limitations in the clinical protocol, the region of MR images did not include this tortuous area in VA. In this study, only WSS in the BA was examined. While the impact of VA tortuous on the BA is considered moderate, further research on the influence of velocity profiles will be necessary. Another limitation we would like mention is about the posterior communicating artery (PcomA). The branches including PCA and PcomA were removed from our models and the potential impact brought by the flow from PcomA was not considered in this study.

4.6 Conclusion of this chapter

In conclusion, we studied the influence degree of BA morphology and velocity brought on WSS. The findings indicate that, among all assessed geometrical variables, the velocity at the vertebrobasilar bifurcation plane showed the most important effect on WSS distribution. BA average diameter exhibited a gradually negative effect in low WSS quantiles. This influence increased when WSS decreased. Notably, in 2.5^{th} WSS quantile, the influence brought by BA average diameter worked a bit larger than the proximal velocity.

The correlation between BA and VA characteristics was explored as well. The lateral differences in VA, as commonly reported in prior studies, were also reflected in the correlation. Only the left VA diameter showed a significant correlation with BA proximal area.

This study gave a quantified analysis report on the geometry-WSS correlations. Our results proposed the conjunctional velocity and local diameter variance as potential risk factors for IA formation. VA velocity, especially that in left VA, should also be paid attention to.
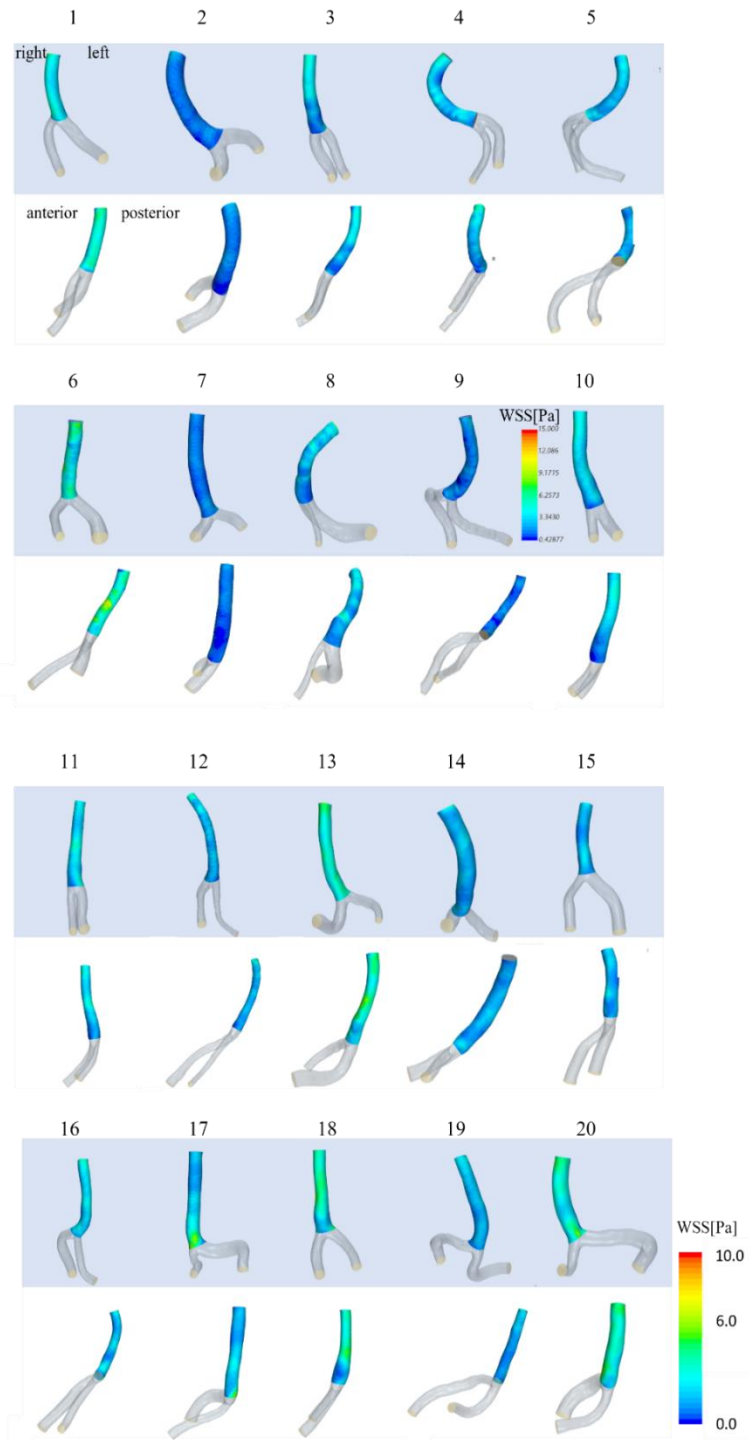
Figure 4-10 Simulation results: simulation results of all 20 cases. The color bar was different in case No.9 and the same for the remaining 19

Chapter 5

The influence brought by specific and generalized boundary conditions

Chapter 5　The influence brought by specific and generalized boundary conditions

5.1 Introduction

For many years, hemodynamics has been asserted as one of the primary factors influencing vascular diseases [133], [134]. Among all hemodynamic stress parameters, WSS has gathered the most attention as we mentioned in Chapter 1.1.3. Numerous studies reported its role in vessel plaque formation [74], [120] as well as aneurysm initiation, development, and rupture [135]–[137]. CFD technique has been widely employed in the past two decades to assess WSS as mentioned in Chapter 1.1.5 [138]. CFD can offer very detailed information about WSS. However, when applying CFD, boundary conditions have crucial impacts on the simulation results [130], [138], [139], which will consequently affect the conclusions on the WSS–disease relationship studies.

Due to the challenges associated with obtaining patient-specific measurements [126], [140], boundary conditions derived from reference papers are commonly used. In previous CFD studies, a common approach to implementing generalized boundary conditions includes extracting pulse wave and flow conditions from reference articles. Some researchers directly utilize the reference data into their simulations, while others adjusted the extracted data based on their own geometric parameters [141]–[143]. Several previous studies were conducted to report the differences in the CFD results when performed with generalized and specific boundary conditions [126], [140], [143], [144]. They emphasized that using patient-specific boundary conditions can be very important when exploring hemodynamic–disease relationships [144], [145]. Nevertheless, obtaining patient-specific data remains a challenge in most cases. Therefore, to improve the utilization of generalized data, we conducted a comparative analysis of various generalized flow rates against specific flow rates to establish the correlation between generalized and specific boundary conditions.

The study object in this study was the vertebrobasilar system, the only position where two arteries merge together into one [31]. Furthermore, variations in the VA are more commonplace than exceptional [114], [115]. We conducted a comparative analysis of the estimated VA flow rates using various generalization methods, which included direct extraction from previous studies, scaling previous reports with specific models, and applying a published area-flowrate relationship equation [146]. Additionally, certain approaches were employed in

computational simulations to assess the degree of consistency between generalized and specific simulation results in this vascular system characterized by high variations.

5.2 Methods

5.2.1 Patient selection

The cohort included in this chapter is the same as that included in chapter 4. For detailed information, please refer to chapter 4.2.1.

5.2.2 Model reconstruction

The reconstructed models applied in this chapter are the same as those utilized in chapter 4. For detailed process information, please refer to chapter 4.2.2.

5.2.3 Flow rate measurement and estimation

The whole process of this chapter was exhibited in Fig.5-1. Flow rates were generalized with several common flow estimation hypotheses. The generalized and patient-specific flow rates were examined. Among the generalized group, the one showed closest flowrate estimation to the specific group, was applied in CFD. WSS obtained from the simulation results with both generalized and specific boundary conditions was compared.

The specific flow velocity and VA diameters were detected via Doppler ultrasound and the details have already been explained in chapter 4.2.3. The flow rates obtained from the specific flow velocity and diameters were considered as the control group.

On the other hand, the VA diameters information applied in all generalized groups were obtained from our reconstructed models. This means the VA diameter information was extracted from MRA imaging. We did this because in many studies, when having no access to specific flow information, the morphology information becomes the only specific available resource. Based on the segmentation position of our MRA test, the VA diameter of our models was the entrance of V4 segment on the whole VA.

The generalized flow rates can be divided into five groups (Table.5-1). And the details are explained as follows:

Groups 1–3: the BA flow rate was extracted from a previous study collecting the BA data of 125 Japanese patients [121]. Three groups with different methods of applying this average BA flow rate are listed:

- Group 1: The reference BA flow rate was directly applied as the BA flow rate. The VA flow rate was calculated by dividing this BA flow rate with the cube law.

- Group 2: The reference generalized BA flow rate was scaled with the BA diameter from the same reference paper as follows:

$$\frac{Flow\ rate\ in\ reference\ paper}{Flow\ rate\ in\ group\ 2} = \frac{BA\ diameter\ in\ reference\ paper}{BA\ diameter\ in\ our\ model} \qquad (5\text{-}1)$$

Then this calculated BA flow rate will be divided into two VA flow rates with the cube law.

- Group 3: The reference extracted BA flow rate was scaled using the BA area as follows:
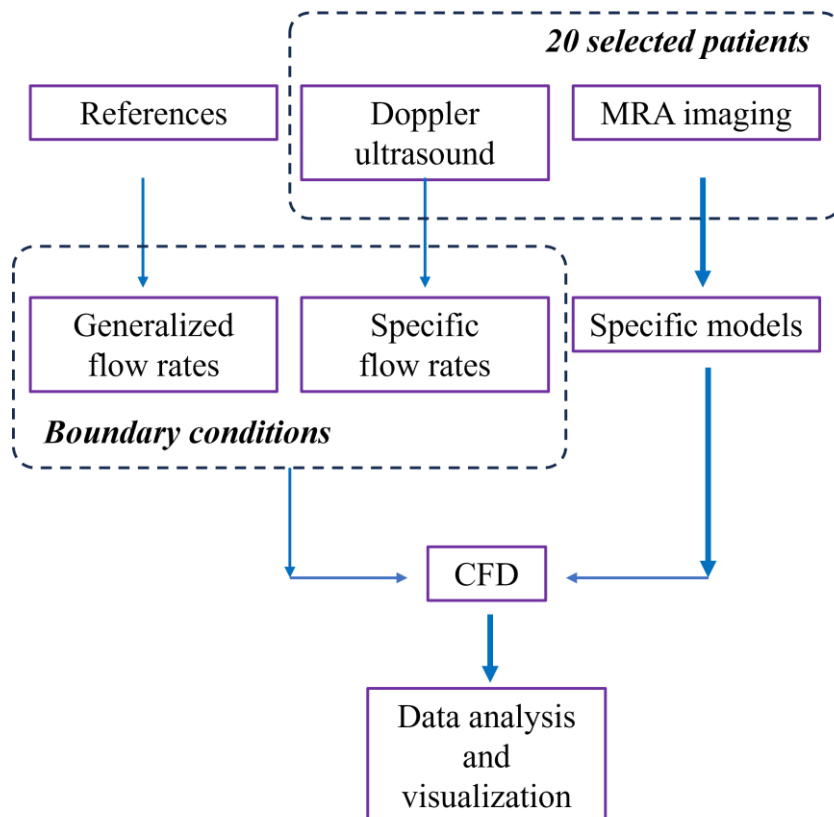
Figure 5-1 Process flowchart: the process of the methods utilized in this chapter.

$$\frac{Flow\ rate\ in\ reference\ paper}{Flow\ rate\ in\ group\ 3} = \left(\frac{BA\ area\ in\ reference\ paper}{BA\ area\ in\ our\ model}\right)^{1.84} \qquad (5\text{-}2)$$

according to the area–flow relationship proposed by Cebral et al. [146]. Again, this calculated BA flow rate was divided using the cube law.

The cube law was applied in Groups 1–3 because it was the principle representing the minimum work physiology at artery branching positions [147]. This cube law has been widely used in hemodynamic CFD simulations [148], [149].

The estimation methods in group 4 and 5 were a bit different. Instead of using the reference extracted BA flow rate, the area-flow relationship was directly applied. The details are as follows:

- Group 4: The equation of the area–flow relationship published by Cebral et al. [146] was applied to BA and was then the calculated BA flow rate was divided into the VA flow rates based on the cube law.

- Group 5, The area-flow equation was directly applied to the VA diameters obtained from the reconstructed models.

5.2.4 CFD

The 3D CFD simulation was performed employing different groups of boundary conditions respectively. From the five groups of generalized VA flow rates, we identified the group that closely matched the specific flow rate. All other CFD parameters remained consistent with the details outlined in section 4.2.4.

5.2.5 Data analysis and visualization

A boxplot was employed to assess variations in WSS magnitude between the specific boundary condition group and the closest generalized group. Additionally, to further explore the similarities and differences in WSS distributions, normalization of WSS was conducted for each simulation separately utilizing the following calculation:

$$WSS_{normalized} = \frac{WSS\ at\ each\ node}{averaged\ WSS\ of\ this\ model} \qquad (5\text{-}3)$$

Subsequently, scatter plots were utilized to compare the WSS and its distribution simulated from the control and generalized boundary condition groups at the same node.

To identify the position exhibiting the most obvious variation between the control and generalized groups, the deviation of the normalized WSS on each node was defined as follows:

$$WSS_{deviation} = \frac{WSS_{generalized\ group} - WSS_{control\ group}}{WSS_{control\ group}} \qquad (5\text{-}4)$$

and the results were visualized using Paraview 5.4.1 (Sandia National Labs, Kitware Inc, and Los Alamos National Labs. http://paraview.org). Linear regression lines were applied to the scatterplots to illustrate the transformation from the generated flow rate group to the control group, expressed as y = k × x, where *k* represents a constant number.

5.3 Results

5.3.1 VA measurements

The flow rates in the VAs demonstrated the following pattern: the control group had lower values than any of the generated groups and the results were exhibited in Fig.5-2. The nearest group was Group 1, where the reference BA flow rate value was directly applied and scaled using the cube law. Groups 3 and 5 exhibited large differences compared to the specific ones. The estimated flow rates displayed a tendency toward overestimation. Even in Group 1, 18 out of 20 cases showed larger BA flow rates compared to the control group.

The VA diameter obtained from the Doppler ultrasound test (LVA = 3.44 ± 0.64 mm; RVA = 3.16 ± 0.50 mm) showed no significant difference from the VA diameters extracted from the 3D models.

5.3.2 WSS magnitude

Group 1 exhibited the smallest difference compared to the specific group, and the WSS results are shown in Fig.5-3 in box charts. Out of 20 cases, a total of 18 showed WSS values simulated from Group 1 boundary conditions that were, on average, larger than those simulated from the control group. Cases No. 18 and 20 were the only two instances where the quantiles of the WSS in Group 1 were lower than those in the control group. Additionally, it was observed that the WSS range in the control group was smaller than that in Group 1, with a lower number of outliers. Case 20 was the only instance where the WSS of Group 1 was obviously lower than that detected in the control group, aligning with the BA flow rate results.

5.3.3 WSS distribution

Fig.5-4 and Fig.5-5 illustrate WSS distributions of Group 1 and the control group, respectively. It can be observed that WSS distributions in both groups were showing similarities to each other. To explore this similarity, scatter plots were employed. Plots of WSS in Group 1 versus the control group were generated, as well as the normalized WSS in Group 1 versus the control group, as presented in Fig.5-6.

WSS results on each simulation node were extracted. Since the same models were applied and simulated with different boundary conditions, we received the WSS results on the same coordinates under different boundary conditions and exhibited them with scatter plots. The first column of Fig.5-6 on the left exhibited the plots of WSS in Group 1 vs. the control group. The linear regression equation was applied and estimated as $y = k \times x$ to demonstrate the correlation between WSS in Group 1 and the control group, where k represented a constant number. The mean adjusted R^2 of the regression equation is 0.96 ± 0.04, which implied that WSS values in the control group are almost the same with the WSS values in Group 1 multiplied by k. The Group 1 results could be considered as the results in the control group after zooming. Notably, although WSS in Group 1 and control group can be concluded into a linear correlation, k varied in different cases,

The column of Fig.5-6 on the right exhibited the scatter plots of the normalized WSS in Group 1 vs. the control group. The average slope of the normalized WSS was 0.96 and ranged from 0.83 to 1.00, implying that the maximum average deviation in WSS distribution caused by the Group 1 was around 17% in all 20 cases. The adjusted R^2 of the regression equation exceeded 0.87 in 18 cases. In addition, the only 2 cases exhibiting a regression slope < 0.9 (0.83 and 0.88, respectively) were also two cases with a relatively low adjusted R^2 (0.71 and 0.79, respectively).

The visualized results of the deviations were exhibited in Fig.5-7. The two columns were showing the visualized normalized WSS deviation results in anterior-posterior view and left-right view. Cases with a typical VA–BA morphology, including the so-called 'tuning fork' and 'walking' types [31] were selected. It was observed that relatively large deviations (red regions in the figures) tended to happen at the VA–BA junction, at the BA–PCA junction, and sometimes at the outer curve.

Table 5-1 Generalization process of boundary conditions

Group		Data source	BA flow rate	The method of division into VA flow rate	Average flow rates[g/s]
Control group		Specific flow rates measured with Doppler Ultrasound			RVA:0.82 LVA:1.18
Generalized groups	1	Collected BA data of 125 Japanese [121]	Directly used reference data	Cube law	RVA:1.34 LVA:1.56
	2		Scaled with diameter	Cube law	RVA:1.57 LVA:1.89
	3	The area–flow relationship proposed by Cebral et al [146]	Scaled with area	Cube law	RVA:2.52 LVA:3.35
	4		Equation applied with BA area	Cube law	RVA:1.61 LVA:2.13
	5		Summary of estimated VA flow rate based on equation	Equation applied with VA areas	RVA:2.20 LVA:3.61
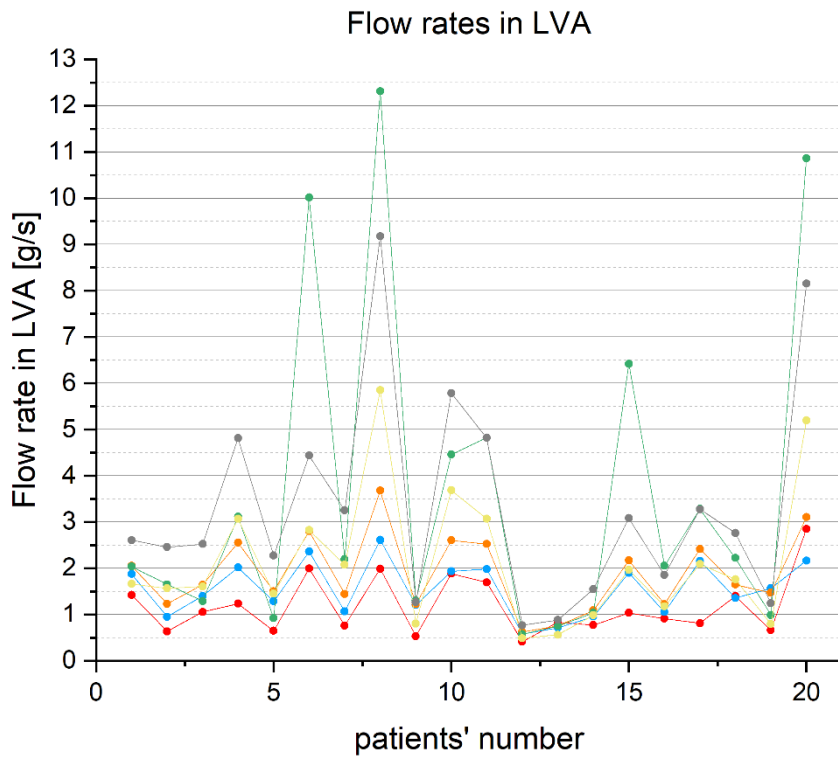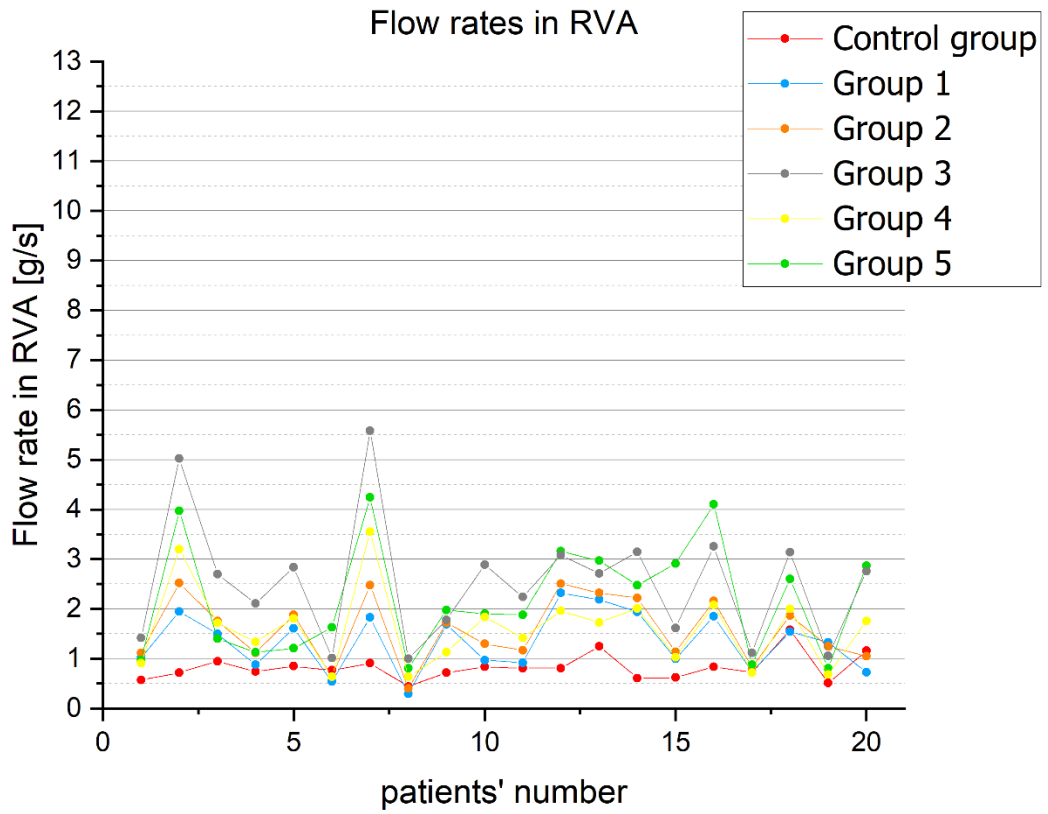
Figure 5-2 VA measurements: the flowrate estimated in the control group and reference generated group 1 to 5.

5.4 Discussion

In this investigation, we demonstrated a consistent trend where the generalized flow rates were notably higher than the specific flow rates on a large scale. This difference had a substantial impact on the hemodynamic simulation outcomes, resulting in generally larger WSS values when using generalized flow rates compared to specific flow rates. However, it was further observed that the WSS distribution exhibited similarities in both simulation groups. Despite the variations introduced by the generalized boundary conditions in simulating WSS magnitude, they could still be effectively utilized when studying distributions and relative hemodynamic relationships.

5.4.1 Flow rate estimation

In the context of flow rate estimation, several hypotheses employed in previous CFD studies were applied, revealing a prevalent tendency: the generalized boundary conditions led to an overestimation of the flow rate. Even in Group 1, considered the closest to the specific results, 18 out of 20 cases exhibited an estimated total BA flow rate larger than in Group 1. As shown in Fig.5-2, Group 1 demonstrated the closest flow rate compared to the control group, which was the only group with no scaling of the reference BA flow rate. In contrast, the remaining groups involved more extensive estimation steps than Group 1. The scaling process
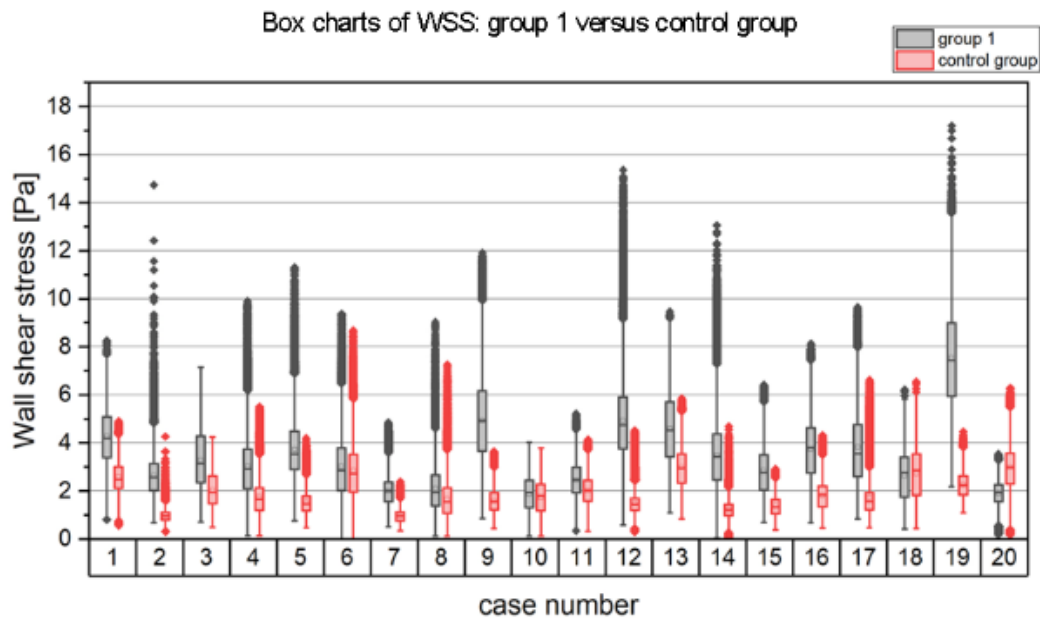

Figure 5-3 Comparison of WSS between group1 and control group

© 2023 IEEE

itself potentially amplified the differences in the estimated BA flow rate compared to the control group. It was evident that the process of integrating hypotheses during flow rate estimation introduced a bias.

The scaling principle and reference data applied were derived from healthy young individuals. Given that VA velocity tends to decrease with age while VA diameters typically remain constant [19], [33], the impact of age on flow rates was neglected in our estimation process. Consequently, as most study subjects were elderly patients, the overestimation of VA flow rates was consistent throughout all generalized groups.

5.4.2 BA variation

The majority of cases exhibited an overestimation of the WSS magnitude. Interestingly, two cases (case No.18 and 20) demonstrated smaller WSS in Group 1 than in the control group. These exceptional cases were also characterized by generalized BA total flow rates that were less than those in the control group. Considering they represented the cases with the largest flow rates in the control group, it could be inferred that larger BA flow rates contribute to a larger WSS range. Case No. 18 showed nearly identical WSS simulation results in both groups, while Case No. 20 stood out as the only case where the WSS value obtained using specific boundary conditions was significantly greater than that obtained using Group 1 boundary conditions.

Additionally, the WSS simulated using the control group had a 75th percentile $\leqslant 4$ Pa, aligning with previous simulation results [31] obtained under specific conditions. This WSS range was close to the WSS results reported in a cell study, where WSS values <1.5 and >4 Pa were identified as special thresholds [120] adhering to the autoregulation principle in biological systems. However, the WSS range in Group 1 significantly exceeded the range observed in cell studies in certain cases. If the study's focus is related to WSS values, patient-specific measurements may be necessary for establishing boundary conditions.

5.4.3 WSS distribution

Figure 5-4 and Fig.5-5 illustrated the WSS characteristics in Group 1 closely resemble those in the control group. Positions with high and low WSS values align between the two groups. This similarity is further confirmed by the scatter plots in Fig.5-6, where the WSS results from Group 1 and the control group exhibit strong linear correlations with high adjusted R^2. This demonstrated that the Group 1 WSS distribution was able to be represented as the specific WSS multiplied with the rate k. The regression equation $y = k \times x$ varies with a different

constant *k* in different cases. Identifying the factors influencing the constant *k* could contribute to refining boundary conditions.

After normalization, the scatter plots of normalized specific WSS values demonstrate a tendency to cluster around the linear equation y = x. This further verified our promotion that generalized boundary conditions are applicable for simulating WSS distributions. If the focus is limited to the relative relationships of WSS, the simulation results derived from the estimated flow rates can offer similar outcomes compared to the specific flow rates, particularly after normalization. Even in the two cases exhibiting a slope < 0.9 after linear regression, along with a relatively low adjusted R^2, the slopes remained > 0.83 and the adjusted R^2 was > 0.7. These two cases also displayed substantial side-to-side VA differences, potentially explaining the variation in their distribution.

5.4.4 Limitations

This study had several limitations. Firstly, the specific boundary conditions utilized were derived from routine Doppler ultrasound, and while intraindividual velocity variation has been documented [150], we employed snapshot data of blood velocity as the control group. The selected cases for the control group had an interval of 1 week between MR angiography and Doppler check.

Secondly, our CFD simulations were performed with several assumptions. Given that our primary focus was on contrasting specific and generalized boundary conditions, we simplified the simulations as steady using a pressure outlet with 0 Pa. The blood flow was modeled as Newtonian flow with a constant density, and this simplification should not substantially impact our findings, as evidenced by Cebral et al.'s work [151].

Lastly, the study included only 20 cases. Therefore, additional cases will support our conclusions. While additional cases would enhance the robustness of our conclusions, the consistent tendency observed in all 20 cases—namely, the similarity in WSS distributions between patient-specific and generalized boundary condition simulations—supports the promotion of using generalized boundary conditions in hemodynamic distribution studies.

5.5 Conclusion

In summary, the flow rate estimation without scaling demonstrated the closest proximity to the patient-specific data. The scaling of the flow rate without accounting for age-related decrease in flow rates may result in an overestimation of the generalized flow rates.

An overestimation of the CFD results was observed when simulated from generalized boundary conditions due to the overestimated flow rates, implying that the WSS values obtained from generalized boundary conditions exhibited variations from the specific ones. However, the WSS obtained when employing the generalized boundary condition was found
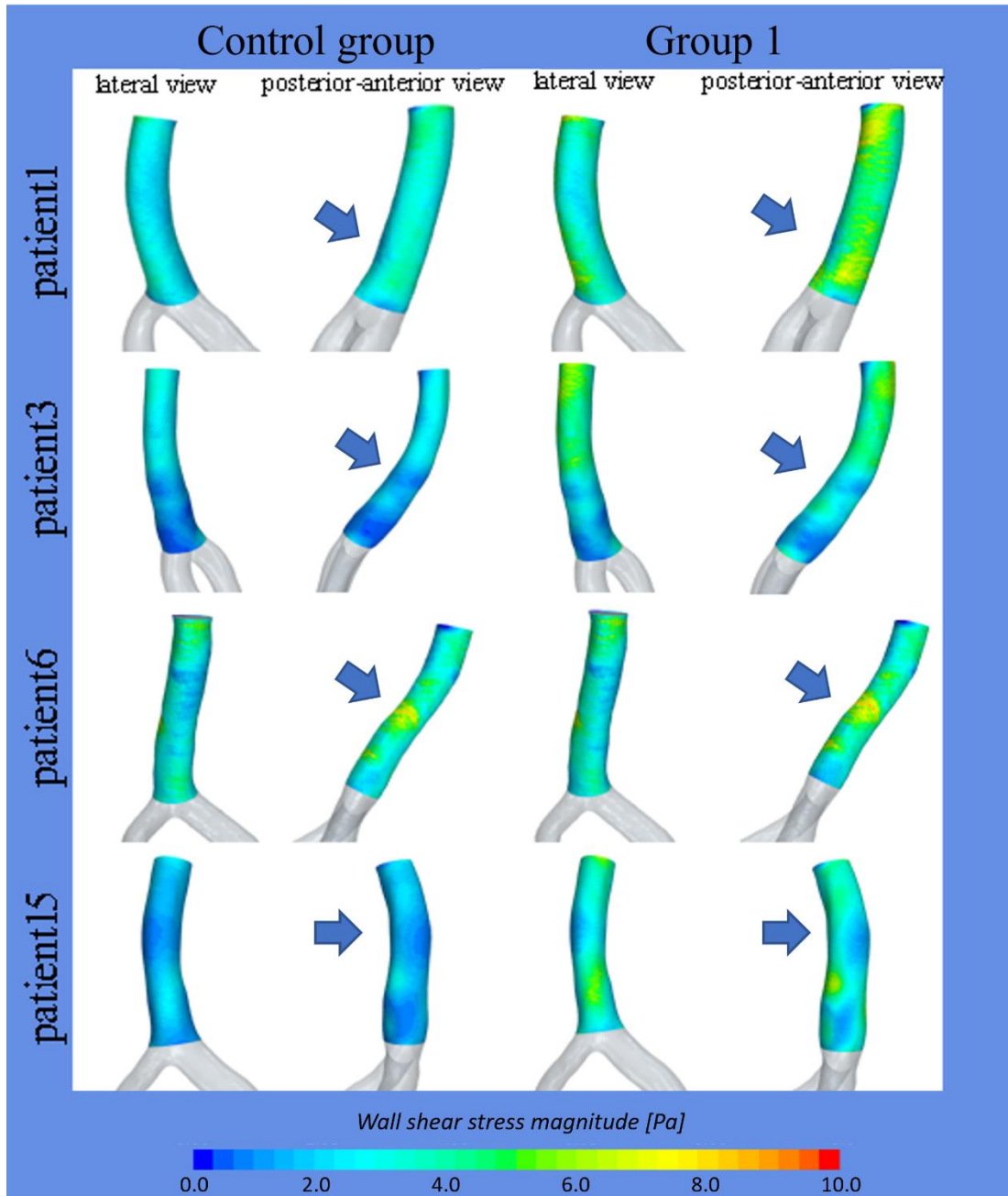
Figure 5-4 WSS distributions: WSS distributions in Group 1 and the control group. 4 examples' results were demonstrated to show the similarities between the control group and Group 1. Two cases were shown in one line and in each case, the first column was the result in control group and the second column was the result in group 1. Each simulation result is reported using a poster-anterior view.

to be the WSS obtained with the specific condition multiplied by the constant k. Identifying the factors influencing k will contribute to the development of a more accurate generalized boundary condition in future studies.
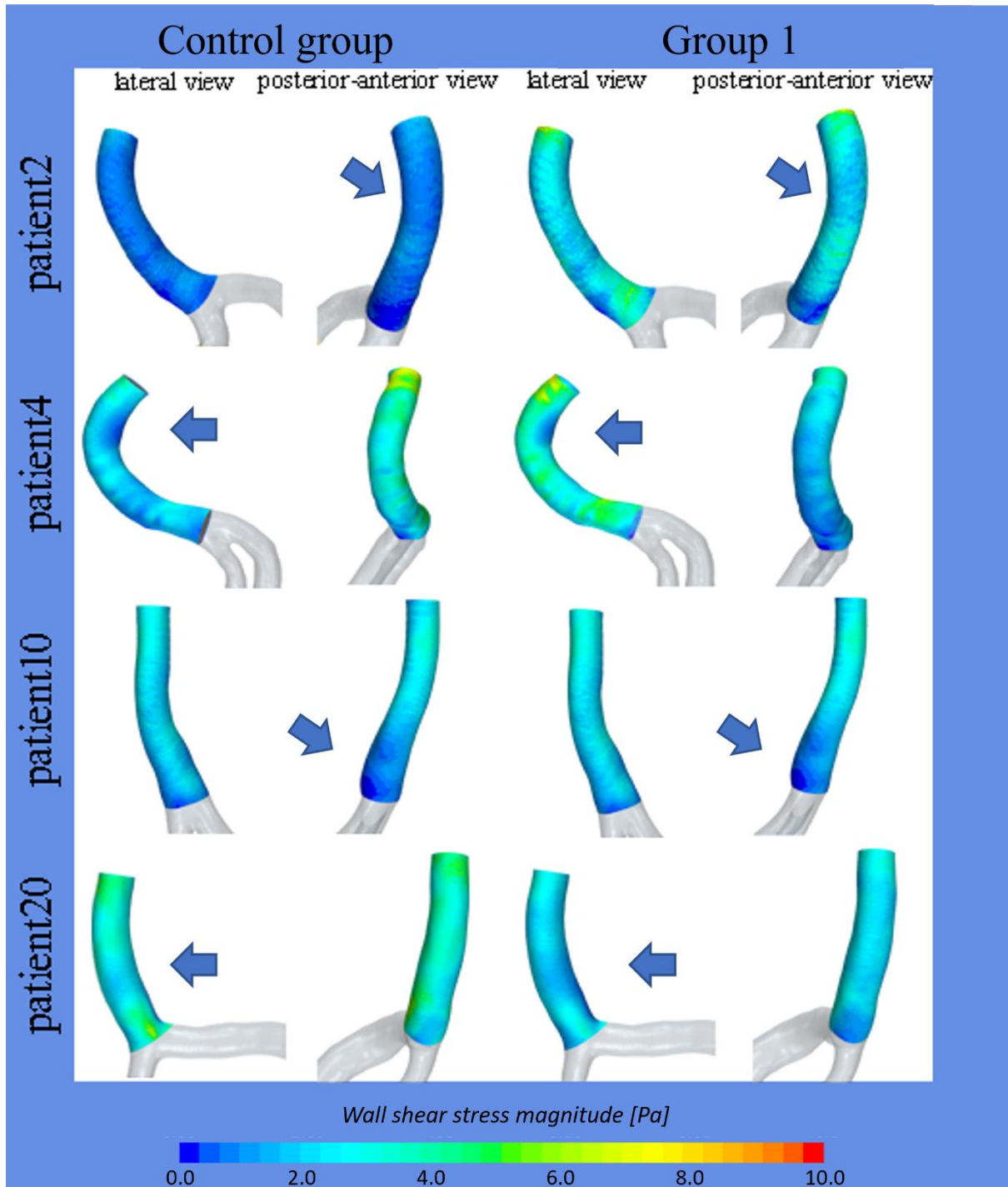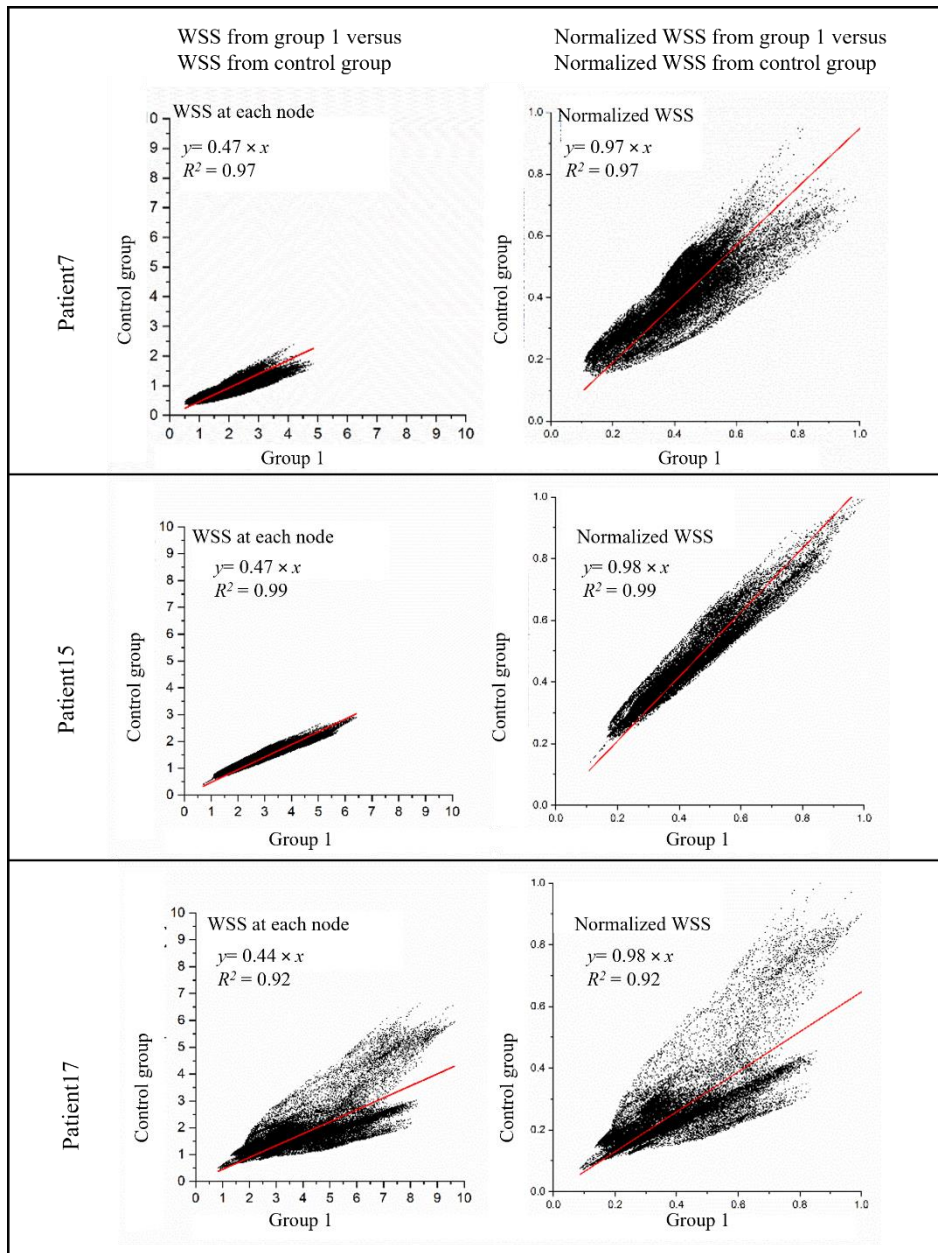

Figure 5-5 WSS distributions: the exhibition of more cases.

Figure 5-6 Distribution similarity: the similarity of WSS from Group 1 and the control group was exhibited with three examples, with each line referring to one case. The first column on the left presents the scatter plot of the WSS in Group 1 versus the control group. The second column on the left presents the scatter plot of the normalized WSS in Group 1 versus the control group. Almost all scatterplots were showing strong linear correlations between two groups.
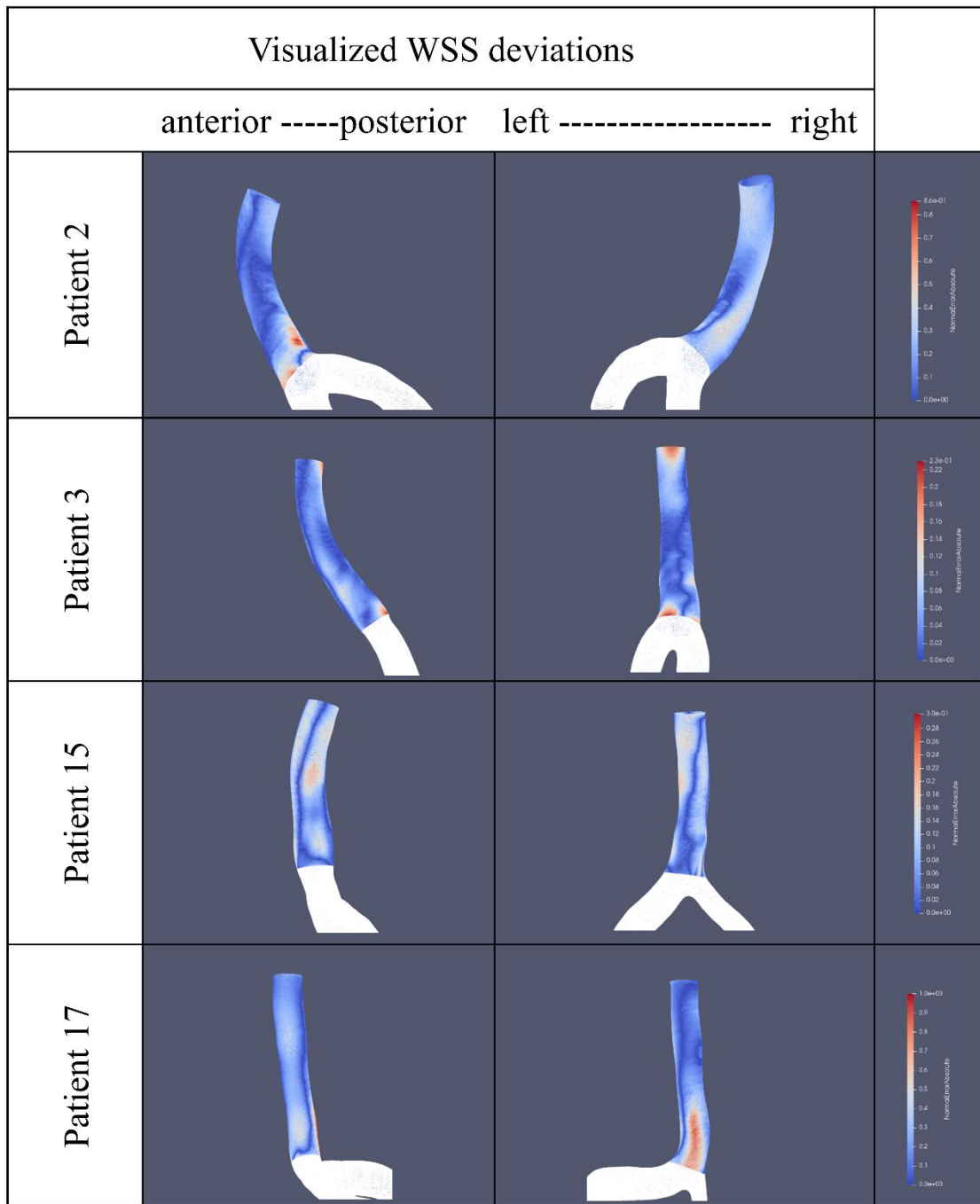
Figure 5-7 Visualization of deviation: the column on the left pertain to the visualized normalized WSS deviation from anterior-posterior view and the right column showed left-right view. It was observed that relatively large deviations tended to occur at the VA–BA junction.

Chapter 6

Conclusion

Chapter 6   Conclusion

This thesis was described mainly to introduce the quantified correlations between vascular geometric features and WSS. The purpose of this thesis work was to propose different influence degree brought by various geometric factors, as well as blood velocity, on WSS. With this connection, we could make a rough estimation of hemodynamic situations from geometric features. We did this work to help find the biomarkers for aneurysm prediction and early detection.

Chapter 1: Aneurysms have always been known for their high mortality after rupture and their hardness for early detection before the rupture or before its rapid growth. This feature of IA motivated us to perform studies on primary prevention of IAs. IAs are not happening evenly throughout the vasculature system but with its own locational preference. Previous studies revealed that hemodynamic stress is a vital contributor to this unevenness of formation locations. To study on the pre-disease risk assessment, we are supposed to know the recent studies of hemodynamics working on IA occurrence. In response to this need, the present thesis first made the report of literature review on aneurysm formation and growth and summarized the results in the following chapter.

Chapter 2: According to the literature review, previous studies proposed IA as a focal disease and different vessels are exposed to different risk of aneurysm initiation. Further studies with computational simulations as well as cell experiments and animal experiments confirmed that this location preference of aneurysm is the result of hemodynamic forces, which is known as the force brought by blood flow on vessel walls.

This connection between hemodynamic force and vessel geometry attracted research studying on using geometry features as one criterion for risk assessment for aneurysm initiation. Among the hemodynamic parameters, WSS has become the one under spotlight for its directly representing the frictional force of the blood on vessel wall.

However, although several previous studies pointed out few geometry parameters connected closely to WSS, we noticed that there lack the detailed numerical studies on these correlations. We aimed to make our work an initial step of correlating vascular geometric features and WSS in a numerical way. From the complicated interactions brought by different factors on WSS, this thesis worked to extract the most important geometric feature and proposed it as an avenue for further research, highlighting its significant impact on WSS.

Chapter 3: In this chapter, we performed a study on correlations between vascular angles and aneurysm locations. By separating BA aneurysms into BA tip and BA trunk aneurysms, the significant differences existing in vascular angles around BA apex in different aneurysm sites was confirmed. From these results, we understand that even BA tip and BA trunk aneurysms are both BA aneurysms, the variation among vessel shapes can be large.

Chapter 4: In this chapter, we further seek the correlation between vascular geometric features and WSS. We divided WSS into different WSS quantiles to have a comprehensive observation. The results turned out that the velocity at bifurcation conjunctions (called as proximal velocity of BA in this thesis) became the most influential factor for almost all WSS quantiles except for the 2.5^{th} WSS quantile. Mean BA diameter showed almost equal, even slightly larger influence than the proximal velocity on the 2.5^{th} WSS quantile.

So, we get to know that if we want to focus on relatively low WSS of an individual, the vessel diameter cannot be neglected.

In addition, although varying among different quantiles, the proximal velocity could predict around 60% of the WSS results. The prediction percentage decreases with the decrease of WSS, implying that causes of low WSS are more complicated than that of high WSS regions.

Chapter 5: In this chapter, we made a numerical analysis on the difference brought by specific and generalized boundary conditions on WSS results. Results turned out that WSS magnitude calculated with reference generalized boundary conditions has an overestimation tendency when compared to that of specific boundary conditions. However, it does not mean that generalized boundary conditions cannot be used. WSS distributions from both boundary conditions are highly similar. The regression results of normalized WSS results between the specific group and generalized group showed an average R^2 higher than 0.9. WSS distributions simulated with generalized boundary conditions could still be relied on.

In summary, this thesis worked on the quantified correlation between vascular geometric features and WSS. In addition, we also introduced the connection between vascular angles and aneurysm sites, as well as the comparison between specific and generalized boundary conditions.

With the results above, we would like to propose the proximal velocity and average vessel diameter as factors worth more attention for pre-disease risk assessment. This thesis work would like to provide the initial step of quantifying geometric features influencing WSS and help future studies on aneurysm primary preventions.

References

[1] A. M. Jersey and D. M. Foster, "Cerebral Aneurysm.," Treasure Island (FL), 2023.

[2] J. Song, Y. C. Lim, I. Ko, J. Y. Kim, and D. K. Kim, "Prevalence of Intracranial Aneurysms in Patients With Systemic Vessel Aneurysms: A Nationwide Cohort Study," *Stroke*, vol. 51, no. 1, pp. 115–120, 2020.

[3] J. Liu *et al.*, "Prevalence and Risk Factors for Unruptured Intracranial Aneurysms in the Population at High Risk for Aneurysm in the Rural Areas of Tianjin," *Front. Neurol.*, vol. 13, no. March, pp. 1–8, 2022.

[4] L. Pyysalo, T. Luostarinen, L. Keski-Nisula, and J. Öhman, "Long-term excess mortality of patients with treated and untreated unruptured intracranial aneurysms," *J. Neurol. Neurosurg. Psychiatry*, vol. 84, no. 8, pp. 888–892, 2013.

[5] H. Meng, V. M. Tutino, J. Xiang, and A. Siddiqui, "High WSS or Low WSS? Complex interactions of hemodynamics with intracranial aneurysm initiation, growth, and rupture: Toward a unifying hypothesis," *Am. J. Neuroradiol.*, vol. 35, no. 7, pp. 1254–1262, 2014.

[6] H. M. Finlay, P. Whittaker, and P. B. Canham, "Collagen organization in the branching region of human brain arteries," *Stroke*, vol. 29, no. 8, pp. 1595–1601, 1998.

[7] D. G. Nehls, R. A. Flom, L. P. Carter, and R. F. Spetzler, "Multiple intracranial aneurysms: Determining the site of rupture," *J. Neurosurg.*, vol. 63, no. 3, pp. 342–348, 1985.

[8] C. O. Willis, K. N. T. Kayembe, M. Sasahara, and F. Hazama, "Cerebral aneurysms and variations in the," *Stroke*, vol. 15, no. 5, pp. 846–850, 1984.

[9] M. Piccinelli *et al.*, "Geometry of the internal carotid artery and recurrent patterns in location, orientation, and rupture status of lateral aneurysms: An image-based computational study," *Neurosurgery*, vol. 68, no. 5, pp. 1270–1285, 2011.

[10] A. Lauric, J. Hippelheuser, M. G. Safain, and A. M. Malek, "Curvature effect on hemodynamic conditions at the inner bend of the carotid siphon and its relation to aneurysm formation," *J. Biomech.*, vol. 47, no. 12, pp. 3018–3027, 2014.

[11] B. Zhang, J. Gu, M. Qian, L. Niu, and D. Ghista, "Study of correlation between wall shear stress and elasticity in atherosclerotic carotid arteries," *Biomed. Eng. Online*, vol. 17, no. 1, pp. 1–11, 2018.

[12] R. M. Krzyżewski, K. M. Kliś, B. M. Kwinta, M. Gackowska, and J. Gąsowski, "Increased tortuosity of ACA might be associated with increased risk of ACoA aneurysm development and less aneurysm dome size: a computer-aided analysis," *Eur. Radiol.*, vol. 29, no. 11, pp. 6309–6318, 2019.

[13] K. M. Kliś *et al.*, "Increased tortuosity of basilar artery might be associated with higher risk of aneurysm development," *Eur. Radiol.*, vol. 30, no. 10, pp. 5625–5632, 2020.

[14] P.-E. Labeyrie *et al.*, "Cervical artery tortuosity is associated with intracranial aneurysm.," *Int. J. stroke Off. J. Int. Stroke Soc.*, vol. 12, no. 5, pp. 549–552, Jul. 2017.

[15] B. J. Kim *et al.*, "Intracranial Aneurysm Is Associated with High Intracranial Artery Tortuosity," *World Neurosurg.*, vol. 112, pp. e876–e880, 2018.

[16] K. Kono, T. Fujimoto, and T. Terada, "Proximal stenosis may induce initiation of cerebral aneurysms by increasing wall shear stress and wall shear stress gradient.," *Int. j. numer. method. biomed. eng.*, vol. 30, no. 10, pp. 942–950, Oct. 2014.

[17] T. Ingebrigtsen, M. K. Morgan, K. Faulder, L. Ingebrigtsen, T. Sparr, and H. Schirmer, "Bifurcation

geometry and the presence of cerebral artery aneurysms," *J. Neurosurg.*, vol. 101, no. 1, pp. 108–113, 2004.

[18]   F. Tütüncü *et al.*, "Widening of the basilar bifurcation angle: Association with presence of intracranial aneurysm, age, and female sex," *J. Neurosurg.*, vol. 121, no. 6, pp. 1401–1410, 2014.

[19]   A. S. E. Bor, B. K. Velthuis, C. B. Majoie, and G. J. E. Rinkel, "Configuration of intracranial arteries and development of aneurysms," *Neurology*, vol. 70, no. 9, pp. 700 LP – 705, Feb. 2008.

[20]   S. Soldozy *et al.*, "The biophysical role of hemodynamics in the pathogenesis of cerebral aneurysm formation and rupture," *Neurosurg. Focus*, vol. 47, no. 1, pp. 1–9, 2019.

[21]   H. Tang *et al.*, "Underlying mechanism of hemodynamics and intracranial aneurysm," *Chinese Neurosurg. J.*, vol. 7, no. 1, pp. 1–8, 2021.

[22]   E. Metaxa *et al.*, "Characterization of critical hemodynamics contributing to aneurysmal remodeling at the basilar terminus in a rabbit model," *Stroke*, vol. 41, no. 8, pp. 1774–1782, 2010.

[23]   L. Gao, Y. Hoi, D. D. Swartz, J. Kolega, A. Siddiqui, and H. Meng, "Nascent aneurysm formation at the basilar terminus induced by hemodynamics," *Stroke*, vol. 39, no. 7, pp. 2085–2090, 2008.

[24]   S. W. Nam, S. Choi, Y. Cheong, Y. H. Kim, and H. K. Park, "Evaluation of aneurysm-associated wall shear stress related to morphological variations of circle of Willis using a microfluidic device," *J. Biomech.*, vol. 48, no. 2, pp. 348–353, 2015.

[25]   P. Machi *et al.*, "Hemodynamics of Focal Versus Global Growth of Small Cerebral Aneurysms," *Clin. Neuroradiol.*, vol. 29, no. 2, pp. 285–293, 2019.

[26]   C. Doenitz, K. M. Schebesch, R. Zoephel, and A. Brawanski, "A mechanism for the rapid development of intracranial aneurysms: A case study," *Neurosurgery*, vol. 67, no. 5, pp. 1213–1221, 2010.

[27]   T. Hassan *et al.*, "Erratum: A proposed parent vessel geometry-based categorization of saccular intracranial aneurysms: Computational flow dynamics analysis of the risk of factors for lesion rupture (Journal of Neurosurgery (October, 2005) 103 (662-680))," *J. Neurosurg.*, vol. 103, no. 6, p. 1110, 2005.

[28]   K. M. Kliś *et al.*, "Association of Arterial Tortuosity with Hemodynamic Parameters—A Computational Fluid Dynamics Study," *World Neurosurg.*, pp. 1–8, 2023.

[29]   Q. Zhang, D. A. Steinman, and M. H. Friedman, "Use of factor analysis to characterize arterial geometry and predict hemodynamic risk: Application to the human carotid bifurcation," *J. Biomech. Eng.*, vol. 132, no. 11, pp. 1–5, 2010.

[30]   A. L. S. Davim, J. F. S. Neto, and D. F. Albuquerque, "Anatomical variation of the superior cerebelar artery: A case study," *J. Morphol. Sci.*, vol. 27, no. 3–4, pp. 155–156, 2010.

[31]   A. K. Wake-Buck, J. C. Gatenby, and J. C. Gore, "Hemodynamic Characteristics of the Vertebrobasilar System Analyzed Using MRI-Based Models," *PLoS One*, vol. 7, no. 12, 2012.

[32]   A. R. Tsantili *et al.*, "Anatomical variations of human vertebral and basilar arteries: A current review of the literature," *Morphologie*, vol. 107, no. 357, pp. 169–175, 2023.

[33]   S. Kalaiyarasi, T. Sivakami, and S. Sumathi, "Anatomical Variability in the Origin, Length and Termination of Basilar Artery and its Clinical Implications," *Int. J. Anat. Radiol. Surg.*, no. April 2020, pp. 9–13, 2022.

[34]   A. Usha Vijayakumar, M. Sudhakaran, and L. Janaki Yovel, "Human basilar artery: morphology & variations," *AIMS Med. Sci.*, vol. 7, no. 4, pp. 278–292, 2020.

[35]   V. Akgun *et al.*, "Normal anatomical features and variations of the vertebrobasilar circulation and its branches: An analysis with 64-detector row CT and 3T MR angiographies," *Sci. World J.*, vol. 2013, 2013.

[36]   N. J. Giffin and P. J. Goadsby, "Basilar artery aneurysm with autonomic features: An interesting pathophysiological problem," *J. Neurol. Neurosurg. Psychiatry*, vol. 71, no. 6, pp. 805–808, 2001.

[37]   H. Ge, X. Lv, H. Jin, Z. Tian, Y. Li, and H. He, "The role of endovascular treatment in unruptured basilar tip aneurysms.," *Interv. Neuroradiol. J. peritherapeutic Neuroradiol. Surg. Proced. Relat. Neurosci.*, vol. 23, no. 1, pp. 8–13, Feb. 2017.

[38]   J. Y. Chung, H. G. Kang, D. S. Shin, and H. S. Han, "Rapidly Growing Basilar Tip Aneurysm Causing Hydrocephalus and Mental Deterioration," *J Neurocrit Care*, vol. 8, no. 2, pp. 130–132, Dec. 2015.

[39]   H. Koffijberg, E. Buskens, A. Algra, M. J. H. Wermer, and G. J. E. Rinkel, "Growth rates of intracranial aneurysms: Exploring constancy," *J. Neurosurg.*, vol. 109, no. 2, pp. 176–185, 2008.

[40]   S. Juvela, K. Poussa, and M. Porras, "Factors affecting formation and growth of intracranial aneurysms: A long-term follow-up study," *Stroke*, vol. 32, no. 2, pp. 485–491, 2001.

[41]   F. WD, "On the origin of military aneurysms of the superficial cerebral arteries," *Bull Johns Hopkins Hosp*, vol. 47, pp. 239–284, 1930.

[42]   L. E. Glynn, "Medial defects in the circle of willis and their relation to aneurysm formation," *J. Pathol. Bacteriol.*, vol. 51, no. 2, pp. 213–222, 1940.

[43]   R. CARMICHAEL, "The pathogenesis of noninflammatory cerebral aneurysms.," *J. Pathol. Bacteriol.*, vol. 62, no. 1, pp. 1–19, Jan. 1950.

[44]   O. Hassler, "Morphological studies on the large cerebral arteries, with reference to the aetiology of subarachnoid hemorrhage," *Acta Psychiatr Scand*, vol. 154, p. 1, 1961.

[45]   W. Stehbens, "Histopathology of cerebral aneurysms," *Arch. Neurol.*, vol. 8, no. 3, pp. 272–285, 1963.

[46]   S. M. de la Monte, G. W. Moore, M. A. Monk, and G. M. Hutchins, "Risk factors for the development and rupture of intracranial berry aneurysms," *Am. J. Med.*, vol. 78, no. 6 PART 1, pp. 957–964, 1985.

[47]   S. Waga, M. Okada, and T. Kojima, "Saccular aneurysm associated with absence of the left cervical carotid arteries.," *Neurosurgery*, vol. 3, no. 2, pp. 208–212, 1978.

[48]   M. H. M. Vlak, G. J. E. Rinkel, P. Greebe, and A. Algra, "Risk of rupture of an intracranial aneurysm based on patient characteristics: A case-control study," *Stroke*, vol. 44, no. 5, pp. 1256–1259, 2013.

[49]   W. Kaspera *et al.*, "Morphological, hemodynamic, and clinical independent risk factors for anterior communicating artery aneurysms," *Stroke*, vol. 45, no. 10, pp. 2906–2911, 2014.

[50]   N. Hashimoto, H. Handa, and F. Hazama, "Experimentally induced cerebral aneurysms in rats.," *Surg. Neurol.*, vol. 10, no. 1, pp. 3–8, Jul. 1978.

[51]   N. Hashimoto, H. Handa, and F. Hazama, "Experimentally induced cerebral aneurysms in rats: part II.," *Surg. Neurol.*, vol. 11, no. 3, pp. 243–246, Mar. 1979.

[52]   F. Hazama *et al.*, "Early changes of experimentally induced cerebral aneurysms in rats. Light-microscopic study," *Am. J. Pathol.*, vol. 124, no. 3, pp. 399–404, 1986.

[53]   I. Nagata, H. Handa, N. Hashimoto, and F. Hazama, "Experimentally induced cerebral aneurysms in rats: Part VI. Hypertension.," *Surg. Neurol.*, vol. 14, no. 6, pp. 477–479, Dec. 1980.

[54]   N. Hashimoto, C. Kim, H. Kikuchi, M. Kojima, Y. Kang, and F. Hazama, "Experimental induction of cerebral aneurysms in monkeys," *J. Neurosurg.*, vol. 67, no. 6, pp. 903–905, 1987.

[55]   H. Nakatani *et al.*, "Cerebral blood flow patterns at major vessel bifurcations and aneurysms in rats," *J. Neurosurg.*, vol. 74, no. 2, pp. 258–262, 1991.

[56]   Y. Shimogonya, T. Ishikawa, Y. Imai, D. Mori, N. Matsuki, and T. Yamaguchi, "Formation of Saccular Cerebral Aneurysms May Require Proliferation of the Arterial Wall: Computational Investigation," *J. Biomech. Sci. Eng.*, vol. 3, no. 3, pp. 431–442, 2008.

[57]   S. Chien, "Mechanotransduction and endothelial cell homeostasis: The wisdom of the cell," *Am. J. Physiol. - Hear. Circ. Physiol.*, vol. 292, no. 3, 2007.

[58]   S. Fukuda *et al.*, "Prevention of rat cerebral aneurysm formation by inhibition of nitric oxide synthase," *Circulation*, vol. 101, no. 21, pp. 2532–2538, 2000.

[59]   T. Aoki *et al.*, "NF-κB is a key mediator of cerebral aneurysm formation," *Circulation*, vol. 116, no. 24, pp. 2830–2840, 2007.

[60]   T. Aoki *et al.*, "PGE 2-EP 2 signalling in endothelium is activated by haemodynamic stress and induces cerebral aneurysm through an amplifying loop via NF-κB," *Br. J. Pharmacol.*, vol. 163, no. 6, pp. 1237–1249, 2011.

[61]   T. Aoki *et al.*, "Prostaglandin E2-EP2-NF-κB signaling in macrophages as a potential therapeutic target for intracranial aneurysms.," *Sci. Signal.*, vol. 10, no. 465, Feb. 2017.

[62]   G. Redekop, K. TerBrugge, W. Montanera, and R. Willinsky, "Arterial aneurysms associated with cerebral arteriovenous malformations: Classification, incidence, and risk of hemorrhage," *J. Neurosurg.*, vol. 89, no. 4, pp. 539–546, 1998.

[63]   S. Miyamoto, T. Funaki, K. Iihara, and J. C. Takahashi, "Successful obliteration and shrinkage of giant partially thrombosed basilar artery aneurysms through a tailored flow reduction strategy with bypass surgery: Clinical article," *J. Neurosurg.*, vol. 114, no. 4, pp. 1028–1036, 2011.

[64]   J. M. Alfano *et al.*, "Intracranial aneurysms occur more frequently at bifurcation sites that typically experience higher hemodynamic stresses.," *Neurosurgery*, vol. 73, no. 3, pp. 497–505, Sep. 2013.

[65]   Z. Kulcsár, Á. Ugron, M. Marosfoi, Z. Berentei, G. Paál, and I. Szikora, "Hemodynamics of cerebral aneurysm initiation: The role of wall shear stress and spatial wall shear stress gradient," *Am. J. Neuroradiol.*, vol. 32, no. 3, pp. 587–594, 2011.

[66]   K. Yamamoto *et al.*, "Impaired flow-dependent control of vascular tone and remodeling in P2X4-deficient mice," *Nat. Med.*, vol. 12, no. 1, pp. 133–137, 2006.

[67]   M. Fukuda *et al.*, "Disruption of P2X4 purinoceptor and suppression of the inflammation associated with cerebral aneurysm formation.," *J. Neurosurg.*, vol. 134, no. 1, pp. 102–114, Dec. 2019.

[68]   C. Børup, B. Meidahl, I. M. Petersen, A. Vangtorp, and P. le Fèvre Honoré, "An early clinical phase II evaluation of paroxetine, a new potent and selective 5HT-uptake inhibitor in patients with depressive illness.," *Pharmacopsychiatria*, vol. 15, no. 6, pp. 183–186, Nov. 1982.

[69]   C. M. Kaye *et al.*, "A review of the metabolism and pharmacokinetics of paroxetine in man," *Acta Psychiatr. Scand.*, vol. 80, no. S350, pp. 60–75, 1989.

[70]   H. Koseki *et al.*, "Two Diverse Hemodynamic Forces, a Mechanical Stretch and a High Wall Shear Stress, Determine Intracranial Aneurysm Formation," *Transl. Stroke Res.*, vol. 11, no. 1, pp. 80–92, 2020.

[71]   W. I. Schievink, V. V. Michels, and D. G. Piepgras, "Neurovascular manifestations of heritable connective tissue disorders a review," *Stroke*, vol. 25, no. 4, pp. 889–903, 1994.

[72] R. M. Starke *et al.*, "Cigarette Smoke Initiates Oxidative Stress-Induced Cellular Phenotypic Modulation Leading to Cerebral Aneurysm Pathogenesis.," *Arterioscler. Thromb. Vasc. Biol.*, vol. 38, no. 3, pp. 610–621, Mar. 2018.

[73] L. Miskolczi, L. R. Guterman, J. D. Flaherty, and L. N. Hopkins, "Saccular aneurysm induction by elastase digestion of the arterial wall: a new animal model.," *Neurosurgery*, vol. 43, no. 3, pp. 591–595, Sep. 1998.

[74] S. Chien, "Effects of disturbed flow on endothelial cells," *Ann. Biomed. Eng.*, vol. 36, no. 4, pp. 554–562, 2008.

[75] C. K. Zarins, M. A. Zatina, D. P. Giddens, D. N. Ku, and S. Glagov, "Shear stress regulation of artery lumen diameter in experimental atherogenesis.," *J. Vasc. Surg.*, vol. 5, no. 3, pp. 413–420, Mar. 1987.

[76] H. Meng *et al.*, "A model system for mapping vascular responses to complex hemodynamics at arterial bifurcations in vivo.," *Neurosurgery*, vol. 59, no. 5, pp. 1091–1094, Nov. 2006.

[77] J. K. Hui Meng 1, Zhijie Wang, Yiemeng Hoi, Ling Gao, Eleni Metaxa, Daniel D Swartz, "Complex Hemodynamics at the Apex of an Arterial Bifurcation Induces Vascular Remodeling Resembling Cerebral Aneurysm Initiation," vol. 38, no. 6, pp. 1924–1931, 2009.

[78] L. Zhou, Y. Yan, H. Du, X. Ni, G. Wang, and Q. Wang, "Plaque features and vascular geometry in basilar artery atherosclerosis," *Medicine (Baltimore).*, vol. 99, no. 18, p. e19742, 2020.

[79] A. J. Geers, H. G. Morales, I. Larrabide, C. Butakoff, P. Bijlenga, and A. F. Frangi, "Wall shear stress at the initiation site of cerebral aneurysms," *Biomech. Model. Mechanobiol.*, vol. 16, no. 1, pp. 97–115, 2017.

[80] T. Watanabe *et al.*, "Hemodynamic vascular biomarkers for initiation of paraclinoid internal carotid artery aneurysms using patient-specific computational fluid dynamic simulation based on magnetic resonance imaging," *Neuroradiology*, vol. 60, no. 5, pp. 545–555, 2018.

[81] A. Lauric *et al.*, "Proximal Parent Vessel Tapering is Associated With Aneurysm at the Middle Cerebral Artery Bifurcation.," *Neurosurgery*, vol. 84, no. 5, pp. 1082–1089, May 2019.

[82] A. Lauric, J. Hippelheuser, M. G. Safain, and A. M. Malek, "Curvature effect on hemodynamic conditions at the inner bend of the carotid siphon and its relation to aneurysm formation," *J. Biomech.*, vol. 47, no. 12, pp. 3018–3027, 2014.

[83] A. Mantha, C. Karmonik, G. Benndorf, C. Strother, and R. Metcalfe, "Hemodynamics in a cerebral artery before and after the formation of an aneurysm.," *AJNR. Am. J. Neuroradiol.*, vol. 27, no. 5, pp. 1113–1118, May 2006.

[84] Y. Shimogonya, T. Ishikawa, Y. Imai, N. Matsuki, and T. Yamaguchi, "Can temporal fluctuation in spatial wall shear stress gradient initiate a cerebral aneurysm? A proposed novel hemodynamic index, the gradient oscillatory number (GON)," *J. Biomech.*, vol. 42, no. 4, pp. 550–554, 2009.

[85] H. Chen *et al.*, "Investigating the influence of haemodynamic stimuli on intracranial aneurysm inception," *Ann. Biomed. Eng.*, vol. 41, no. 7, pp. 1492–1504, 2013.

[86] H. Isoda *et al.*, "MR-based computational fluid dynamics with patient-specific boundary conditions for the initiation of a sidewall aneurysm of a basilar artery," *Magn. Reson. Med. Sci.*, vol. 14, no. 2, pp. 139–144, 2015.

[87] K. Tanaka *et al.*, "Relationship between hemodynamic parameters and cerebral aneurysm initiation.," *Annu. Int. Conf. IEEE Eng. Med. Biol. Soc. IEEE Eng. Med. Biol. Soc. Annu. Int. Conf.*, vol. 2018, pp. 1347–1350, Jul. 2018.

[88]   G. J. J. Riccardello *et al.*, "Influence of Relative Residence Time on Side-Wall Aneurysm Inception.," *Neurosurgery*, vol. 83, no. 3, pp. 574–581, Sep. 2018.

[89]   L.-D. Jou *et al.*, "Correlation between lumenal geometry changes and hemodynamics in fusiform intracranial aneurysms.," *AJNR. Am. J. Neuroradiol.*, vol. 26, no. 9, pp. 2357–2363, Oct. 2005.

[90]   L. Boussel *et al.*, "Aneurysm growth occurs at region of low wall shear stress: Patient-specific correlation of hemodynamics and growth in a longitudinal study," vol. 39, no. 11, pp. 2997–3002, 2009.

[91]   D. M. Sforza, K. Kono, S. Tateshima, F. Viñuela, C. Putman, and J. R. Cebral, "Hemodynamics in growing and stable cerebral aneurysms," *J. Neurointerv. Surg.*, vol. 8, no. 4, pp. 407–412, 2016.

[92]   X. J. Zhang, B. L. Gao, T. X. Li, W. L. Hao, S. S. Wu, and D. H. Zhang, "Association of basilar bifurcation aneurysms with age, sex, and bifurcation geometry," *Stroke*, vol. 49, no. 6, pp. 1371–1376, 2018.

[93]   S. Rashad *et al.*, "Impact of bifurcation angle and inflow coefficient on the rupture risk of bifurcation type basilar artery tip aneurysms," *J. Neurosurg.*, vol. 128, no. 3, pp. 723–730, 2018.

[94]   M. C. Villa-Uriol *et al.*, "@neurIST complex information processing toolchain for the integrated management of cerebral aneurysms," *Interface Focus*, vol. 1, no. 3, pp. 308–319, 2011.

[95]   R. P. Kavak, M. Özdemir, N. Kavak, and F. Yıldırım, "Basilar trunk artery aneurysm presenting with brainstem stroke," *Radiol. Case Reports*, vol. 15, no. 4, pp. 387–390, 2020.

[96]   A. Valtorta, E. Scrivano, I. Lylyk, R. Viso, and P. Lylyk, "Superior Cerebellar Artery Aneurysm: Ruptured Blister Aneurysm Treated with Balloon-Assisted Coil Occlusion with Good Angiographic and Clinical Outcome BT - The Aneurysm Casebook: A Guide to Treatment Selection and Technique," H. Henkes, P. Lylyk, and O. Ganslandt, Eds. Cham: Springer International Publishing, 2020, pp. 1533–1542.

[97]   D. P. Patra *et al.*, "Superior Cerebellar Artery Aneurysms, the 'Sui Generis' in Posterior Circulation: The Role of Microsurgery in the Endovascular Era," *World Neurosurg.*, vol. 94, pp. 229–238, 2016.

[98]   K. Irie *et al.*, "Computational fluid dynamic analysis following recurrence of cerebral aneurysm after coil embolization," *Asian J. Neurosurg.*, vol. 7, no. 03, pp. 109–115, 2012.

[99]   A. Fedorov *et al.*, "3D Slicer as an image computing platform for the Quantitative Imaging Network.," *Magn. Reson. Imaging*, vol. 30, no. 9, pp. 1323–1341, Nov. 2012.

[100]   R. Hess, *Blender Foundations: The Essential Guide to Learning Blender 2.6. Focal Press.* 2010.

[101]   R. Izzo, D. Steinman, S. Manini, and L. Antiga, "The Vascular Modeling Toolkit: A Python Library for the Analysis of Tubular Structures in Medical Images," *J. Open Source Softw.*, vol. 3, no. 25, p. 745, 2018.

[102]   J. B. Thomas *et al.*, "Variation in the carotid bifurcation geometry of young versus older adults: Implications for geometric risk of atherosclerosis," *Stroke*, vol. 36, no. 11, pp. 2450–2456, 2005.

[103]   K. Ćmiel-Smorzyk, E. Kawlewska, W. Wolański, A. Hebda, P. Ładziński, and W. Kaspera, "Morphometry of cerebral arterial bifurcations harbouring aneurysms: a case-control study," *BMC Neurol.*, vol. 22, no. 1, pp. 1–13, 2022.

[104]   X. J. Zhang, B. L. Gao, W. L. Hao, S. S. Wu, and D. H. Zhang, "Presence of anterior communicating artery aneurysm is associated with age, bifurcation angle, and vessel diameter," *Stroke*, vol. 49, no. 2, pp. 341–347, 2018.

[105]   M. S. Alnæs, J. Isaksen, K. A. Mardal, B. Romner, M. K. Morgan, and T. Ingebrigtsen, "Computation of hemodynamics in the circle of Willis," *Stroke*, vol. 38, no. 9, pp. 2500–2505, 2007.

[106]   D. M. Sforza, C. M. Putman, and J. R. Cebral, "Hemodynamics of Cerebral Aneurysms.," *Annu. Rev.*

Fluid Mech., vol. 41, pp. 91–107, Jan. 2009.

[107] A. L. Ho, A. Mouminah, and R. Du, "Posterior cerebral artery angle and the rupture of basilar tip aneurysms," *PLoS One*, vol. 9, no. 10, 2014.

[108] G. Saliou *et al.*, "Natural History and Management of Basilar Trunk Artery Aneurysms," *Stroke*, vol. 46, no. 4, pp. 948–953, 2015.

[109] J. Boucherit *et al.*, "Bifurcation geometry remodelling of vessels in de novo and growing intracranial aneurysms: a multicenter study," *J. Neurointerv. Surg.*, vol. 15, no. 6, pp. 566–571, 2023.

[110] P. Berg *et al.*, "Multiple Aneurysms AnaTomy CHallenge 2018 (MATCH): Phase I: Segmentation," *Cardiovasc. Eng. Technol.*, vol. 9, no. 4, pp. 565–581, 2018.

[111] J. Schindelin *et al.*, "Fiji: An open-source platform for biological-image analysis," *Nat. Methods*, vol. 9, no. 7, pp. 676–682, 2012.

[112] R. Bourne, "NIH Image to ImageJ: 25 years of Image Analysis," *Fundam. Digit. Imaging Med.*, vol. 9, no. 7, pp. 185–188, 2010.

[113] F. Pan, N. Mori, S. Mugikura, M. Ohta, and H. Anzai, "The influence of blood velocity and vessel geometric parameters on wall shear stress," *Med. Eng. Phys.*, vol. 124, no. April 2023, p. 104112, 2024.

[114] M. Schöning and B. Hartig, "The development of hemodynamics in the extracranial carotid and vertebral arteries," *Ultrasound Med. Biol.*, vol. 24, no. 5, pp. 655–662, 1998.

[115] M. Schöning and P. Scheel, "Color duplex measurement of cerebral blood flow volume: Intra- and interobserver reproducibility and habituation to serial measurements in normal subjects," *J. Cereb. Blood Flow Metab.*, vol. 16, no. 3, pp. 523–531, 1996.

[116] H. Simon, K. Niederkorn, S. Horner, M. Duft, and M. Schröckenfuchs, "[Effect of head rotation on the vertebrobasilar system. A transcranial Doppler ultrasound contribution to the physiology]," *HNO*, vol. 42, no. 10, p. 614—618, Oct. 1994.

[117] P. Scheel, C. Ruge, and M. Schöning, "Flow velocity and flow volume measurements in the extracranial carotid and vertebral arteries in healthy adults: Reference data and the effects of age," *Ultrasound Med. Biol.*, vol. 26, no. 8, pp. 1261–1266, 2000.

[118] B. J. Kim *et al.*, "Asymptomatic Basilar Artery Plaque Distribution and Vascular Geometry.," *J. Atheroscler. Thromb.*, vol. 26, no. 11, pp. 1007–1014, Nov. 2019.

[119] J. Ravensbergen, J. W. Ravensbergen, J. K. B. Krijger, B. Hillen, and H. W. Hoogstraten, "Localizing Role of Hemodynamics in Atherosclerosis in Several Human Vertebrobasilar Junction Geometries," *Arter. Thromb Vasc Biol*, vol. 18, pp. 708–717, 1998.

[120] A. M. Malek and S. L. Alper, "Hemodynamic Shear stress and Its Role in Atherosclerosis," vol. 282, no. 21, pp. 2035–2042, 2007.

[121] H. Tanaka *et al.*, "Relationship between variations in the circle of Willis and flow rates in internal carotid and basilar arteries determined by means of magnetic resonance imaging with semiautomated lumen segmentation: Reference data from 125 healthy volunteers," *Am. J. Neuroradiol.*, vol. 27, no. 8, pp. 1770–1775, 2006.

[122] V. Zbornikova and C. Lassvik, "Duplex scanning in presumably normal persons of different ages," *Ultrasound Med. Biol.*, vol. 12, no. 5, pp. 371–378, 1986.

[123] R. Manara *et al.*, "Basilar artery changes in fabry disease," *Am. J. Neuroradiol.*, vol. 38, no. 3, pp. 531–

536, 2017.

[124] H. Xu, D. Baroli, and A. Veneziani, "Global sensitivity analysis for patient-specific aortic simulations: The role of geometry, boundary condition and large eddy simulation modeling parameters," *J. Biomech. Eng.*, vol. 143, no. 2, pp. 1–12, 2021.

[125] G. D. Maher, C. M. Fleeter, D. E. Schiavazzi, and A. L. Marsden, "Geometric uncertainty in patient-specific cardiovascular modeling with convolutional dropout networks," *Comput. Methods Appl. Mech. Eng.*, vol. 386, p. 114038, 2021.

[126] I. G. H. Jansen *et al.*, "Generalized versus patient-specific inflow boundary conditions in computational fluid dynamics simulations of cerebral aneurysmal hemodynamics," *Am. J. Neuroradiol.*, vol. 35, no. 8, pp. 1543–1548, 2014.

[127] A. G. Radaelli *et al.*, "Reproducibility of haemodynamical simulations in a subject-specific stented aneurysm model - A report on the Virtual Intracranial Stenting Challenge 2007," *J. Biomech.*, vol. 41, no. 10, pp. 2069–2081, 2008.

[128] J. F. LaDisa, L. E. Olson, H. A. Douglas, D. C. Warltier, J. R. Kersten, and P. S. Pagel, "Alterations in regional vascular geometry produced by theoretical stent implantation influence distributions of wall shear stress: Analysis of a curved coronary artery using 3D computational fluid dynamics modeling," *Biomed. Eng. Online*, vol. 5, 2006.

[129] R. Perinajová *et al.*, "Assessment of turbulent blood flow and wall shear stress in aortic coarctation using image-based simulations," *Biomed. Eng. Online*, vol. 20, no. 1, pp. 0–20, 2021.

[130] C. Karmonik *et al.*, "Quantitative comparison of hemodynamic parameters from steady and transient CFD simulations in cerebral aneurysms with focus on the aneurysm ostium," *J. Neurointerv. Surg.*, vol. 7, no. 5, pp. 367–372, 2015.

[131] A. J. Geers, I. Larrabide, H. G. Morales, and A. F. Frangi, "Comparison of steady-state and transient blood flow simulations of intracranial aneurysms," *2010 Annu. Int. Conf. IEEE Eng. Med. Biol. Soc. EMBC'10*, pp. 2622–2625, 2010.

[132] J. P. Ku, C. J. Elkins, and C. A. Taylor, "Comparison of CFD and MRI flow and velocities in an in vitro large artery bypass graft model," *Ann. Biomed. Eng.*, vol. 33, no. 3, pp. 257–269, 2005.

[133] M. Motomiya, "Flow patterns in the human carotid artery bifurcation," *Stroke*, vol. 15, no. 1, pp. 50–56, 1984.

[134] M. R. Roach, "Biophysical analyses of blood vessel walls and blood flow.," *Annu. Rev. Physiol.*, vol. 39, pp. 51–71, 1977.

[135] M. A. H. Mohd Adib, S. Ii, Y. Watanabe, and S. Wada, "Minimizing the blood velocity differences between phase-contrast magnetic resonance imaging and computational fluid dynamics simulation in cerebral arteries and aneurysms," *Med. Biol. Eng. Comput.*, vol. 55, no. 9, pp. 1605–1619, 2017.

[136] A. Sarrami-Foroushani, M. N. Esfahany, H. S. Rad, K. Firouznia, M. Shakiba, and H. Ghanaati, "Effects of variations of flow and heart rate on intra-aneurysmal hemodynamics in a ruptured internal carotid artery aneurysm during exercise," *Iran. J. Radiol.*, vol. 13, no. 1, pp. 1–6, 2016.

[137] A. Valencia, H. Morales, R. Rivera, E. Bravo, and M. Galvez, "Blood flow dynamics in patient-specific cerebral aneurysm models: The relationship between wall shear stress and aneurysm area index," *Med. Eng. Phys.*, 2008.

[138]   K. M. Saqr *et al.*, "What does computational fluid dynamics tell us about intracranial aneurysms? A meta-analysis and critical review," *J. Cereb. Blood Flow Metab.*, vol. 40, no. 5, pp. 1021–1039, 2020.

[139]   Y. Hua, J. H. Oh, and Y. B. Kim, "Influence of parent artery segmentation and boundary conditions on hemodynamic characteristics of intracranial aneurysms," *Yonsei Med. J.*, vol. 56, no. 5, pp. 1328–1337, 2015.

[140]   A. Marzo *et al.*, "Computational hemodynamics in cerebral aneurysms: The effects of modeled versus measured boundary conditions," *Ann. Biomed. Eng.*, vol. 39, no. 2, pp. 884–896, Feb. 2011.

[141]   R. Retarekar *et al.*, "Stratification of a population of intracranial aneurysms using blood flow metrics," *Comput. Methods Biomech. Biomed. Engin.*, vol. 18, no. 10, pp. 1072–1082, 2015.

[142]   H. G. Morales and O. Bonnefous, "Unraveling the relationship between arterial flow and intra-aneurysmal hemodynamics," *J. Biomech.*, vol. 48, no. 4, pp. 585–591, 2015.

[143]   J. Xiang, A. H. Siddiqui, and H. Meng, "The effect of inlet waveforms on computational hemodynamics of patient-specific intracranial aneurysms," *J. Biomech.*, vol. 47, no. 16, pp. 3882–3890, Dec. 2014.

[144]   C. Karmonik, C. Yen, O. Diaz, R. Klucznik, R. G. Grossman, and G. Benndorf, "Temporal variations of wall shear stress parameters in intracranial aneurysms-importance of patient-specific inflow waveforms for CFD calculations," *Acta Neurochir. (Wien).*, vol. 152, no. 8, pp. 1391–1398, Aug. 2010.

[145]   P. M. McGah *et al.*, "Accuracy of computational cerebral aneurysm hemodynamics using patient-specific endovascular measurements," *Ann. Biomed. Eng.*, vol. 42, no. 3, pp. 503–514, Mar. 2014.

[146]   J. R. Cebral, M. A. Castro, C. M. Putman, and N. Alperin, "Flow-area relationship in internal carotid and vertebral arteries," *Physiol. Meas.*, 2008.

[147]   C. D. Murray, "The Physiological Principle of Minimum Work: I. The Vascular System and the Cost of Blood Volume," *Proc. Natl. Acad. Sci.*, vol. 12, no. 3, pp. 207–214, 1926.

[148]   K. Valen-Sendstad *et al.*, "Real-World Variability in the Prediction of Intracranial Aneurysm Wall Shear Stress: The 2015 International Aneurysm CFD Challenge," *Cardiovasc. Eng. Technol.*, vol. 9, no. 4, pp. 544–564, 2018.

[149]   M. Najafi *et al.*, "How patient-specific do internal carotid artery inflow rates need to be for computational fluid dynamics of cerebral aneurysms?," *J. Neurointerv. Surg.*, vol. 13, no. 5, pp. 459–464, 2021.

[150]   X. Liu *et al.*, "Identification of intra-individual variation in intracranial arterial flow by MRI and the effect on computed hemodynamic descriptors," *Magn. Reson. Mater. Physics, Biol. Med.*, vol. 34, no. 5, pp. 659–666, Oct. 2021.

[151]   J. R. Cebral, M. A. Castro, S. Appanaboyina, C. M. Putman, D. Millan, and A. F. Frangi, "Efficient Pipeline for Image-Based Patient-Specific Analysis of Cerebral Aneurysm Hemodynamics : Technique and Sensitivity," vol. 24, no. 4, pp. 457–467, 2005.

[152]   P. Hendrix *et al.*, "Arterial supply of the lower cranial nerves: A comprehensive review," *Clin. Anat.*, vol. 27, no. 1, pp. 108–117, 2014.

Acknowledgement

I came to Japan from October 4th, 2017, without much considering and deep thinking of difficulties I might face for studying in a foreign country without the capability of speaking the local language. It turned out that I did encounter a lot of tough times, but they were never desperate. I'm fortunate enough to have very nice teachers, colleagues and friends who kindly offered their help whenever I needed them. This whole studying process is more than getting my degree. I got the opportunity to meet, to communicate and collaborate with people from worldwide. I saw a wider world, and this is, for sure, going to change my view on my life.

Too many thanks to say. Thank Professor Ohta and Professor Anzai for having long discussions with me. I can very stubborn some time and thank them for understanding me and keeping me as myself. Thank Professor Mugikura, Professor Mori, and Professor Philippe for offering me the chance to work together.

Thank students in our lab for understanding my Japanese, helping my study and my life in Japan. Dr. Zi Wang kindly offered me a lot of help. Dr. Kaihong Yu, Dr.Yujie Li and Dr. Mingzi Zhang gave me suggestions on both research and life. Dr. Simon Tupin kindly gave me great suggestions on my research. The senior students, Dr. Narendra Putra, Dr. Yuta Muramoto, Mr. Kazuhiro Watanabe, Mr. Makoto Ito, Dr. Haoran Wang were generous enough to have discussions with me. Thanks to Mr. Ko kitamura, Mr. Ryota Nagano, Mr. Kohei Misuzuka, Mr. Yugo Shindo, Mr. Naohiro Kobayashi, Mr. Kazuki Takeda, Mr. Muhammad Shiddiq Hashuro, Dr. Meghane Decroocq, Mr. Keiichiro Shiraishi, Mr. Kotaro Daibo and Ms. Yukiko Kojima, who have already graduated, for their help and kindness. Thanks to Professor Ryuhei Yamaguchi, Mr. Kazuyoshi Jin, Mr. Hanif Saifurrahman, Mr. Daisuke Goanno, Mr. Masahiro Hasegawa, Ms. Riko Hasegawa, Mr. Kazuki Shibata, Mr. Tatsuya Uchida, Mr. Keito Yanagisawa, Mr. Naoki Kobayashi Mr. Shintaro Sasaki, and Mr. Louis Paquet, who are still members in our lab or are also going to graduate this spring. Great thanks to Dr. Satomi Hirose and Mr. Yutaro Kohata for their kind support. Best wishes to all of you!

This may not be very common, but I also would like to express my gratitude to people from Carpediem Sendai. They helped me for my hardest time when I was preparing for this thesis and defense.

Too many thank you to say for a two-page acknowledgement. Some names may not written inside but I do wish all the bests to everyone. Time may fly but my gratitude and wishes will always be here together with this thesis.

Fangjia PAN

March 25th, 2024

Accomplishment

List of publications (peer-reviewed)

1. <u>Pan, F.</u>, Anzai, H., Mugikura, S., Kitamura, K., & Ohta, M. (2019, November). The relationship between the arterial geometry and wall shear stress in the vertebrobasilar system. In ASME International Mechanical Engineering Congress and Exposition (Vol. 59407, p. V003T04A039). American Society of Mechanical Engineers. (chapter 4)

2. Fukuda, S., Shimogonya, Y., Nakamura, M., Yamada, T., Suzuki, K., Yamamoto, Y., Kanou, K., Okada, N., <u>Pan, F.</u>, Okudaira, T., Kuwahara, S., & CFD-BIO study group. (2019). Review on the formation and growth of cerebral aneurysms. Journal of Biorheology, 33(2), 43-52. (chapter 2)

3. <u>Pan, F.</u>, Mori, N., Mugikura, S., Bijlenga, P., Ohta, M., & Anzai, H. (2023, August). Generalized versus Specific Boundary Conditions for CFD in vertebral-basilar artery. In 2023 8th International Conference on Instrumentation, Control, and Automation (ICA) (pp. 19-24). IEEE. (chapter 5)

4. <u>Pan, F.</u>, Bijlenga, P., Mori, N., Mugikura, S., Ohta, M., & Anzai, H. Exploring the Variations in Angles Around Basilar Bifurcation Categorized by Aneurysm Locations. In The 2023 Biomedical Engineering International Conference (BMEiCON-2023). Tokyo, Japan, 2023, pp. 1-5, doi: 10.1109/BMEiCON60347.2023.10322063. (chapter 3)

5. <u>Pan F.</u>, Mori N., Mugikura S., Ohta M., Anzai H. The influence of blood velocity and vessel geometric parameters on wall shear stress. Med Eng Phys. 2024 Feb;124:104112. doi: 10.1016/j.medengphy.2024.104112. Epub 2024 Jan 28. PMID: 38418022 (chapter 4)

International conference/ symposium

Peer reviewed

1. Pan, F., Anzai, H., Mugikura, S., Kitamura, K., Ohta, M., The relationship between the arterial geometry and wall shear stress in the vertebrobasilar system International Mechanical Engineering Congress & Exposition (IMECE) 2019, 2019/11/10-14, Salt lake city, America (same as publishment no.1)

2. Pan, F., Mori, N., Mugikura, S., Anzai, H., and Ohta, M., Vertebral dominance and basilar artery 7th International Conference on Computational & Mathematical

Biomedical Engineering, 2022/6/27-29, Politecnico di Milano, Campus Leonardo, Milan, Italy

3. Pan, F., Bijlenga, P., Mori, N., Mugikura, S., Ohta, M., Anzai, H. Exploring the Variations in Angles Around Basilar Bifurcation Categorized by Aneurysm Locations. In The 2023 Biomedical Engineering International Conference (BMEiCON-2023) (same as publishment no.4)

Non-peer reviewed

1. Pan, F., Ohta, M., Anzai, H., Mugikura, S., Mori, N., The influence brought by specific boundary conditions on vascular simulations 2ND INTERNATIONAL SYMPOSIUM ON COMPUTATIONAL BIOFLUID 2020, online(webex), 2020/12/16

2. Pan, F., Mori, N., Mugikura, S., Anzai, H., Ohta, M., Influence of flow rate estimation at vertebral arteries on basilar artery wall shear stress The 11th Asian-pacific conference on Biomechanics, 2021/12/02-04, online

3. Pan, F., Mori, N., Mugikura, S., Anzai, H., Ohta, M., Influences brought by different wall shear stress analysis on curved vessels UTM-IFS 3rd International Biofluid Symposium 2021, 2021/11/18, online

Domestic seminar/ workshop

1. Pan, F., Porosity dependency of an optimized stent design for an intracranial aneurysm # Journal introduction Computational Fluid Dynamics with Clinicians and Bioengineers Meeting, 2018/06/29 - 7/1 Taiwan, China

2. Pan, F., Mori, N., Mugikura, Bijlenga, P., Ohta, M., Anzai, H., Boundary Conditions in Computational Fluid Dynamics Simulations of Vertebral-Basilar Artery: How to use generalized boundary conditions? 第 1 回 生体流れ計測・解析に関する合同セミナー

3. Pan, F., Bijlenga, P., Mori, N., Mugikura, S., Ohta, M., Anzai, H. The correlation between vascular angles and aneurysm formation, 日本機械学会東北支部第 59 期総会・講演会, 2024/03/15 Sendai, Japan

Grants/ Scholarship

1. Graduate Program for Integration of Mechanical Systems: GP-Mech
2. JST Spring